

RESEARCH ARTICLE

10.1029/2017JD027974

This article is a companion to Vadas et al. (2018) <https://doi.org/10.1029/2017JD027970>.

Key Points:

- Main point #1: Mountain waves break in the winter stratosphere over McMurdo, exciting secondary GWs with much larger horizontal wavelengths
- Main point #2: Secondary GWs create fishbone structures in the stratosphere and have similar periods, wavelengths, and azimuths above and below the knee
- Main point #3: Most of the wintertime GWs at $z > 70$ km above McMurdo are secondary GWs

Supporting Information:

- Supporting Information S1
- Movie S1
- Movie S2

Correspondence to:

S. L. Vadas,
vasha@cora.nwra.com

Citation:

Vadas, S. L., & Becker, E. (2018). Numerical modeling of the excitation, propagation, and dissipation of primary and secondary gravity waves during wintertime at McMurdo Station in the Antarctic. *Journal of Geophysical Research: Atmospheres*, 123, 9326–9369. <https://doi.org/10.1029/2017JD027974>

Received 31 OCT 2017

Accepted 15 MAY 2018

Accepted article online 23 MAY 2018

Published online 12 SEP 2018

Numerical Modeling of the Excitation, Propagation, and Dissipation of Primary and Secondary Gravity Waves during Wintertime at McMurdo Station in the Antarctic

Sharon L. Vadas¹  and Erich Becker² 

¹Northwest Research Associates, Boulder, Colorado, USA, ²Leibniz Institute of Atmospheric Physics, Kühlungsborn, Germany

Abstract We analyze the results of the gravity wave (GW)-resolving, high-resolution Kühlungsborn Mechanistic general Circulation Model in July at McMurdo Station (166.69°E and 77.84°S), where strong downslope eastward winds create strong mountain wave (MW) events. These MWs have horizontal wavelengths of $\lambda_H \approx 230$ km, propagate to $z \sim 40$ –60 km, and can have upward phases in time if the eastward wind accelerates in time. Additionally, inertia-GWs (IGWs) with $\lambda_H \sim 500$ –800 km and ground-based periods of $\tau_r \sim 5$ –6 hr are generated in the troposphere from unbalanced, large-scale flow. The density-scaled GW amplitudes are ~ 10 times smaller at $z \sim 80$ –100 km than at $z < 50$ km because of severe wave dissipation. “Fishbone” structures are seen at $z \sim 30$ –60 km with upward (downward) phases in time below (above) the “knee” at z_{knee} . We horizontally filter the perturbations to isolate the GWs in a fishbone structure for a particular MW event. We find that these GWs have strikingly similar parameters below and above $z_{\text{knee}} = 46$ km, with ground-based horizontal phase speeds of $c_H \sim 40$ –60 m/s, $\tau_r \sim 9$ –10 hr, $\lambda_H \sim 1,600$ –2,050 km, vertical wavelengths of $\lambda_z \sim 18$ –25 km, and azimuths of $\Upsilon = 145^\circ$ – 151° east of north. We show that these are secondary GWs excited by a body force at z_{knee} created by MW dissipation approximately 400 km northwest of McMurdo 2.5 hr earlier and that the secondary GW scales and propagation directions are consistent with this force. Importantly, we show that most of the GWs at $z > 70$ km are secondary GWs not primary GWs from the troposphere.

1. Introduction

Wind flow over orography excites GWs called mountain waves (MWs; Holton, 1992; Fritts & Alexander, 2003). If the wind is constant in time and the flow is linear, the ground-based phase speed of a MW, c_H , is 0 and the GW solution is steady state. MWs have been observed over the southern Andes in South America and the Antarctic Peninsula with the Cryogenic Infrared Spectrometers and Telescopes for the Atmosphere (Eckermann & Preusse, 1999; Ern et al., 2004), the Upper Atmosphere Research Satellite Microwave Limb Sounder (Jiang et al., 2002; Wu & Jiang, 2002), the Atmospheric Infrared Sounder (AIRS; Alexander & Teitelbaum, 2007, 2011; Gong et al., 2012; Hoffmann & Alexander, 2009; Wu et al., 2006), the High Resolution Dynamics Limb Sounder and the Sounding of the Atmosphere using Broadband Emission Radiometry (Alexander et al., 2008; Ern et al., 2011), the meteorological program of the Global Positioning System (Tsuda et al., 2000), Global Positioning System radio occultation (de la Torre & Alexander, 2005), and superpressure balloons (Plougonven et al., 2008; Vincent et al., 2007; Walterscheid et al., 2016). They have also been observed over New Zealand in the Deep Propagating Gravity Wave Experiment (DEEPWAVE; Bossert et al., 2015, 2017; Fritts et al., 2016; Heale et al., 2017) and near McMurdo Station in the Antarctic with superpressure balloons and AIRS (Hendricks et al., 2014; Hoffmann et al., 2013; Vincent et al., 2007).

Yamashita et al. (2009) found that the GW potential energy density at $z = 30$ –45 km was 6 times larger at Rothera Station than at South Pole Station during the winter, while the energy densities were small and comparable at the two stations during the summer. They attributed the wintertime difference to the excitation of (westward) MWs at Rothera, which propagated to $z \sim 30$ –45 km through the background eastward wind. Kaifler et al. (2015) found that the GW potential energy density at $z = 30$ –40 km was 3–5 times larger during the winter than during the summer at Davis (69°S, 78°E), Antarctica. Chen et al. (2013) observed two

simultaneous IGWs at $z = 80\text{--}100$ km at McMurdo in June. One had $\tau_r \sim 7.7$ hr, $\lambda_z \sim 22$ km, $\lambda_H \sim 2,200$ km, $c_H = \lambda_H/\tau_r \sim 80$ m/s, and azimuth $\Upsilon \sim 11^\circ$ east of north and was traced back to a region of unbalanced flow in the stratosphere. Murphy et al. (2014) analyzed the IGWs at Davis Station using radiosonde data and found that $\sim 50\%$ were downward propagating for $z = 13\text{--}30$ km during May–October. They suggested that the downward propagating IGWs (upward phase propagation) might have been generated by an unbalanced flow in the lower stratosphere, which creates upward- and downward-propagating IGWs (e.g., Vadas & Fritts, 2001; Zhu & Holton, 1987). Chen et al. (2016) found that IGWs with $\tau_r \sim 3\text{--}10$ hr and $\lambda_z \sim 20\text{--}30$ km were persistent at McMurdo from the stratosphere to lower thermosphere. Due to the change in the slope of the GW spectra with altitude, they postulated a stratosphere source for the IGWs observed in the mesosphere and lower thermosphere (MLT). Using a 2-D Morlet wavelet transform technique, Chen and Chu (2017) estimated that the IGWs in the MLT had $\lambda_H \sim 400\text{--}4,000$ km and $c_H = 30\text{--}140$ m/s at McMurdo. Zhao et al. (2017) found that the GWs at $z = 30\text{--}50$ km had upward and downward phases in time during the winter at McMurdo, with $\lambda_z \sim 3\text{--}13$ km and $\tau_r \sim 2\text{--}10$ hr. They estimated $\lambda_H \sim 350\text{--}500$ km during June–October, which is significantly smaller than the estimated λ_H in the MLT (Chen et al., 2013; Chen & Chu, 2017). This strongly suggests that during the wintertime at McMurdo, the GWs in the MLT might be different from the GWs in the stratosphere. Indeed, observations have pointed toward stratospheric GW sources related to imbalances of the polar night jet (Alexander et al., 2011; Chen et al., 2013; Sato & Yoshiki, 2008; Shibuya et al., 2017; Yoshiki & Sato, 2000; Yoshiki et al., 2004).

When a GW breaks (e.g., when it approaches a critical level), the flow is nonlinear and there is a cascade to smaller scales and eventually to turbulence. Small-scale “secondary” GWs are excited having smaller λ_H than that of the breaking GW (e.g., Bacmeister & Schoeberl, 1989; Bossert et al., 2017; Chun & Kim, 2008; Franke & Robinson, 1999; Satomura & Sato, 1999; Zhou et al., 2002). Because these GWs typically cannot propagate very far before being reabsorbed by the fluid (although they may carry and transport significant momentum flux in the process (Bossert et al., 2017)), they can be loosely thought of as being part of the transition to smaller scales and to turbulence.

Along with wave breaking and the transition to turbulence, momentum and energy is deposited into the background flow on a larger horizontal scale than λ_H of the breaking GW; indeed, this horizontal scale is set by the horizontal scale of the wave packet (Vadas & Fritts, 2002). This momentum deposition corresponds to a “local body force,” and results in a temporally and spatially localized horizontal acceleration of the background flow. The zonal and meridional components of the body force are given by the convergence of the pseudo momentum flux (derived in Appendix A):

$$F_{x,\text{tot}} = -\frac{1}{\bar{\rho}} \partial_z \left(\bar{\rho} \left(\overline{u'w'} - \frac{f C_p}{g} \overline{T'v'} \right) \right), \quad F_{y,\text{tot}} = -\frac{1}{\bar{\rho}} \partial_z \left(\bar{\rho} \left(\overline{v'w'} + \frac{f C_p}{g} \overline{T'u'} \right) \right). \quad (1)$$

Here u , v , and w are the zonal, meridional, and vertical velocities, respectively; ρ is density; and T is temperature. The primes denote deviations from the background flow due to GWs, and the overlines denote averages over several GW wavelengths. Additionally, g is the gravitational acceleration, C_p is the specific heat capacity at constant pressure, and f is the Coriolis parameter in the f -plane approximation, that is, $f = 2\Omega \sin \theta$ with $\Omega = 2\pi/24$ hr and θ being a fixed latitude. The temperature flux terms in equation (1) correspond to the Stokes drift correction for atmospheric waves that are affected by the Coriolis force (Dunkerton, 1978). Note that equation (1) is equivalent to the corresponding expression given in equation (41) in Fritts and Alexander (2003) when using the polarization relations for a monochromatic GW.

$F_{x,\text{tot}}$ and $F_{y,\text{tot}}$ in equation (1) do not include small-scale nonlinearities that accompany the cascade to turbulence. However, since the latter spread horizontally, the extent of the body force is estimated to be approximately twice that of the breaking wave packet (Vadas & Fritts, 2002). For example, if a primary GW packet consists of two wave cycles that are breaking, the horizontal extent of the body force is estimated to be $\sim 4\lambda_H$, which is much larger than λ_H of the breaking GW (Vadas & Fritts, 2002). Because momentum deposition occurs on timescales of $\sim (1 - 2)\tau_r$, where τ_r is the primary GW period, the body force accelerates the background flow horizontally over the same timescales. This causes the flow to be unbalanced. The fluid responds by (a) creating a 3-D horizontal mean flow that consists of two counter-rotating cells and (b) exciting larger-scale secondary GWs (Fritts et al., 2006; Plougonven et al., 2008; Vadas & Fritts, 2001, 2002, 2013; Vadas et al., 2003; Vadas & Liu, 2009, 2013). These secondary GWs propagate forward, backward, upward, and downward away from the body force and have a broad spectrum of horizontal scales that peak at approximately twice the width of the body force (Vadas et al., 2003, 2018). For the above example, the secondary GW

spectrum peaks at $\sim 8\lambda_H$. Even if the portion of the primary GW that breaks only consists of one-half of a wave cycle, the secondary GW spectrum peaks at $\sim 2\lambda_H$, which is still larger than λ_H of the breaking GW.

The secondary GWs excited by a body force have λ_H much larger than that of the small-scale secondary GWs mentioned above. This important feature typically allows them to propagate to much higher altitudes before dissipating, because they have much larger horizontal phase speeds, $c_H = \lambda_H/\tau_r$, than both the primary GWs and the small-scale secondary GWs. Because of this, it is likely that these latter (larger-scale) secondary GWs are much more important for the transport of momentum and energy than the former small-scale secondary GWs. It is unfortunate that the phrase “secondary GWs” has been applied to both of these different types of GWs in the literature. The astute reader must therefore be careful to distinguish between these two types of secondary GWs. Indeed, only if the secondary GWs have λ_H greater than that of the primary GWs can their sources be identified as body forces from the primary breaking GWs. For the rest of this paper, we only use the term “secondary GWs” to describe the (latter, larger-scale) GWs generated by a body force.

Over the past decade, high-resolution, GW-resolving general circulation models (GCMs) have modeled GWs generated by orography, jet stream adjustment, and convection (Becker, 2009; Becker & Vadas, 2018; Hoffmann et al., 2010; Liu et al., 2014; Sato et al., 2009, 2012; Watanabe et al., 2006, 2008). Because of resolution constraints, these models can only simulate the medium-scale MWs created by flow over orography. However, the omission of small-scale MWs may still result in realistic dynamical and thermal structures in the stratosphere and mesosphere (Sato et al., 2012; Watanabe et al., 2008).

Using a high-resolution, GW-resolving GCM, Sato et al. (2012) found stratospheric MW hotspots leeward of the southern Andes during winter. They showed a correlation between downward energy flux in the stratosphere and orographic GW activity over the southern Andes. They postulated that this might be due to partial wave reflection from the changing buoyancy frequency or to nonlinear processes (i.e., small-scale secondary GWs created from wave breaking), although neither possibility was deemed as entirely satisfactory. They also found orographic GWs near McMurdo in July and suggested that these GWs were created by katabatic winds at the western edge of the Ross Sea (Watanabe et al., 2006).

Recently, Becker and Vadas (2018) analyzed the characteristics of GWs in the stratosphere and mesosphere in the southern winter hemisphere using the high-resolution, GW-resolving Kühlungsborn Mechanistic general Circulation Model (KMCM). They found that MWs created by eastward flow over the southern Andes and Antarctic Peninsula broke and created temporally and spatially dependent wave drag in the stratosphere. At higher altitudes in the MLT, they found GWs with predominantly eastward and westward components and $c_H \sim 60$ m/s. They noted that strong MW events in the stratosphere preceded strong GW events in the MLT. They identified the GWs in the MLT as being secondary GWs created from the intermittent body forces due to MW breaking in the stratosphere. Additionally, they found that the eastward secondary GWs dissipated at $z \sim 90$ – 100 km and created a second eastward wind peak there.

Although Becker and Vadas (2018) examined the dynamical effect that secondary GWs have on the MLT for the first time, they did not investigate their properties or sources in detail; in particular, they did not perform a detailed analysis of λ_H , they did not look for downward-propagating GWs with similar λ_H , vertical wavelength λ_z , τ_r , and propagation directions nor did they locate specific body forces as sources of the identified secondary GWs.

In this paper, we investigate the generation, propagation, and dissipation of primary and secondary GWs over Antarctica and at McMurdo in the troposphere, stratosphere, and mesosphere during July when the polar night jet is fairly well established. We briefly describe the KMCM in section 2. In section 3, we describe the wave activity in July. We investigate the primary and secondary GWs during several large events in section 4. Section 5 provides our conclusions. Appendix A contains our derivation of the GW pseudo momentum flux needed to calculate the body forces. Appendix B contains the equations we use to transform from geophysical to 2-D Cartesian coordinates, which allows for the straightforward determination of λ_H and the direction of propagation of GWs at polar latitudes.

2. Description of the KMCM

We use results from the KMCM, which is a high-resolution, GW-resolving, hydrostatic, and free-running global circulation model. It is based on a standard spectral dynamical core with a terrain-following hybrid

vertical coordinate. We use a triangular spectral truncation at total horizontal wave number 240 and 190 full model layers (T240L190) up to $\sim 3 \times 10^{-5}$ hPa ($z \sim 130$ km). The resulting horizontal and vertical grid spacings are ~ 55 km and ~ 600 m, respectively, for $z \leq 100$ km. The smallest horizontal wavelength resolvable is $\lambda_H = 165$ km.

The KMCM includes explicit computations of radiation and the tropospheric moisture cycle (Becker et al., 2015, Becker, 2017). Land-sea contrasts are included via orography and land-sea masks (albedo, relative humidity, heat capacity, and roughness length). A simple slab ocean is included to close the surface energy budget.

Subgrid-scale parameterizations consist of (a) a local boundary diffusion scheme, (b) a simple tropospheric moist convection scheme, and (c) a Smagorinsky-type horizontal and vertical diffusion scheme for the whole atmosphere, with both diffusion coefficients dependent on the Richardson number, R_i , such as to give rise to wave damping when $R_i \leq 0.25$ (Becker, 2009; Becker & Vadas, 2018). Additionally, there is a sponge layer at $z > 100$ km owing to linear harmonic horizontal diffusion. The entire momentum diffusion (including the sponge layer) conserves angular momentum since it is based on a symmetric stress-tensor formulation. The model thermosphere also includes a simple ion drag scheme. All subgrid-scale momentum tendencies are energetically balanced by the corresponding frictional heating terms (see discussion in Becker, 2017). A former version of the KMCM with high resolution and resolved GWs was used, for example, in Becker (2009), Hoffmann et al. (2010), and Becker (2012).

The KMCM simulates (spatially and temporally localized) momentum deposition. This wave-mean flow interaction occurs in response to the dynamical instability of the resolved GWs and subgrid-scale turbulent diffusion, as mentioned above. Note that the subgrid-scale diffusion is essential to induce wave-mean flow interaction. This notion is in accordance with the Wentzel-Kramers-Brillouin solution for GWs damped by turbulent diffusion (Becker, 2012; Lindzen, 1981).

In this study, we employ the same model version that was used in Becker and Vadas (2018). Our resolution of the KMCM data is $\Delta t = 45$ min, $\Delta \phi = 1.875^\circ$ in longitude from 0°E to 360°E , and $\Delta \theta = 0.8^\circ$ in latitude from 89.6°S to 50.4°S . We extrapolate the data to an altitudinal (geometric height) grid having a vertical grid spacing of $\Delta z = 2$ km for $z \geq 4$ km.

3. Wave Activity Over McMurdo During July

Figure 1 shows the temperature, T , zonal velocity, u , and meridional velocity, v , at McMurdo during July. The polar night jet in the stratosphere is strong and eastward: $u \sim 60\text{--}120$ m/s. Daily to weekly variability caused by Rossby waves is visible in all three components at $z \sim 40\text{--}70$ km (Lu et al., 2013, 2017). Figure 2 shows a “blowup” at $z = 70\text{--}100$ km for 3–11 July. This altitudinal range includes that of the Fe Boltzmann lidar measurements at McMurdo (Chen et al., 2013, 2016; Chen & Chu, 2017; Chu et al., 2011). Although the semidiurnal tide is strong and variable in u and v at $z \sim 80\text{--}100$ km, it is weak in T . Instead, GWs with $\tau_r \sim 3\text{--}11$ hr and $T' \sim 10\text{--}40$ K are easily visible in T (unlike in u and v). These amplitudes, as well as the lack of a significant semidiurnal tide in the temperature, agree well with observations (Chen et al., 2013). Note that the GW periods seen over McMurdo during midwinter are shorter than those inferred by Shibuya et al. (2017) in the lower mesosphere above Syowa Station (39.6°E , 69°S) during a particular week in March 2015. Those authors obtained quasi 12-hr periods for large-scale IGWs from radar measurements and a numerical simulation initialized by Modern-Era Retrospective Analysis for Research and Applications data.

We remove the semidiurnal and diurnal tides and planetary waves by applying a Fourier filter and eliminating all waves with $\tau_r > 11$ hr. (Note that this also removes stationary and quasi-stationary MWs with $\tau_r > 11$ hr.) Figure 3 shows the resulting density-scaled (or “scaled”) GW perturbations, which are T' , u' , and v' multiplied by the scaling factor $\sqrt{\bar{\rho}/\bar{\rho}_0}$, where $\bar{\rho}_0$ is an arbitrary constant value. Here we choose the value of $\bar{\rho}_0$ to be the value of $\bar{\rho}$ at 0°E , 90°S and $z = 5$ km on 1 July at OUT: $\bar{\rho}_0 = 880$ gm/m³. Note that we show the scaled perturbations in Figure 3 to see the GW perturbations at all altitudes “equally,” since a GW’s amplitude grows exponentially with height (Hines, 1960). Thus, a conservative, linear, nondissipating upward or downward-propagating GW in an isothermal atmosphere in a uniform wind would have a constant scaled amplitude with height.

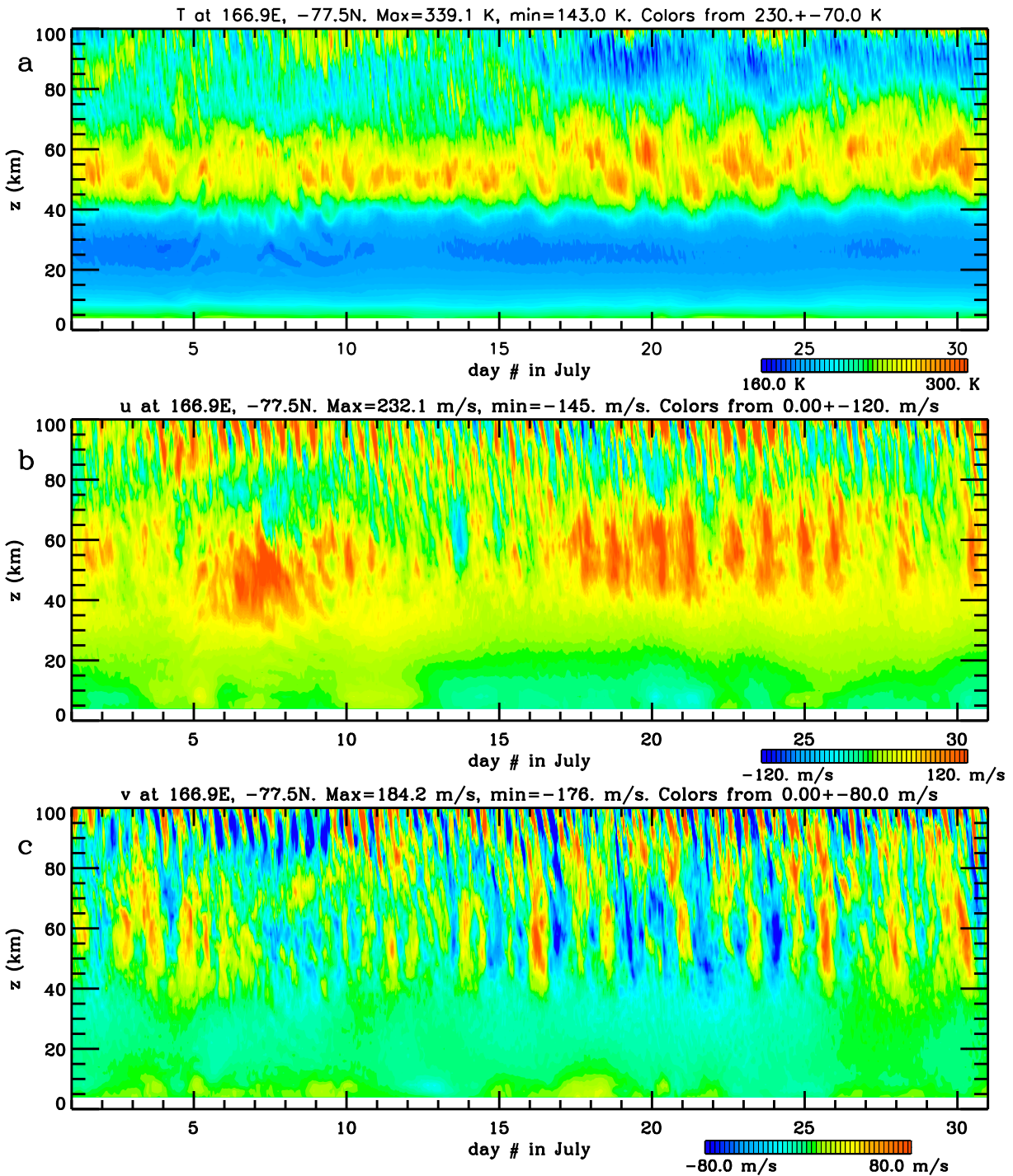


Figure 1. Temperature T (a), zonal velocity u (b), and meridional velocity v (c) at McMurdo during July from the Kühlungsborn Mechanistic general Circulation Model. Maximum and minimum values are shown at the top of each panel.

GWs are ubiquitous in Figure 3 and have both upward and downward phases in time. As we show in section 4.2.2, the large-amplitude, upward-propagating GWs with upward phases in time at $z < 50$ km on 5 July are MWs that traveled through a “ramp-up” (acceleration) of the background eastward wind. (Upward-propagating MWs with upward phases in time are also seen in Figure 3 of Watanabe et al., 2006.) Although GWs are easily visible for $z < 60$ km, it is difficult to see them for $z > 60$ km. Figure 4 shows the scaled perturbations at $z = 80\text{--}100$ km. The scaled GW amplitudes are about 10 times smaller than at $z < 50$ km.

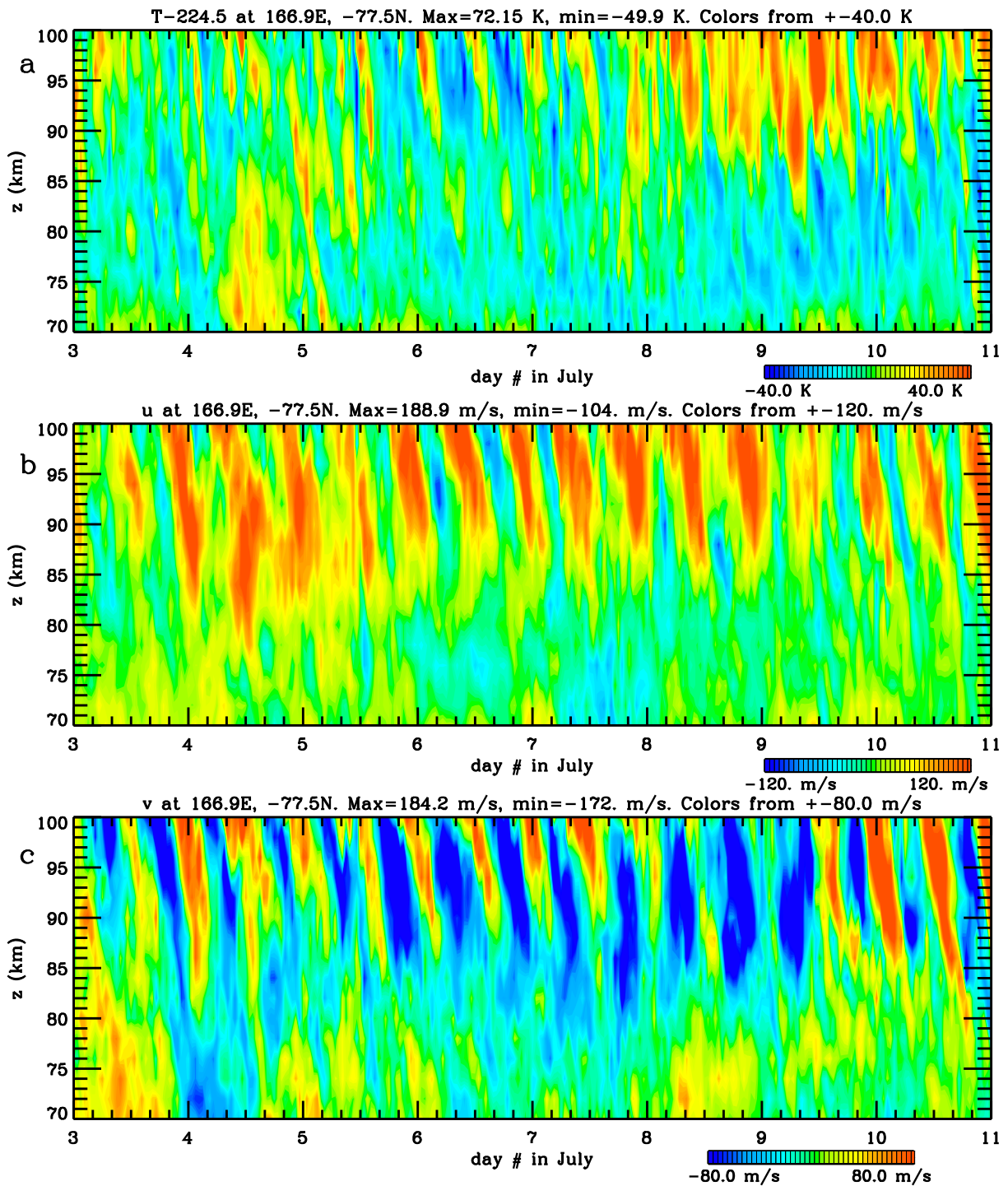


Figure 2. Same as in Figure 1, but for 3–11 July at $z = 70$ – 100 km. Additionally, (a) shows $T - 224.5$ K, where 224.5 is the average temperature at $z = 90$ km for this time period.

This suggests that severe wave dissipation occurs at $z \sim 50$ – 80 km, in agreement with lidar and satellite observations (Lu et al., 2015; Preusse et al., 2006). Figure 4 also shows that the GW amplitudes are somewhat more uniform in time at $z = 80$ – 100 km than at $z < 60$ km. Finally, the GW vertical wavelengths are much larger here than in the stratosphere. Figures 3, 4 show that GWs are ubiquitous at all altitudes and times at McMurdo and have amplitudes that vary strongly with altitude and time.

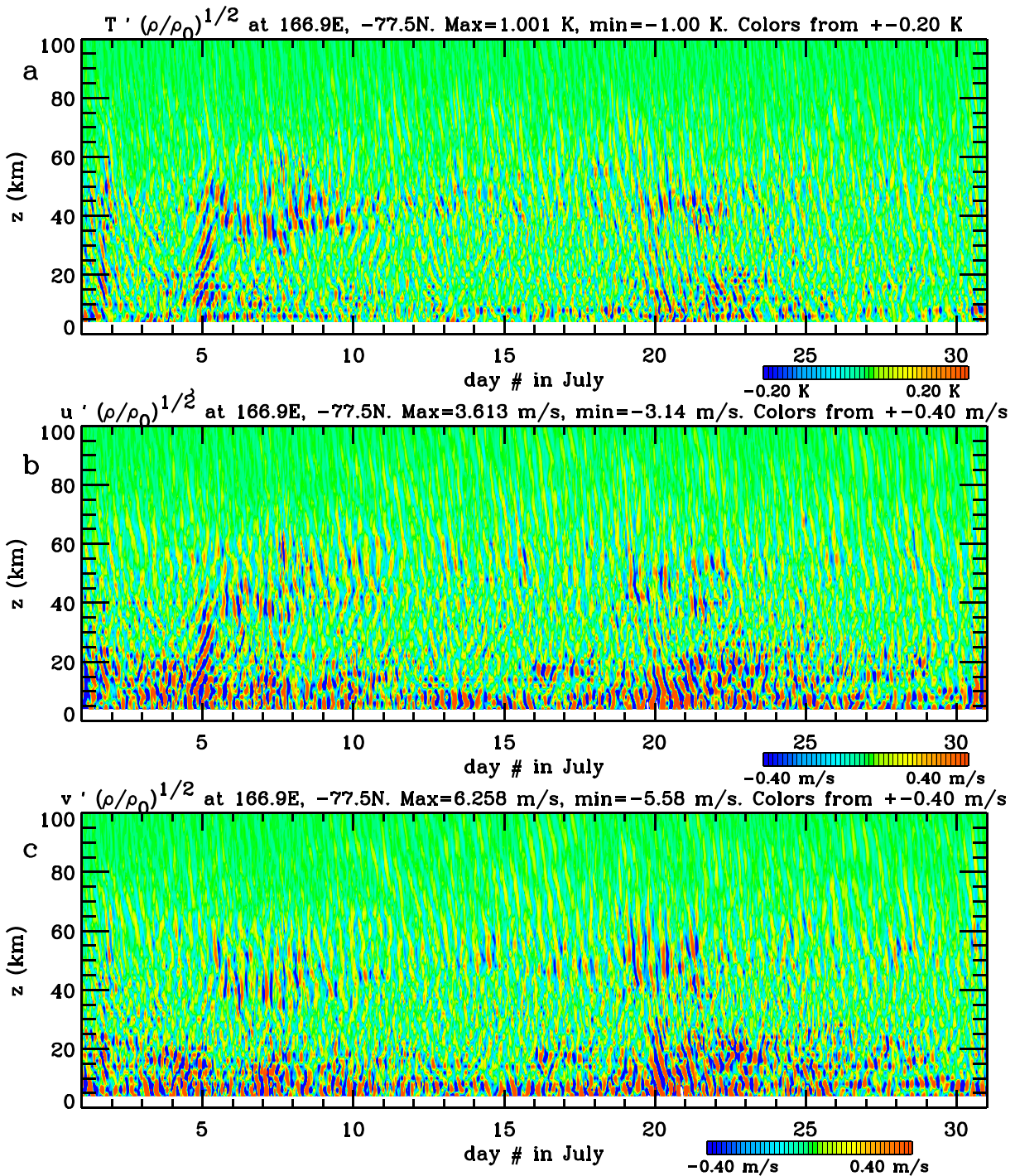


Figure 3. Scaled perturbations at McMurdo obtained via removing waves with $\tau_r > 11$ hr from Figure 1 and multiplying by $\sqrt{\bar{\rho}/\bar{\rho}_0} \cdot T' \sqrt{\bar{\rho}/\bar{\rho}_0}$ (a), $u' \sqrt{\bar{\rho}/\bar{\rho}_0}$ (b), and $v' \sqrt{\bar{\rho}/\bar{\rho}_0}$ (c). Maximum and minimum values are shown at the top of each panel.

Although it is somewhat difficult to see, the scaled GW horizontal velocity amplitudes, $\sqrt{\bar{\rho}/\bar{\rho}_0} u'$ and $\sqrt{\bar{\rho}/\bar{\rho}_0} v'$, are relatively constant in time for $z \leq 10$ km in Figure 3, with phase lines that are typically downward in time. For $10 < z < 20$ km, however, these amplitudes vary significantly in time because of strong wave events, and the phase lines can be upward in time (e.g., on 5 July) or downward in time (e.g., on 9 and 20–22 July). Strong wave events occur on 4–10 and 19–23 July. During these times, GWs with large amplitudes are visible

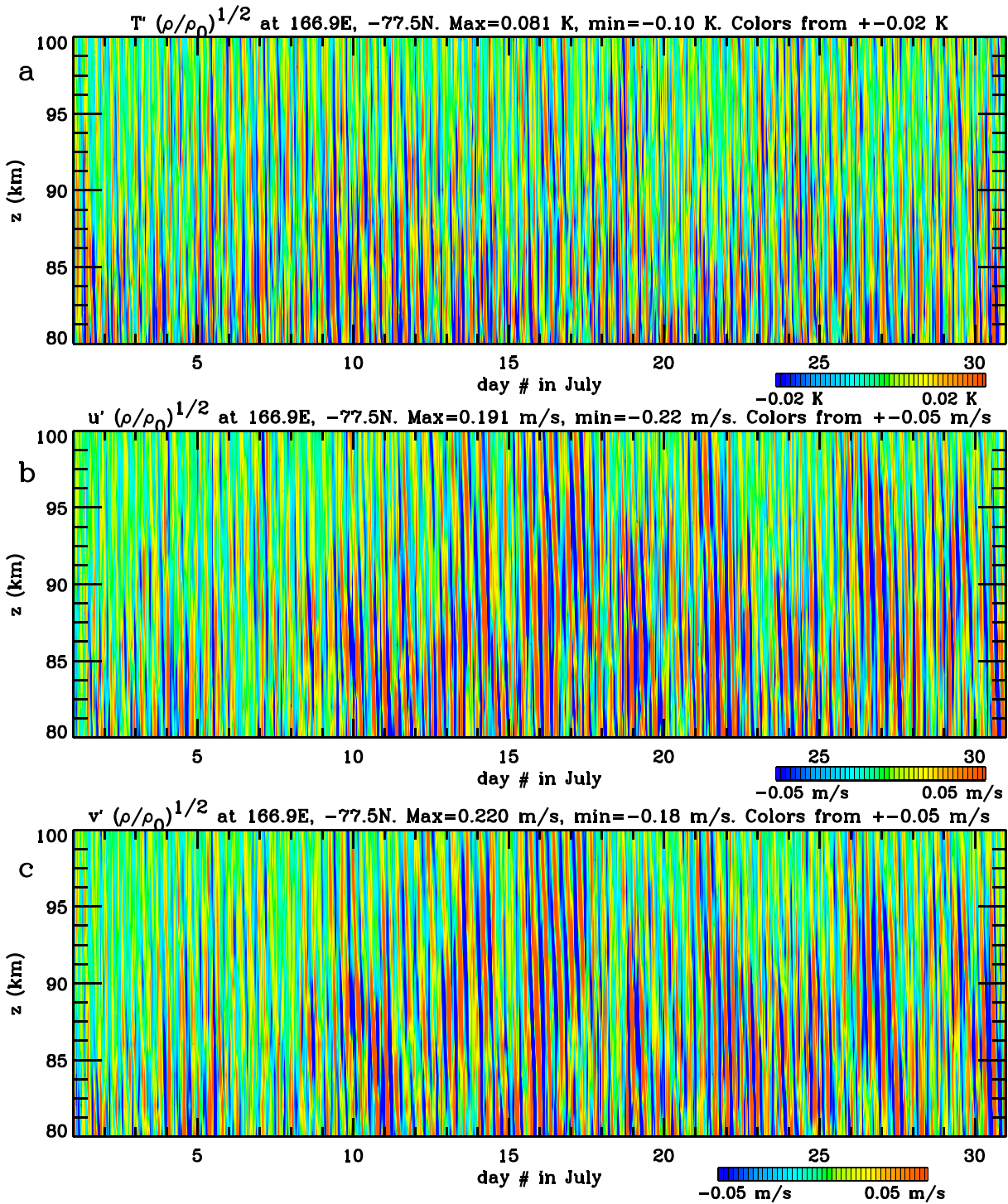


Figure 4. Same as in Figure 3 but for $z = 80\text{--}100$ km and using different color scales.

at $z \sim 5\text{--}60$ km. Comparing with Figure 4, however, this enhanced GW activity at $z < 60$ km does not appear to continue into the mesosphere, although there is some variation in the GW activity in the MLT.

4. Wave Activity on 3–11 July at McMurdo

We now analyze the GW activity at McMurdo on 3–11 July in detail. This period contains several strong events whereby large-amplitude GWs are present from the troposphere to $z \sim 60$ km (see Figure 3).

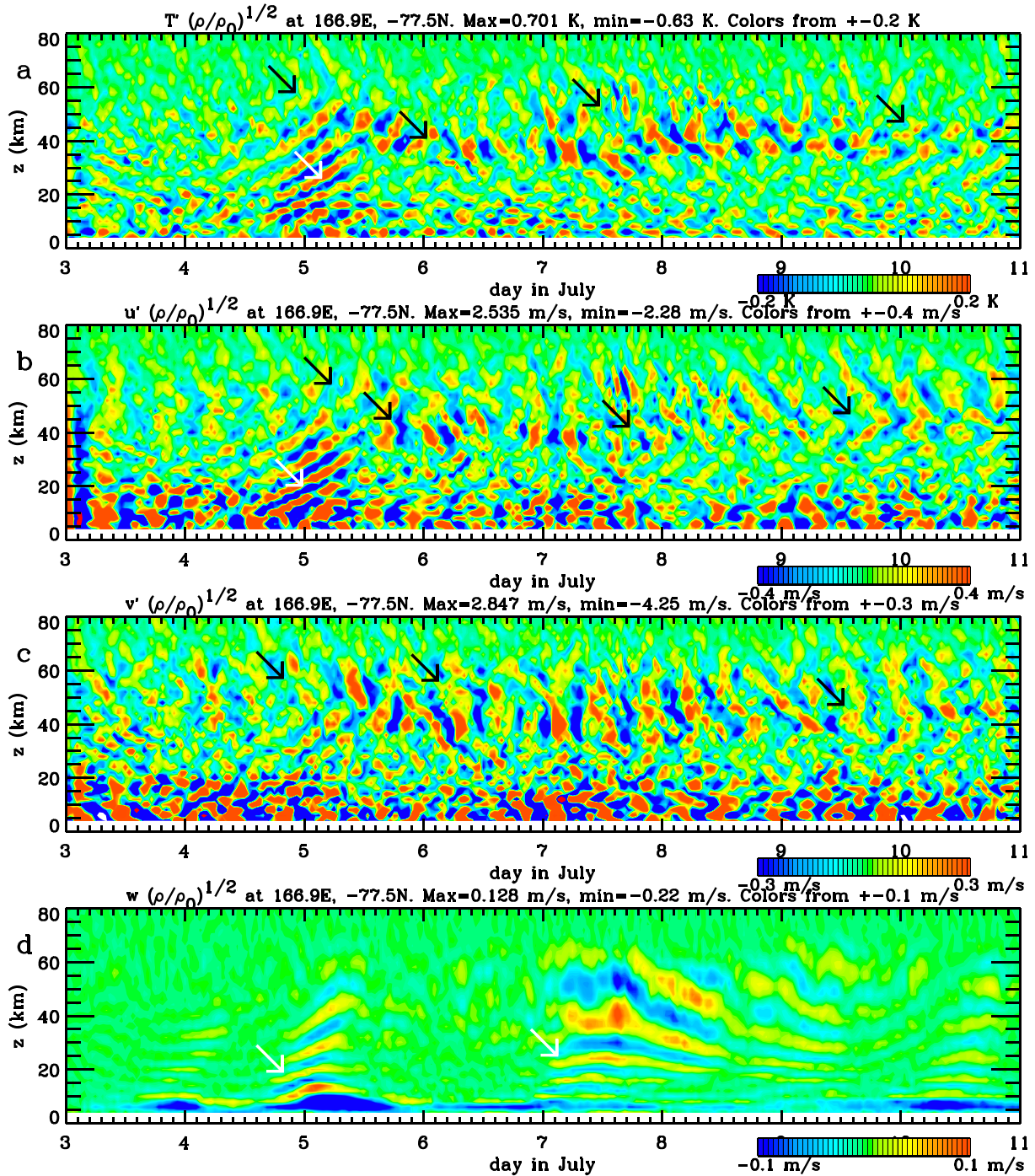


Figure 5. Scaled variables at McMurdo for 3–11 July. $T' \sqrt{\rho/\rho_0}$ (a), $u' \sqrt{\rho/\rho_0}$ (b), $v' \sqrt{\rho/\rho_0}$ (c), and $w \sqrt{\rho/\rho_0}$ (d). White and black arrows show the locations and times for select mountain wave events and fishbone structures, respectively. Maximum and minimum values are shown at the top of each panel.

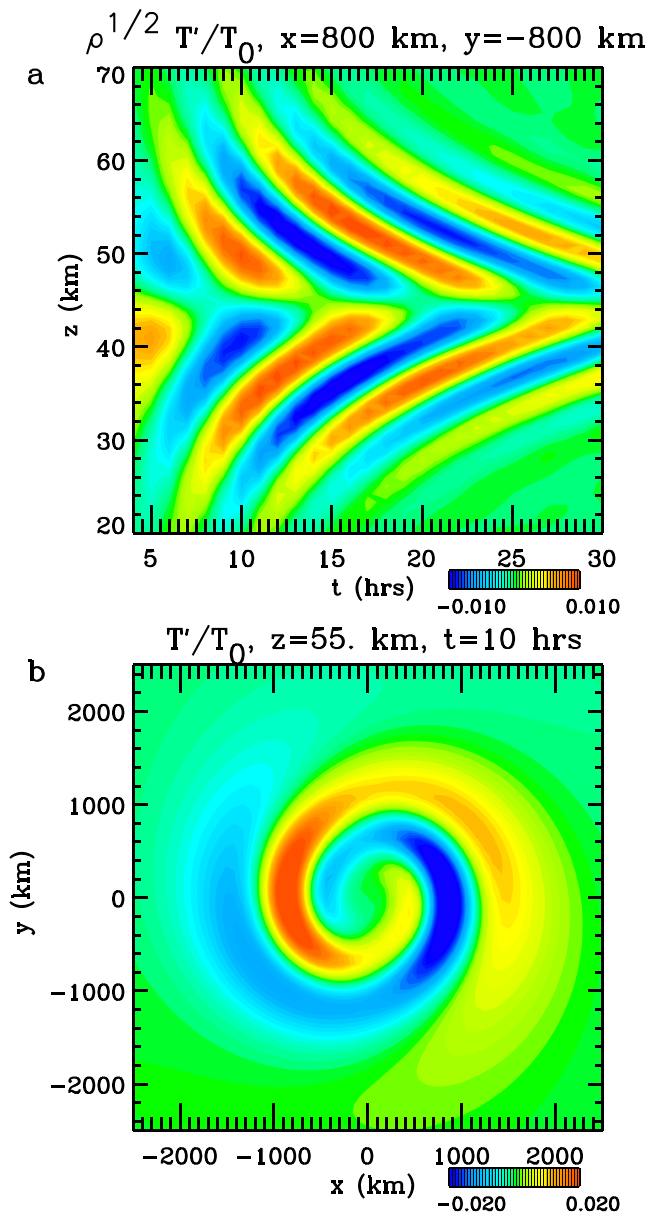


Figure 6. Theoretical compressible solution of the secondary gravity waves excited by a zonal body force centered at $x = y = 0$ and $z = 45$ km in an isothermal, windless atmosphere. The body force begins at $t = 0$ and has full horizontal width $D_H = 800$ km, full depth $D_z = 8$ km, and duration $\chi = 6$ hr. (a) Height-time cross section of the scaled temperature perturbation, $\sqrt{\bar{\rho}} T' / \bar{T}$ (colors), at $x = 800$ km and $y = -800$ km. The altitude of the knee of the structure is at the force center (i.e., $z_{\text{knee}} = 45$ km). (b) Horizontal cross section of T' / \bar{T} at $z = 55$ km and $t = 10$ hr.

4.1. Overview of the Primary and Secondary GWS at McMurdo

Figure 5 shows T' , u' , v' , and w scaled by $\sqrt{\bar{\rho}/\bar{\rho}_0}$ on 3–11 July, where w is the vertical velocity. Here $\bar{\rho}_0 = 868 \text{ gm/m}^3$ is the value of $\bar{\rho}$ at 0°E , 90°S and $z = 5$ km on 3 July at 0 UT for this and all remaining KMCM figures in this paper. Here we show the scaled w rather than the scaled w' in order to see all waves (including those with periods ≥ 11 hr). On 4 July at 18 UT through 5 July at 12 UT, coherent GWs with upward phases in time are seen at $z \sim 10$ – 50 km in T' , u' , and w (see white arrows at $z \sim 20$ km). As we will see in section 4.2.2, these are upward propagating MWs created by a downslope wind; the upward phases occur because the background eastward wind “ramps up” (accelerates) during this event. At $z < 10$ km, the GWs primarily have downward phases in time.

Figure 5d includes three distinct events in w : 4.5–6 July, 7–9.5 July, and 9.5 July to at least 11 July. The durations of these events, 1.5–2.5 days, is consistent with Watanabe et al. (2006) who found that typical downslope wind events lasted for ~ 1 – 4 days near McMurdo.

We overlay black arrows at $z \sim 40$ – 60 km in Figure 5 to highlight a few locations where “fishbone” (or “>”) structure is seen in the perturbations. A fishbone structure is particularly clear in u' at 12 UT on 9 July through 12 UT on 10 July at $z \sim 40$ – 60 (see Figure 5b). This fishbone structure looks very similar to the theoretically derived structure that arises from secondary GWs excited by a body force (see below).

To illustrate this point, we solve the linear, f -plane compressible fluid equations given by Vadas (2013) and show the analytical solution for the secondary GWs and mean response created by an idealized Gaussian zonal body force centered at $z = 45$ km. We assume that the body force is 800 km wide, is 8 km deep, lasts for 6 hr, and has an amplitude of $40 \text{ m}\cdot\text{s}^{-1}\cdot\text{day}^{-1}$. We also assume an isothermal background atmosphere with $\bar{T} = T_0 = 231$ K, resulting in a buoyancy frequency of $N_B = 0.02 \text{ rad/s}$ and $\bar{\rho} = \bar{\rho}_0 \exp(-z/H)$ with $H = 6.9$ km, where H is the density scale height. Further details concerning this theoretical solution can be found in Vadas et al. (2018). In Figure 6a, we show $\sqrt{\bar{\rho}} T' / \bar{T}$ for a horizontally fixed observer $\sqrt{2} \times 800 = 1,130$ km south-east of the center of the body force. A striking fishbone structure appears in this $z - t$ plot; it is created as different spectral components of the excited secondary GWs propagate away from the body force with different horizontal and vertical velocities. This structure is asymmetric in z about $z = 45$ km (which we dub the *knee* of the structure), with upward-propagating GWs having downward phases in time above the knee and downward-propagating GWs having upward phases in time below the knee. Importantly, the upward and downward secondary GWs have the same amplitudes at the excitation altitude; it is only when they propagate away from the body force that the downgoing GW amplitudes decrease as $1/\sqrt{\bar{\rho}}$, while the upgoing GW amplitudes increase as $1/\sqrt{\bar{\rho}}$. Note that the fishbone structure is visible in any horizontal direc-

tion except perpendicular to the force direction (Vadas et al., 2018). Figure 6b shows T' / \bar{T} at $z = 55$ km and $t = 10$ hr. Partial concentric rings are visible and are asymmetric about the axis perpendicular to the force direction (i.e., $x = 0$ here); these partial rings appear to radiate away from the force center in time (not shown). The amplitude of the fishbone structure maximizes in the direction parallel or antiparallel to the body force (i.e., $y = 0$ here) and is 0 in the direction perpendicular to the body force (i.e., $x = 0$ here). We show in section 4.3 that the GWs in the fishbone structures in Figure 5 are indeed secondary GWs and that they are excited by the body forces created by MW dissipation.

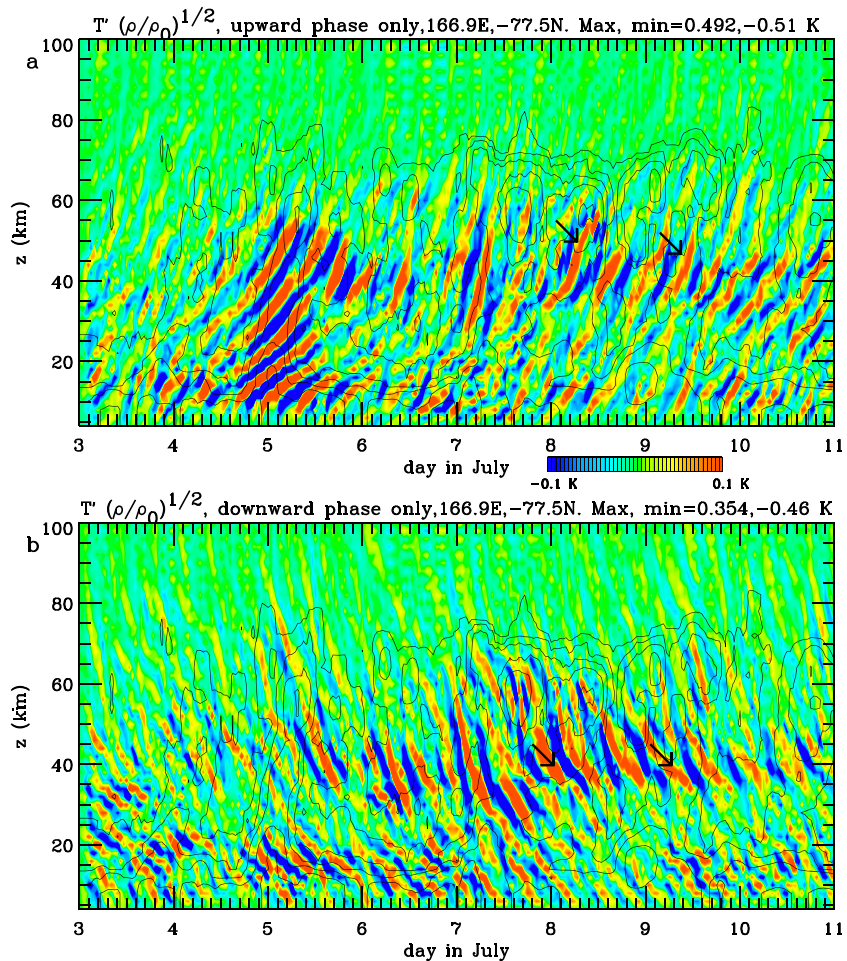


Figure 7. Scaled temperature perturbations, $T' \sqrt{\bar{\rho}/\bar{\rho}_0}$, at McMurdo. (a) Upward phases in time. (b) Downward phases in time. Solid black contours show the dissipation rate multiplied by $\bar{\rho}/\bar{\rho}_0$ at the values $0.015 \times (0.003, 0.01, 0.03, 0.1, 0.3, 1.)$ K/day. Black arrows show select bursts of upward- and downward-propagating gravity waves.

We separate the GWs with upward and downward phases in time by performing a 2-D fast Fourier transform (FFT) in z and t on the scaled temperature perturbations in Figure 5a, separating out the wave components, and then applying the inverse FFTs. Figures 7a and 7b show the scaled temperature perturbations for GWs having upward and downward phases in time, respectively. Coherent wave packets are seen. On 4.0–6.0 July, the MWs in Figure 7a have $\lambda_z \sim 5$ –12 km and $\tau_r \sim 5$ –9 hr at $z \sim 30$ –50 km, consistent with observations (Zhao et al., 2017). Additionally, λ_z increases with altitude, because the westward MWs propagate into an increasing eastward wind (see Figure 1b and section 4.2.1). (Note that a medium-scale MW observed in DEEPWAVE had $\lambda_z \sim 10$ km at $z < 30$ km and $\lambda_z \sim 20$ –30 km at higher altitudes [Bossert et al., 2015].)

In the regions where fishbone structures occur (i.e., $z \sim 30$ –60 km on 5.25–6.5 and 9.5–10.5 July in Figure 5), Figure 7 shows “bursts” of simultaneously occurring upward- and downward-propagating GWs with similar τ_r and λ_z that originate at $z \sim 35$ –50 km, highlighted with black arrows (e.g., at 8.0–10.0 July). In fact, our Fourier decomposition shows that such upward- and downward-propagating waves are persistent during the whole period from 5.5 to 11 July at $z \sim 30$ –60 km. (The GWs with downward phases in time are persistent from earlier: 4.0 July.) The scaled amplitudes of these waves strongly decrease with decreasing z below ~ 30 km; the stratospheric waves are separated from the waves in the troposphere. Thus, the stratospheric GWs seen in Figure 7 from 5.5 to 11 July are most likely secondary waves that are generated by the intermittent body forces created by dissipating primary GWs. The black contour lines in Figure 7 show the scaled dissipative (frictional) heating rate, indicating regions of dynamically unstable GWs. (The frictional heating rate indicates dynamically unstable GWs because the diffusion coefficients in the KMCM are scaled by a criterion of dynamic instability.) The structure of the dissipation rate suggests that the first burst of upward- and downward-propagating waves in the stratosphere is induced by the breakdown of the transient MWs having

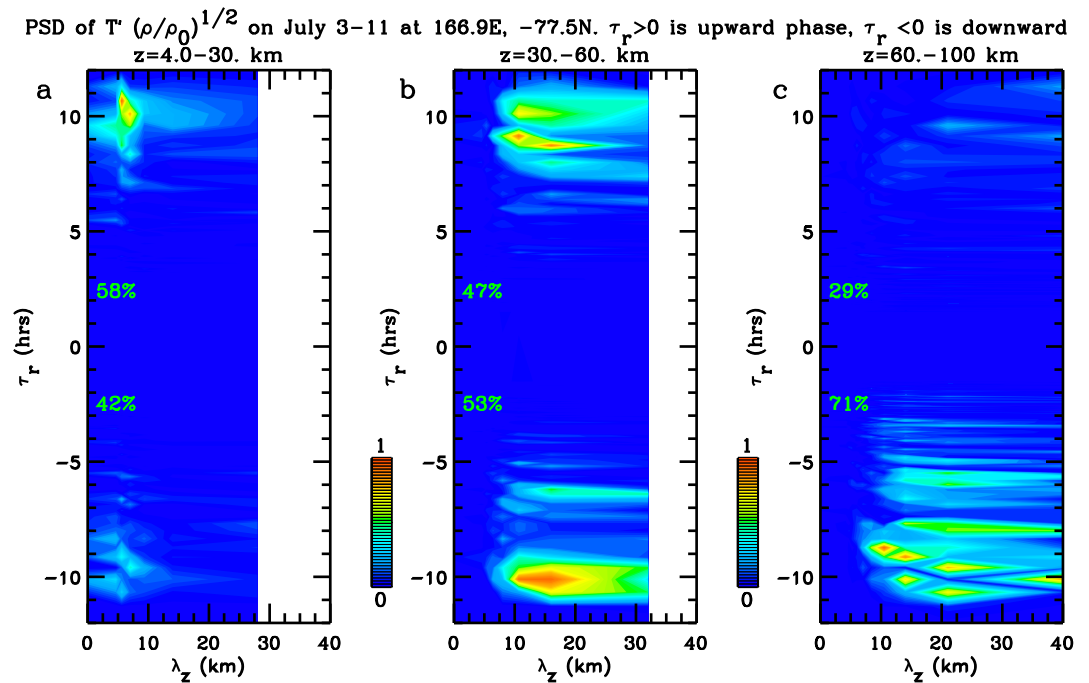


Figure 8. Power spectral density (PSD) of the scaled temperature perturbation, $|T' \sqrt{\rho/\rho_0}|^2$, at McMurdo during 3–11 July. (a) $z = 4\text{--}30$ km. (b) $z = 30\text{--}60$ km. (c) $z = 60\text{--}100$ km. The quadrants are combined so that gravity waves (GWs) with upward phases in time are shown for $\tau_r > 0$, and GWs with downward phases in time are shown for $\tau_r < 0$. Each panel is scaled by its (arbitrary) maximum value. Yellow labels show the percentage of the integrated PSD in GWs with upward phases in time (at $\tau_r > 0$) and downward phases in time (at $\tau_r < 0$).

upward phase propagation (around 5 July). The strong dissipation in the stratosphere after about 7 July is due to MWs that are approximately stationary and are therefore visible in Figure 5d, but are not visible in Figures 5a, 5b, 5c and 7 due to our filtering in frequency space (since only periods < 11 hr are included; e.g., see section 4.3.2).

Figure 8 shows the power spectral density (PSD) of the scaled temperature perturbations, $|T' \sqrt{\rho/\rho_0}|^2$, for 3–11 July. Here the “ \sim ” denotes taking the 2-D FFT. The PSD produces power in all four quadrants ($\pm m, \pm \omega_r$), where $m = -2\pi/\lambda_z$ is the vertical wave number and $\omega_r = 2\pi/\tau_r$ is the ground-based frequency. The spectrum is symmetric regarding the sign of $m\omega_r$, where $m\omega_r > 0$ (< 0) indicates upward (downward) phase propagation. We combine the GWs from the two quadrants with $m > 0$ and show the GWs with upward phases in time as $\tau_r > 0$ and those GWs with downward phases in time as $\tau_r < 0$.

In the troposphere and lower stratosphere ($z = 4\text{--}30$ km), Figure 8a shows that 58% (42%) of the GWs have upward (downward) phases in time with $\tau_r \sim 9\text{--}11$ hr and $\lambda_z \sim 4\text{--}9$ km. These GWs include MWs and IGWs from unbalanced flow associated with large Rossby-wave amplitudes (this process is often called *spontaneous emission* in the literature). In the stratosphere ($z = 30\text{--}60$ km), 47% (53%) of the GWs have upward (downward) phases in time. These GWs have a larger range of periods and vertical wavelenghts, $\tau_r \sim 7\text{--}11$ hr and $\lambda_z \sim 6\text{--}30$ km and include MWs, secondary GWs (see section 4.3), and IGWs from unbalanced flow. In the upper stratosphere and mesosphere ($z = 60\text{--}100$ km), only 29% of the GWs have upward phases in time. Seventy-one percent of the GWs have downward phases in time, with $\tau_r \sim 3\text{--}11$ hr and $\lambda_z \sim 9\text{--}40$ km. We show in section 4.4 that these latter GWs are mainly upward-propagating secondary GWs. We note that some of the downward-propagating GWs might be reflected GWs. However, Sato et al. (2012) showed that only 10% of the GWs reflect from a jump in N_b^2 in the southern winter stratosphere in their hydrostatic KANTO model and that the reflected GWs are quite weak. Because the KMCM is also hydrostatic and is similar to the KANTO model regarding numerical methods and applied resolution, it is possible that few of the downward-propagating GWs here are reflected GWs.

The percentage of GWs with downward phases in the stratosphere is 53% from Figure 8b. This is significantly smaller than the 70.4% measured by Zhao et al. (2017) at 30–50 km during the McMurdo winter. We also note from Figures 8b and 8c that the peak periods are $\tau_r \sim 4\text{--}10$ hr, which are somewhat longer than

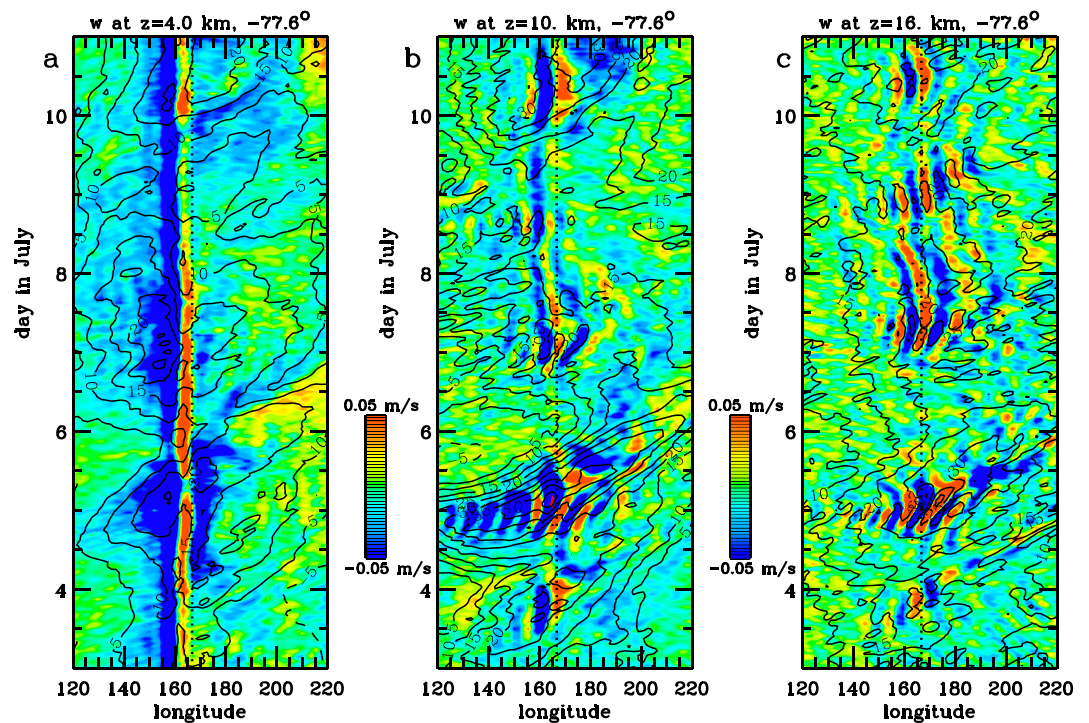


Figure 9. The vertical velocity, w , (color contours) at 77.6°S as a function of longitude and time at $z = 4$ km (a), 10 km (b), and 16 km (c). Solid (dashed) lines show positive (negative) zonal wind, u , in 5-m/s intervals at the same altitudes. The dotted lines show the location of McMurdo.

in the observations (Chen et al., 2016; Zhao et al., 2017), although our peak λ_z agrees well with these observations. These differences might occur because (a) we included the PSD from all GWs (rather than selecting only the largest-amplitude GWs), (b) we only included the PSD from GWs during a large MW event (rather than including all the data for the entire winter), and (c) we utilized a somewhat larger vertical range. Also note that Yamashita et al. (2009) found that 51% and 62% of the stratospheric GWs had downward phase progression in the winter at the South Pole and Rothera Stations, respectively.

4.2. Primary GWS at McMurdo: Mountain Waves and Inertia-GWS

4.2.1. MWS and IGWS in the Troposphere and Stratosphere

In Figure 9a, we show w at 77.6°S and $z = 4$ km as a function of longitude and time. A narrow band containing one or two upward/downward cycles of a strong quasi-stationary MW are seen slightly west of McMurdo. To understand how these MWs are created, we also show the zonal wind u at $z = 4$ km. We see that the strong quasi-stationary MWs have large amplitudes when the wind is eastward with $u > 10$ m/s, such as occurs on 5.0 July. In Figure 10a, we show a stereographic projection of w at $z = 4$ km on 5.0 July. The phase lines of the MWs are parallel to the coastline at McMurdo (i.e., northwest to southeast). Therefore, we conclude that the narrowband of strong MWs created near McMurdo in Figure 9a are created by a downslope wind that flows downslope from the Transantarctic Mountains to the Ross Sea, as first modeled by Watanabe et al. (2006). Note that Watanabe et al. (2006) found that the MWs have $\lambda_H \sim 220$ km and $\lambda_z \sim 11$ km and that the near-surface zonal wind speed needed to be > 13 m/s to excite these MWs, which agrees well with our results. We also see in Figure 9a that the MW amplitude increases rapidly to $w \sim 0.05\text{--}0.1$ m/s on 4.5 July; this corresponds to the beginning of one of the strong MW events in Figure 5.

In Figures 9b and 9c, we show w and u at $z = 10$ and 16 km, respectively. Here the quasi-stationary MWs have $\lambda_H \approx 230$ km and are broken up into distinct wave packets, which extend upstream (windward) and downstream (leeward) from McMurdo with 2–5 cycles zonally. Note that Plougonven et al. (2008) modeled the MWs excited by wind flow over the Antarctic Peninsula during a strong event and found that the MWs are located upstream and downstream of the mountain. Walterscheid et al. (2016) studied the MWs excited by wind over the Antarctic Peninsula and found that steady state flow creates upstream MWs that tilt into the wind. They also found that the downstream MWs mainly correspond to high-flux wave events

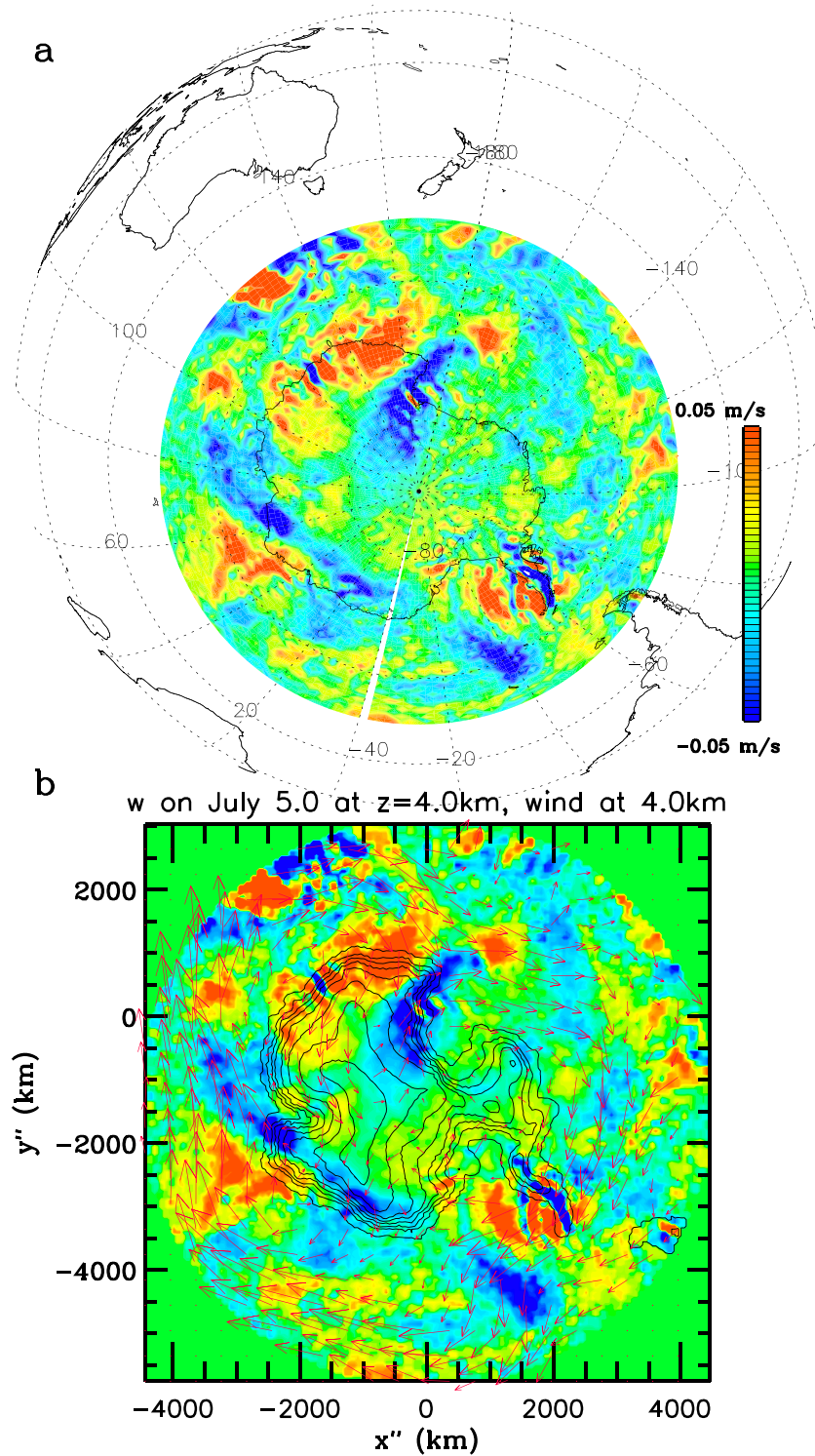


Figure 10. The vertical velocity w at $z = 4$ km on 5.0 July (color contours). (a) w using a stereographic projection. McMurdo is south of New Zealand, just west of 180° longitude. (b) w on a 2-D plane parallel to the Earth's surface at McMurdo using the transformation from Appendix B. McMurdo is located at $x'' = y'' = 0$. The horizontal wind u_H is shown at $z = 4$ km with red arrows, with lengths proportional to the maximum horizontal wind of $u_H = 60$ m/s. The height of the topography above sea level is shown as black lines in 0.5-km intervals from 50 m.

and are therefore likely associated with transient flow. Finally, Sato et al. (2012) found leeward advection of MWs that extended thousands of kilometers over the southern Andes and Antarctica Peninsula because of the mean wind component perpendicular to the GW wave number vector (Preusse et al., 2002).

The segmentation of the quasi-stationary MWs into distinct wave packets is seen to be caused by the change in u in Figures 9b and 9c; when the eastward wind intensifies in the upper troposphere and lower stratosphere, the MWs intensify because λ_z increases (see below), which allows them to propagate to higher altitudes. We see this relationship as follows. The dispersion relation for midfrequency GWs with $|\lambda_z| \ll 4\pi\mathcal{H}$ is

$$\omega_{lr} = N_B k_H / m, \quad (2)$$

where k , l , and m are the zonal, meridional, and vertical wave numbers, respectively, and $k_H = \sqrt{k^2 + l^2} = 2\pi/\lambda_H$. The intrinsic frequency is

$$\omega_{lr} = \omega_r - kU - lV = \omega_r - k_H U_H, \quad (3)$$

where U and V are the zonal and meridional background wind components and $U_H = (kU + lV)/k_H$ is the horizontal wind speed along the direction of propagation of the GW. Rearranging equation (3), we obtain

$$\lambda_z = \frac{2\pi(c_H - U_H)}{N_B} = \frac{2\pi c_{lH}}{N_B}, \quad (4)$$

where $c_H = \omega_r/k_H$ and $c_{lH} = c_H - U_H$ is the intrinsic horizontal phase speed. Since $c_H = 0$ for an MW generated by a steady state wind, the intrinsic horizontal phase speed of the MW is opposite to the wind, $c_{lH} = -U_H$ (i.e., westward if the wind is eastward). Additionally,

$$|\lambda_z| = \frac{2\pi|U_H|}{N_B}. \quad (5)$$

Thus, $|\lambda_z|$ is proportional to the background wind (e.g., Alexander & Teitelbaum, 2007). If $|U_H|$ increases with altitude, then $|\lambda_z|$ increases as well, thereby allowing the MWs to propagate to higher altitudes before dissipating.

We now check the consistency of the KMCM model data with equation (5). We set $N_B \sim 0.01$ rad/s in the troposphere. From Figures 9a and 1, we estimate $U \sim 10$ m/s and $V \sim 0$, respectively, which yields $\lambda_z = 6$ km from equation (5). This value is consistent with $\lambda_z \sim 6-7$ km from our model data in Figures 7a and 8a.

We now wish to accurately determine the horizontal scales, phase speeds, and propagation directions of all GWs at McMurdo, including those with small amplitudes. This is difficult to accomplish near the pole in geophysical coordinates, because the distance between adjacent longitudinal grid points decreases rapidly near the pole. Although the MW parameters can be estimated from stereographic projections when they have large amplitudes (e.g., Figure 10a), it is difficult to determine the parameters of smaller-amplitude GWs (such as IGWs and secondary GWs), because they cannot be easily identified “by eye” in these figures.

Here we introduce a new technique that enables Fourier filtering in the horizontal direction in order to isolate, identify, and quantify the parameters of all GWs. We first transform from geophysical coordinates to Cartesian coordinates on a 2-D plane that is tangent to Earth at the desired location using a series of rotations, dot products and cross products. This transformation is described in Appendix B. We then create an equally spaced grid on this 2-D plane and populate the cells with interpolated values from the model data. Figure 10b shows the results of transforming w from Figure 10a onto a 2-D plane that is tangent to Earth at McMurdo. This 2-D plane has coordinates (x'', y'') and grid spacings $\Delta x'' = \Delta y'' = 50$ km. McMurdo is located at $x'' = y'' = 0$. Positive x'' (y'') corresponds to the geophysical eastward (northward) directions at McMurdo only. Comparing with Figure 10a, we see that this transformation technique works quite well, even $\sim 4,000$ km from McMurdo. Note that we can easily see the MWs excited parallel to the coastline at McMurdo.

In addition to w , we overlay vectors showing the horizontal wind, $u_H = \sqrt{u^2 + v^2}$, at $z = 4$ km in Figure 10b, as well as the topography in 0.5-km intervals. (Note that the wind vector is transformed to this 2-D plane via equation (B11).) The wind at McMurdo is northeastward during this event. Additionally, the MWs begin part-way down the slope, before the downslope wind reaches the Ross Sea. Supporting information A shows a movie of u_H at $z = 4$ km (vectors) and w at $z = 16$ km (colors) during 3–11 July. We see large-scale swirls within the baroclinic waves that create temporally and spatially variable wind around and over Antarctica. When the wind amplitude is small, upslope, or parallel to the coastline, MWs are not seen at McMurdo. However, when the wind is strong and has a large eastward component (i.e., downslope), MWs are generated

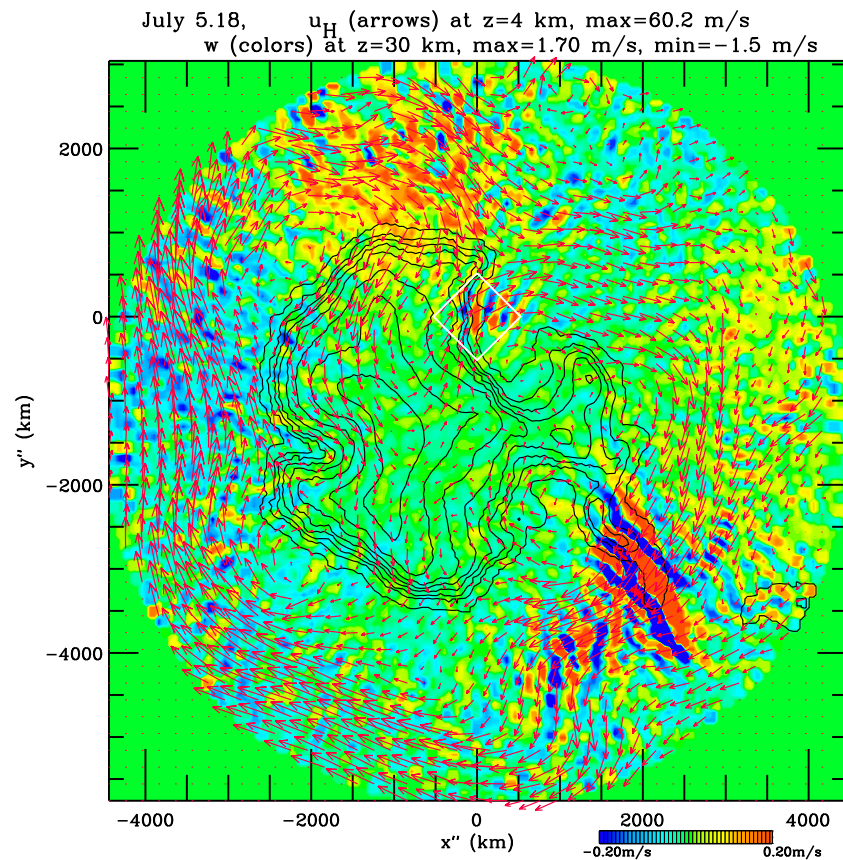


Figure 11. The vertical velocity, w , (color contours) at $z = 30$ km and the horizontal wind, u_H , (red arrows) at $z = 4$ km on 5.18 July on a 2-D plane centered at McMurdo. The maximum value of u_H is 60 m/s. The height of the topography above sea level is shown as black lines in 0.5-km intervals from 50 m. The center of the white diamond is McMurdo. Maximum and minimum values of w are shown at the top.

at McMurdo. Multiple significant events occur at McMurdo on 4.8–5.4, 6.9–8.6, 9.0–9.6, and 10.3–10.8 July. Although the first event continues after 5.4 July, the MWs are swept downstream (eastward), out of McMurdo’s field of view. The large-scale horizontal wind in Figure 10b is caused by synoptic-scale weather systems that are comprised of baroclinic Rossby waves. These waves move in vortex-like patterns around the circumpolar ocean surrounding Antarctica and also extend onto the Antarctic continent.

In Figures 9b and 9c, the baroclinic waves (seen in the zonal wind) are strong at $z = 10$ km but are weak by $z = 16$ km. This is because the Rossby waves do not propagate into the stratosphere but grow to large amplitudes in the troposphere, thereby generating horizontal accelerations/decelerations that lead to unbalanced flow and the excitation of IGWs (O’Sullivan & Dunkerton, 1995; Plougonven & Zhang, 2014; Zhang, 2004). Because the Rossby waves are strongest over the circumpolar ocean (Hendricks et al., 2014), IGW generation from this mechanism is stronger there than over the Antarctic continent. These IGWs appear as mesoscale fine structure (shorter than $\sim 1,000$ km) in w within the circumpolar ocean surrounding Antarctica (see supporting information A). These IGWs make up for $\sim 33\%$ of the total density-weighted zonal mean momentum flux (Vincent et al., 2007). Note that Wu and Jiang (2002) also observed substantial GW momentum flux over the oceans surrounding Antarctica, although they did not diagnose their source. Finally, Plougonven et al. (2008) showed that upward-propagating IGWs are created in the lower stratosphere from the breaking of a large-amplitude MW; they postulated that these are larger-scale secondary GWs from body forces from MW breaking.

Figure 11 shows u_H (vectors) at $z = 4$ km and w at $z = 30$ km on 5.18 July. The MWs excited by the northeastward downslope wind propagate to the stratopause region (see Figure 7a) and still have phase lines parallel to the coastline. Additionally, large-amplitude MWs are visible over and in the lee of the Antarctic Peninsula at $x'' \sim 1,000$ – $2,500$ km and $y'' \sim -4,500$ to $-2,000$ km. These MWs have large amplitudes because the

Rossby waves have a strong eastward wind component there. These hotspots (i.e., McMurdo and the Antarctic Peninsula) were observed with the AIRS satellite (Hendricks et al., 2014; Hoffmann et al., 2013) and superpressure balloon experiments (Vincent et al., 2007) and are also a general feature of the KMCM (Becker & Vadas, 2018). We also see some IGWs created from accelerations/decelerations associated with large-amplitude Rossby waves over the circumpolar ocean surrounding Antarctica (Figure 11), although these IGWs are weak at $z > 25$ km (see section 4.2.3).

Supporting information B shows a movie of u_H at $z = 4$ km (vectors) and w at $z = 30$ km (colors) on 3–11 July. Two large MW events reach $z = 30$ km during this time: 5.0–5.5 and 7.1–8.8 July. A smaller event occurs on 9.2–9.7 July. Note that MWs are nearly continuously present above and in the lee of the Antarctic Peninsula, although their locations and amplitudes vary significantly in time. Additionally, MWs from the southern Andes are often visible over the southern part of South America and in the Drake Passage (e.g., on 7.2–11 July).

4.2.2. Mountain Waves With Upward Phases in Time

It is known that a change in the background wind in time creates a change in the ground-based GW frequency ω_r in time (Eckermann & Marks, 1996; Senf & Achatz, 2011). If a GW propagates in the background wind $\mathbf{V}(\mathbf{x}) = (V_1, V_2, V_3) = (U, V, W)$, then the change in its location \mathbf{x} and wave number \mathbf{k} in time t calculated along the raypath is (Lighthill, 1978) as follows:

$$\frac{dx_i}{dt} = V_i + \frac{\partial \omega_r}{\partial k_i} = V_i + c_{g_i}, \quad (6)$$

$$\frac{dk_j}{dt} = -k_j \frac{\partial V_j}{\partial x_i} - \frac{\partial \omega_r}{\partial x_i}, \quad (7)$$

$$\frac{d\omega_r}{dt} = k_i \frac{\partial V_i}{\partial t} + \frac{\partial \omega_r}{\partial t}, \quad (8)$$

where the components of the vector group velocity, \mathbf{c}_g , are $c_{g_i} = \partial \omega_r / \partial k_i$, and

$$\begin{aligned} \frac{\partial \omega_r}{\partial x_i} &= \frac{\partial \omega_r}{\partial N_B} \frac{\partial N_B}{\partial x_i} + \frac{\partial \omega_r}{\partial H} \frac{\partial H}{\partial x_i}, \\ \frac{\partial \omega_r}{\partial t} &= \frac{\partial \omega_r}{\partial N_B} \frac{\partial N_B}{\partial t} + \frac{\partial \omega_r}{\partial H} \frac{\partial H}{\partial t}. \end{aligned} \quad (9)$$

Here the indices $i, j = 1, 2, 3$ indicate the components of the vector quantities $\mathbf{x}, \mathbf{V}, \mathbf{k}$, and \mathbf{c}_g , repeated indices imply a summation, $\partial / \partial k_i$ are computed for fixed \mathbf{x} and t , $\partial / \partial x_i$ are computed for fixed \mathbf{k} and t , and $\partial / \partial t$ are computed for fixed \mathbf{k} and \mathbf{x} .

The MWs excited at McMurdo on 5 July are westward-propagating because they are excited by eastward winds. If the background wind U is constant in time, the GW solution is stationary in time. This is stated mathematically as the GWs having ground-based zonal phase speed $c_x \simeq 0$ and $\omega_r \simeq 0$, where $c_x = \omega_r / k$ is the ground-based zonal phase speed. The MW's intrinsic zonal phase speed, $c_{ix} = c_x - U$, however, is not 0. If U is constant in time, then $c_{ix} \sim -U$. However, if U increases significantly in time (i.e., $\partial U / \partial t > 0$) by the total amount $\Delta U > 0$ over the time Δt , then because $k < 0$ for westward GWs, equations (8) and (9) show that $d\omega_r / dt = k \partial U / \partial t < 0$ (assuming $\partial N_B / \partial t = \partial H / \partial t = 0$). We assume that U is independent of x, y , and z in the region where U increases. After U increases by ΔU , the change in the GW's ground-based frequency (along the raypath) is then

$$\Delta \omega_r \simeq k \Delta U. \quad (10)$$

Since $\Delta U > 0$, this causes ω_r to become negative. Since a GW's phase is $mz - \omega_r t$ (at a fixed location), the slope of the phase line in a $z - t$ plot is

$$\frac{dz}{dt} = \frac{\omega_r}{m}. \quad (11)$$

Therefore, ω_r becoming negative has the result that the upward-propagating MW (negative vertical wave number, positive intrinsic frequency) now has an upward phase in time in the ground-based reference frame (i.e., $\frac{dz}{dt} > 0$). This ramp-up effect was also mentioned in Yamashita et al. (2009). Because this effect involves an acceleration of the background wind, it is somewhat different from the effect that ω_r can have the opposite sign of ω_r if U_H is comparable to or larger than the GW intrinsic phase speed (Fritts & Alexander, 2003).

In addition to the change in ω_r , the MW will also gain a nonzero ground-based phase speed. From equation (10), the total change in c_x along the raypath over the time Δt is

$$\Delta c_x = \Delta \omega_r / k \sim \Delta U. \quad (12)$$

Therefore, a westward MW will gain an eastward ground-based phase speed and an upward phase in time if U increases in time. This will result in the MW being swept downstream in time.

As an example, U increases from 20 to 37 m/s over $\Delta t = 12$ hr on 4.5–5.0 July at $z = 10$ km at McMurdo (see Figure 9b). This yields $\Delta U = 17$ m/s and an average acceleration of $\partial U / \partial t \sim 1.4 \text{ m} \cdot \text{s}^{-1} \cdot \text{hr}^{-1}$. We assume that this increase in U occurs at all heights equally at $z \geq 10$ km. Assuming $\lambda_H = 230$ km and zonal propagation, the total change in the GW's ground-based frequency over Δt (along the GW raypath) for $z \geq 10$ km is $\Delta \omega_r \simeq k \Delta U \sim -4.6 \times 10^{-4}$ rad/s. For $z < 10$ km, the quasi-stationary MW has a downward phase in time (see Figures 5a, 5b, and 7), with $\tau_r \sim 9$ hr (or $\omega_r = 1.9 \times 10^{-4}$ rad/s) and $c_x = -7.1$ m/s. (Note that this MW likely has a nonzero ground-based zonal phase speed because the downslope wind varies in time.) After propagating to $z \geq 10$ km, we estimate a ground-based frequency of $\omega_r \sim (1.9 - 4.6) \times 10^{-4}$ rad/s $\sim -2.7 \times 10^{-4}$ rad/s, which corresponds to $\tau_r \sim -6.5$ hr. This is quite similar to the observed value of $\tau_r \sim -(7-8)$ hr for $z \sim 10-15$ km (see Figures 5a and 5b). Note that the change in sign for ω_r corresponds to a shift from downward to upward phases in time at $z \geq 10$ km (see equation (11)). Additionally, we predict an eastward change in the ground-based zonal phase speed (along the GW raypath) of $\Delta c_x \sim \Delta U \sim 17$ m/s from equation (12), which results in an eastward phase speed of $c_x \sim (-7.1 + 17.0)$ m/s ~ 10 m/s at $z \geq 10$ km. We will see in section 4.2.3 that this estimate for c_x agrees quite well with the model result.

4.2.3. Horizontal Parameters of Primary GWS in the Lower Stratosphere

We now determine the horizontal parameters (i.e., λ_H , c_H , and direction of propagation) of the primary GWs in the lower stratosphere at McMurdo. Figures 12a and 12b show u' at $z = 20$ km on 5.0 July for GWs with upward and downward phases in time, respectively. Large-amplitude MWs with upward phases in time and $\lambda_H \simeq 230$ km are seen at McMurdo. Figures 12c and 12e show "keograms" of u' as functions of time and x'' at $y'' = -22$ km, and Figures 12d and 12f show keograms of u' as functions of time and y'' at $x'' = -0.6$ km. The MWs have large amplitudes of $u' \sim 3$ m/s, $\tau_r \sim 8-9$ hr, and $c_x \sim 9$ m/s on 5.0–5.6 July at $x'' = 0-500$ km (the solid line in Figure 12c highlights an MW phase line). The value of c_x agrees well with the predicted value in section 4.2.2. Additionally, smaller-amplitude IGWs with upward and downward phases in time are seen with $u' \sim 0.5-1$ m/s, $c_x \sim 50$ m/s, $c_y \sim 50$ m/s, and $\tau_r \sim 5-6$ hr (the dashed lines in Figures 12c–12f highlight several IGW phase lines).

The horizontal phase speed of a GW is

$$c_H = \frac{\omega_r}{k_H} = \frac{1}{\sqrt{(k/\omega_r)^2 + (l/\omega_r)^2}} = \frac{1}{\sqrt{1/c_x^2 + 1/c_y^2}}, \quad (13)$$

where c_x and c_y are the speeds of the GW phase in the x and y directions, respectively (e.g., from a keogram): $c_x = \omega_r/k = \lambda_x/\tau_r$ and $c_y = \omega_r/l = \lambda_y/\tau_r$. Since $c_H = \omega_r/k_H = \lambda_H/\tau_r$,

$$\lambda_H = \frac{\tau_r}{\sqrt{1/c_x^2 + 1/c_y^2}}. \quad (14)$$

For the MW (assuming zonal propagation), we predict $\tau_r = \lambda_H/c_x \simeq 7.1$ hr at $z \sim 20$ km, which agrees well with the value obtained from Figure 12c. For the IGWs ($\tau_r \sim 5-6$ hr), we estimate $c_H \sim 35$ m/s from equation (13), and $\lambda_H \sim 600$ to 800 km from equation (14). Note that $\lambda_x = \tau_r c_x \sim \lambda_y \sim 900$ to $1,080$ km. This range of λ_H is typical for IGWs from unbalanced flow associated with large Rossby wave amplitudes (Nicolls et al., 2010; O'Sullivan & Dunkerton, 1995).

We apply 2-D FFTs on selected horizontal slices of u' at $z = 20$ km and extract those GWs with $\lambda_H = 400-2,000$ km in order to remove the large-amplitude MWs. Figure 13a shows the inverse FFT on 4.0 July. Although MWs are no longer present, it is difficult to see the individual GWs because of constructive and destructive interference. Figures 13b and 13c show the result where we filter for $k/l > 0$ (southwestward- or northeastward-propagating GWs) and $k/l < 0$ (northwestward- or southeastward-propagating GWs), respectively, before applying the inverse FFT. GW packets are now easily seen. Rows 2 and 3 show the corresponding results on 5.0 and 6.0 July, respectively. In order to determine the propagation directions of the GW packets,

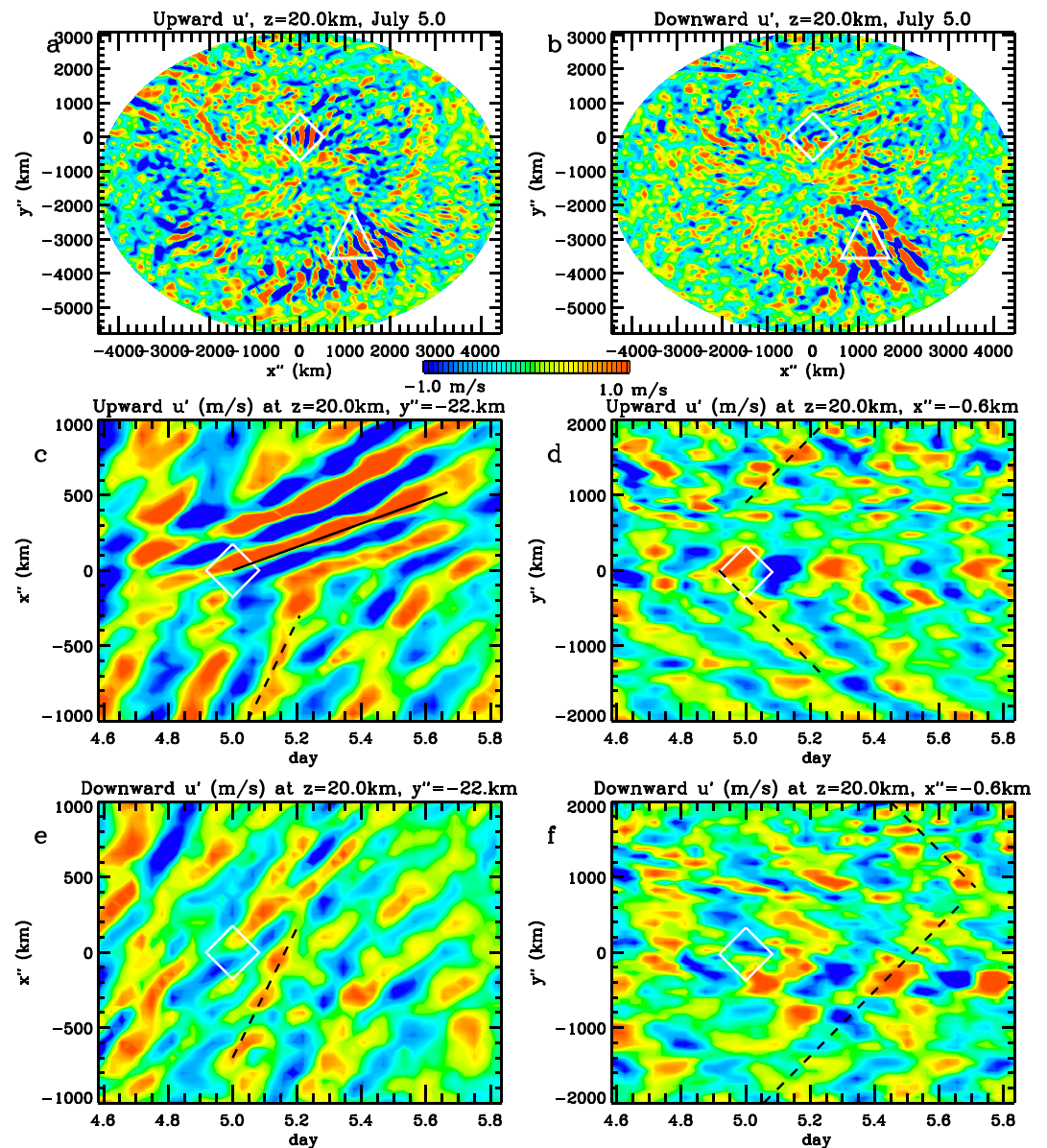


Figure 12. u' at $z = 20$ km on a 2-D plane centered at McMurdo. Gravity waves (GWs) with upward (a) and downward (b) phases in time on 5.0 July. (c) u' as function of time and x'' at $y'' = -22$ km for GWs with upward phases in time. The solid black line shows $c_x = 9$ m/s. (d) u' as function of time and y'' at $x'' = -0.6$ km for GWs with upward phases in time. (e, f) Same as (c) and (d) but for GWs with downward phases in time. The dashed black lines in (c) and (e) show $c_x = 50$ m/s. The dashed black lines in (d) and (f) show $c_y = \pm 50$ m/s. The maximum value in (c) is $u' \sim 3$ m/s. The white diamonds and triangles in (a) and (b) are centered at McMurdo and the Antarctic Peninsula (at 50°W and 73°S), respectively.

we show separate keograms in Figure 14. The IGWs with $k/l > 0$ propagate northeastward on 4.0–4.7 July at McMurdo with $\tau_r \sim 5$ –6 hr. These IGWs are located at $x'' = -2,500$ to 200 km and $y'' = -2,000$ to 500 km with $\lambda_H \sim 500$ – 700 km in Figures 13b and 13e. Comparing with Figure 11, we conclude that these IGWs are created from Rossby waves over the circumpolar ocean at $x'' \sim -3,500$ to $-1,500$ km and $y'' \sim -3,500$ to $-2,500$ km. From Figures 14b and 14d, the IGWs with $k/l < 0$ propagate southeastward on 4.0–5.3 July at McMurdo with $\tau_r \sim 5$ –6 hr. These IGWs are located at $x'' = -1,500$ to $1,000$ km and $y'' = -2,000$ to $1,500$ km with $\lambda_H \sim 500$ to 800 km in Figures 13c and 13f. These IGWs are also created from Rossby waves over the circumpolar ocean, although their source region is located at $x'' = -3,000$ to $-2,000$ km and $y'' = 1,000$ to $2,000$ km in Figure 11.

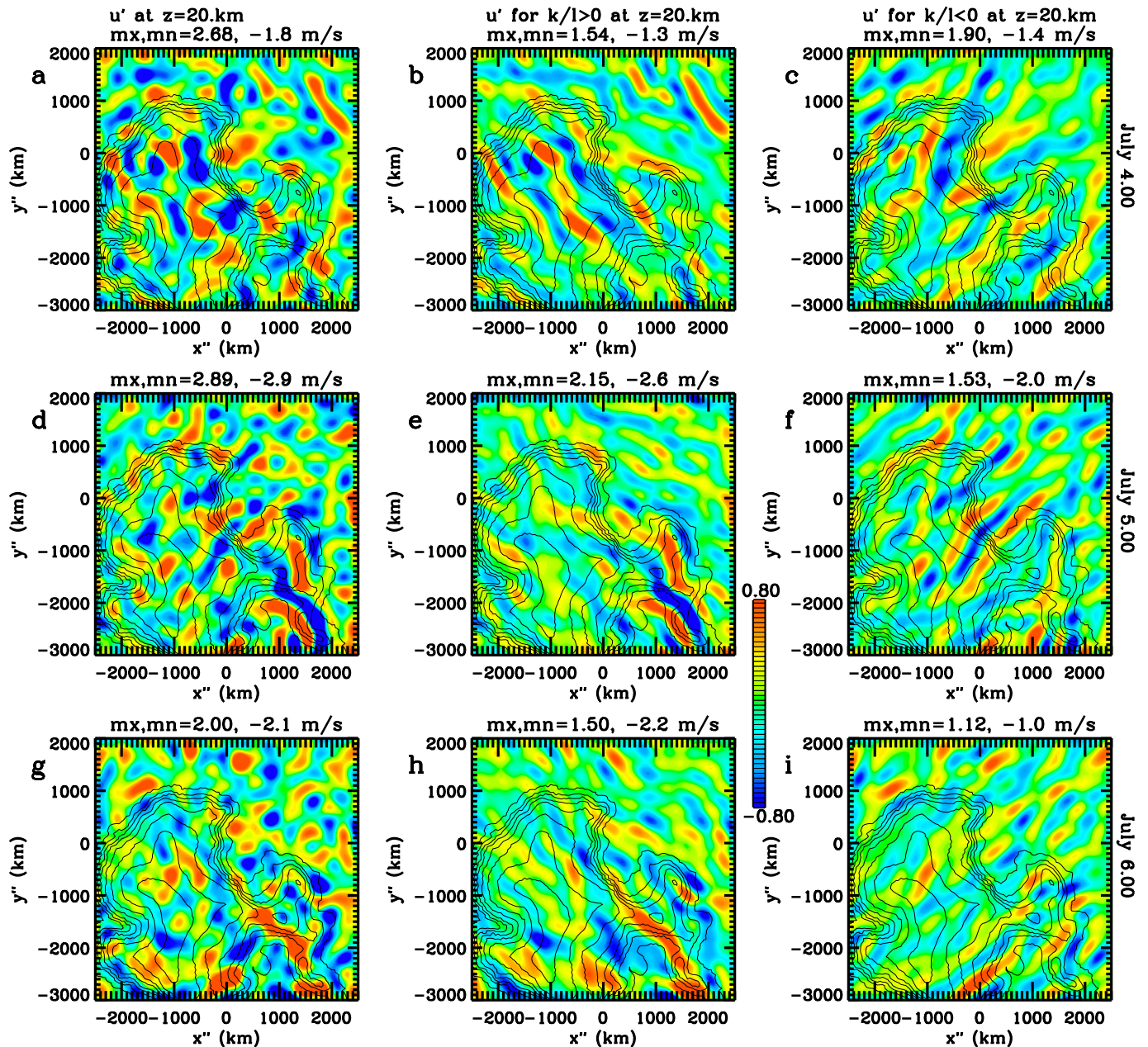


Figure 13. u' at $z = 20$ km on a 2-D plane centered at McMurdo for gravity waves with $\lambda_H = 400$ to $2,000$ km. Row 1: 4.0 July. Left to right panels show u' , u' Fourier filtered so that $k/l > 0$, and u' Fourier filtered so that $k/l < 0$, respectively. Rows 2 and 3: Same as row 1 but for 5.0 and 6.0 July, respectively. Maximum and minimum values of u' are shown at the top of each panel. The height of the topography above sea level is shown as black lines in 0.5-km intervals from 50 m.

Figure 15a shows $u' \sqrt{\bar{\rho}/\bar{\rho}_0}$ at McMurdo for all GWs for $z = 6$ to 36 km on 4–6 July. (As before, these GWs have periods < 11 hr.) Figure 15b shows the result for GWs with $165 < \lambda_H < 400$ km. Strong MW activity is seen, with downward/upward phases in time for $z < 10$ km ($z > 10$ km). Figure 15c shows the result for GWs with $400 < \lambda_H < 2,000$ km. While strong IGW activity is present in the troposphere and lower stratosphere with $\lambda_z \sim 5$ – 10 km, it is small for $z > 25$ km, thereby implying that most of the IGWs dissipate below $z \sim 20$ – 25 km. This can also be seen from v' in Figure 5c. Figure 15d shows the result for GWs with $2,000 < \lambda_H < 5,050$ km. Although these GWs may be generated at $z \sim 13$ km (possibly from Rossby waves), most appear to reflect downward at $z \sim 20$ – 25 km.

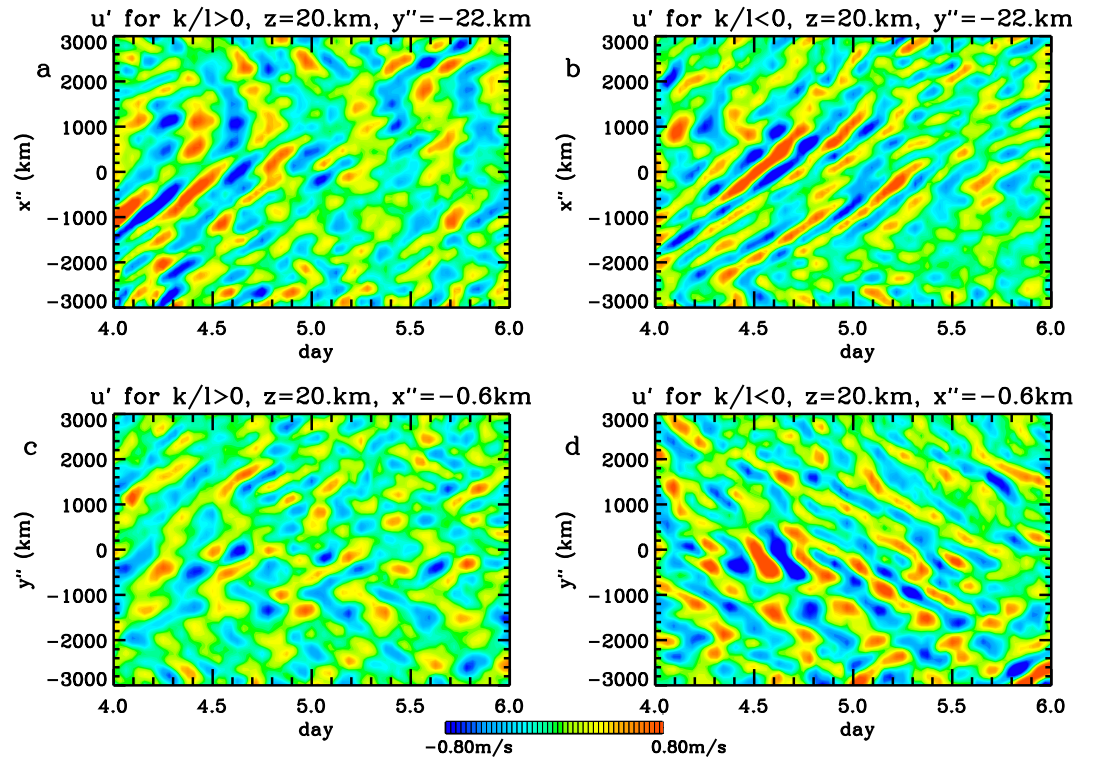


Figure 14. Keograms of u' at $z = 20$ km for gravity waves (GWs) with $\lambda_H = 400$ to $2,000$ km. (a): u' as a function of time and x'' at $y'' = -22$ km for GWs with $k/l > 0$. (b): Same as (a) but for GWs with $k/l < 0$. (c): u' as a function of time and y'' at $x'' = -0.6$ km for GWs with $k/l > 0$. (d): Same as (c) but for GWs with $k/l < 0$. McMurdo is located at $x'' = y'' = 0$.

4.2.4. Dissipation of Mountain Waves in the Stratosphere

As noted previously, during most of July, most of the MWs dissipate at $z \sim 10$ – 20 km (see Figure 3). During strong events, however, MWs can propagate to $z \sim 40$ – 60 km. This occurs on 4.5–6 and 7–11 July, for example (see Figure 5d). In section 4.1 we noted that strong dissipation rates at $z \sim 40$ – 70 km (black contour lines in Figure 7) indicate wave instability and wave-mean-flow interaction during MW events, because both the horizontal and vertical turbulent diffusion coefficients in the KMCM depend on the Richardson number, R_i , giving rise to strong wave damping for $R_i < 0.25$ (Becker, 2009). Here we further illustrate the instability of the MWs at McMurdo in terms of the saturation condition, which is a weaker condition for wave instability than the R_i criterion utilized in the turbulence model of the KMCM.

Figure 16 shows T' on 4–7 July at McMurdo. At $z \sim 50$ – 70 km, the temperature perturbations are large: $T' \sim 5$ – 15 K. The condition for convective instability of a stationary monochromatic MW yields the temperature amplitude (Lindzen, 1981; McFarlane, 1987)

$$T'_{\text{break}} \sim \left(\frac{d\bar{T}}{dz} + \Gamma_a \right) \frac{U}{N_B} \quad (15)$$

where Γ_a is the adiabatic lapse rate ($\Gamma_a = 9.8$ K/km). We overplot T'_{break} in Figure 16. $T' \sim T'_{\text{break}}$ on 4.4–5.1 July at $z \sim 50$ – 70 km, which implies that strong GW damping by turbulent diffusion (corresponding to GW breaking in the real atmosphere) and the accompanying body forces have very likely occurred there. Importantly, we note that $T' \sim T'_{\text{break}}$ occurs slightly before the occurrence of the fishbone structures in Figure 5 at $z \sim 40$ – 70 km on 4.8–5.5 July.

4.3. Secondary GWS at McMurdo in the Stratosphere

4.3.1. Fishbone Structures and Partial Concentric Rings in GW Perturbations

As mentioned previously, fishbone structures are frequently seen at $z \sim 30$ – 60 km on 4.5–11 July in Figure 5. Theory shows that fishbone structures occur in z - t plots when secondary GWs propagate away from the horizontal body force, which generates them, and when the observer is horizontally displaced from

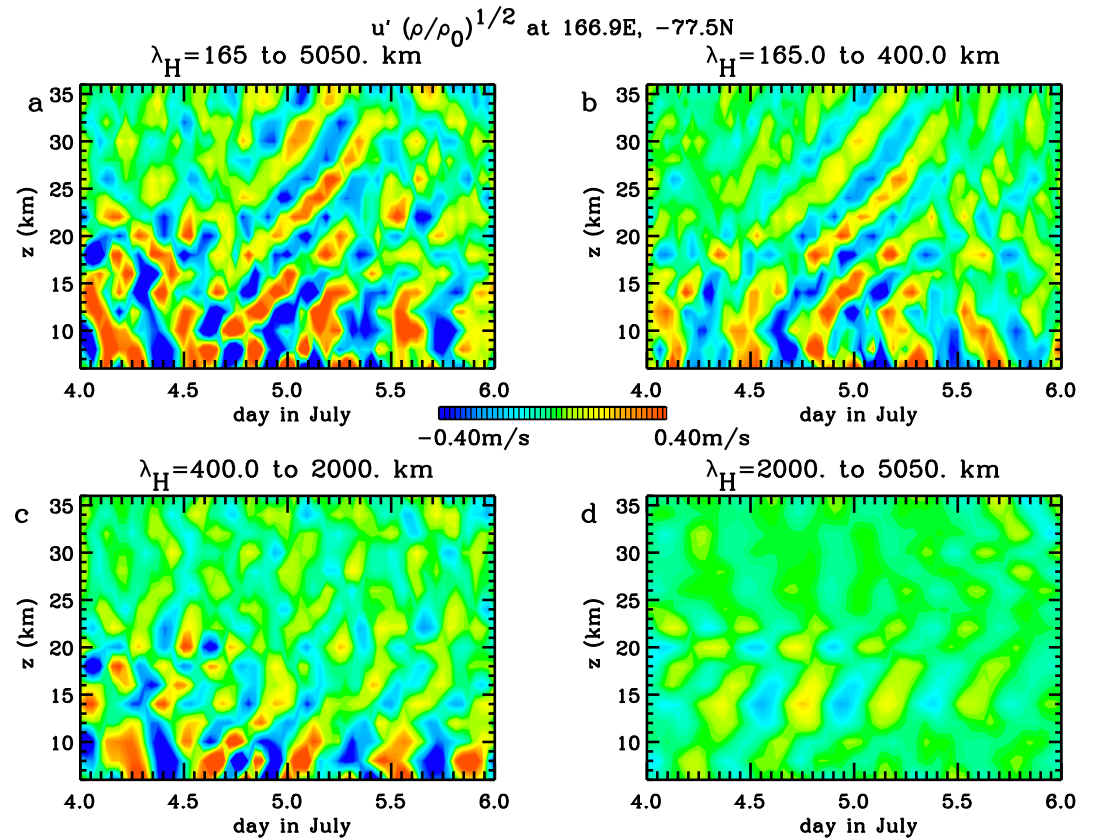


Figure 15. $u' \sqrt{\rho/\rho_0}$ at McMurdo. (a) Gravity waves (GWs) with $165 < \lambda_H < 5,050$ km. (b) GWs with $165 < \lambda_H < 400$ km. (c) GWs with $400 < \lambda_H < 2,000$ km. (d) GWs with $2,000 < \lambda_H < 5,050$ km.

the force (see Figure 6). Because body forces are created from the dissipation of GWs, we now investigate in detail if the fishbone structures seen in Figure 5 are indeed secondary GWs generated from body forces. Figure 17a shows w at $z = 30$ km and u_H at $z = 4$ km on 9.31 July. At this time, strong northeastward downslope winds excite MWs that propagate well into the stratosphere. Another MW event that occurs on 8.09 July is depicted in Figure 17b and will be discussed in section 4.3.4. In the following, we concentrate on the MW event on 9–11 July.

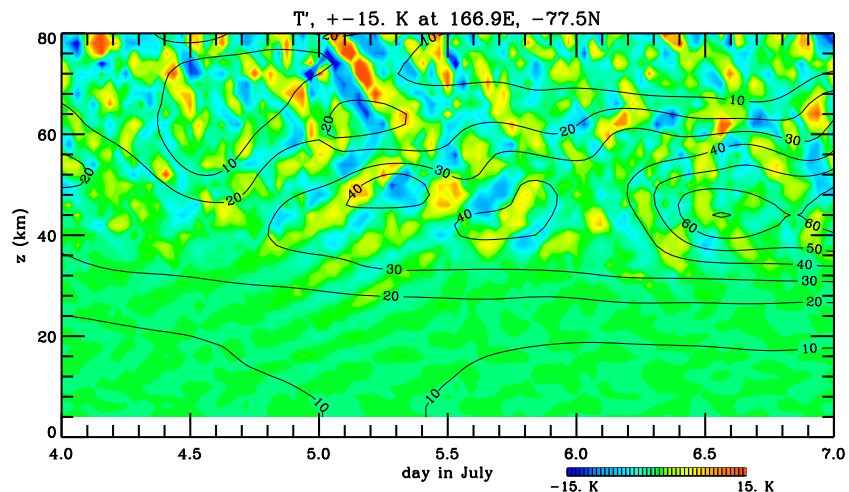


Figure 16. T' at McMurdo (color contours). Black contour lines show T'_{break} from equation (15) in 10-K intervals.

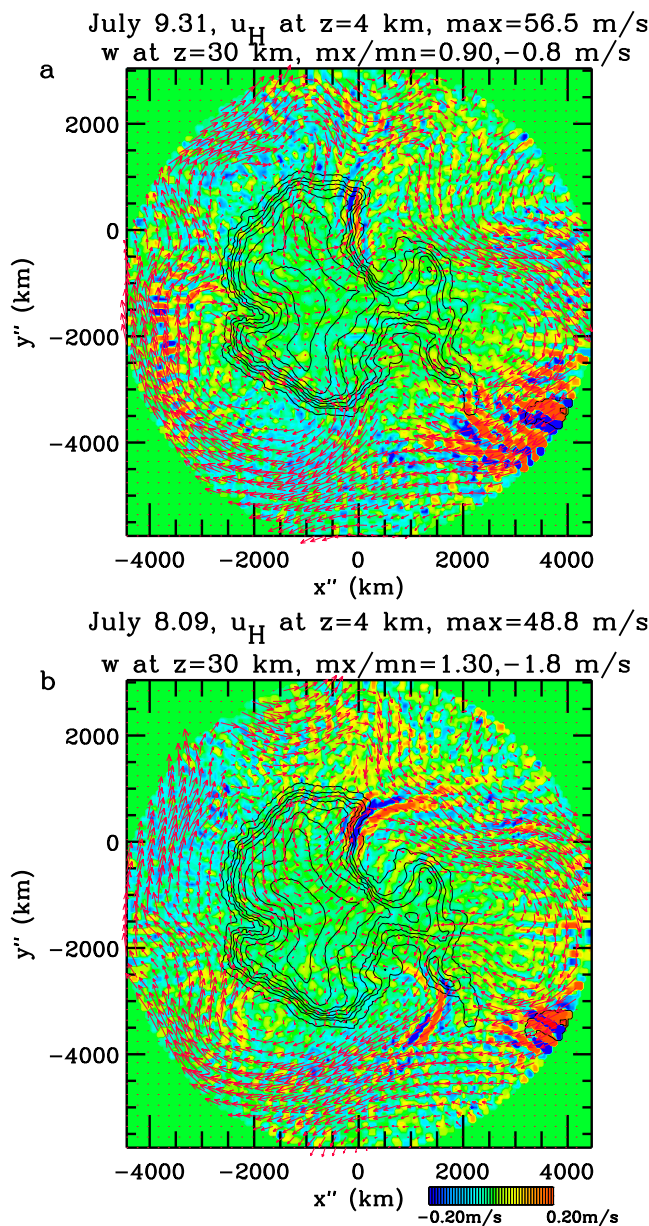


Figure 17. w at $z = 30$ km (color contours) ranging from -0.2 to 0.2 m/s. u_H is shown at $z = 4$ km as red arrows, with lengths proportional to the maximum horizontal wind. McMurdo is located at $x'' = y'' = 0$. (a) 9.31 July. (b) 8.09 July. Maximum and minimum values of w and u_H are shown at the top of each panel.

knee. From Figures 20a and 20c, the GWs above and below the knee propagate eastward on 9.0–11.0 July at McMurdo, with similar values of $\tau_r \sim 9$ –10 hr and $c_x = 90$ –100 m/s. From Figures 20b and 20d, GWs above and below the knee propagate northward on 9.0–10.2 July and southward on 9.5–11.0 July at McMurdo. For the southward GWs on 9.5–11.0 July, the GWs below and above the knee have similar values of $\tau_r \sim 9$ –10 hr and $c_y = -50$ to -70 m/s. The overlap of northward and southward-propagating GWs at McMurdo can be seen on 10.0 July at $z = 42$ and 50 km in Figures 19g and 19i; here the northeastward-propagating GWs are located at $x'' \sim -2,000$ to $2,000$ km and $y'' \sim -1,000$ to $2,000$ km, while the southeastward-propagating GWs are located at $x'' \sim -1,000$ to $2,500$ km and $y'' \sim -2,500$ to $1,000$ km. Thus, there are two separate GW packets propagating in different directions at this time over McMurdo. After 10.2 July, only southeastward-propagating GWs are seen over McMurdo (see Figures 19j and 19l).

Figure 18a shows a close-up of $u' \sqrt{\bar{\rho}/\bar{\rho}_0}$ at $z = 30$ – 60 km. The fishbone structure occurs from 9.5 to 10.75 July, with an average knee altitude of $z \sim 46$ km. The GWs below and above the knee have $\lambda_z \sim 18$ – 25 km; these values are nearly twice as large as those for the MWs at $z \sim 30$ – 50 km of $\lambda_z \sim 12$ km (see Figure 7). Figure 18b shows the same GWs from Figure 18a but having $165 < \lambda_H < 700$ km. Although MWs and small-scale GWs are present, they do not contribute significantly to the fishbone structure. Figures 18c and 18d show GWs with $700 < \lambda_H < 3,000$ km and $3,000 < \lambda_H < 5,050$ km, respectively. Most of the fishbone structure is created from GWs with $700 < \lambda_H < 3,000$ km.

Figures 19a–19c show horizontal cross sections of $u' \sqrt{\bar{\rho}/\bar{\rho}_{z=50}}$ for GWs with $700 < \lambda_H < 3,000$ km on 9.5 July at $z = 42, 46$, and 50 km, respectively. Here $\bar{\rho}_{z=50}$ denotes $\bar{\rho}$ evaluated at $z = 50$ km. Rows 2–4 show the same quantities but on 9.75, 10.0, and 10.25 July, respectively. Dozens of partial concentric ring structures are visible in Figure 19; black arrows highlight a few of the most prominent structures. Perhaps the clearest ring structure is located at $x'' = -1,000$ to $1,000$ km and $y'' = 0$ to $2,500$ km on 10.25 July at $z = 46$ km, with a yellow (blue) inner (outer) ring. The center of these rings are located at $x'' \sim -100$ to -200 km and $y'' \sim 1,200$ km. These partial ring structures are an important clue for the presence of secondary GWs from body forces, since secondary GWs excited by body forces have partial concentric ring structures in a uniform background wind (Vadas & Liu, 2009, 2013; Vadas et al., 2003, 2018), as shown earlier (see Figure 6b). (To our knowledge, only body forces and heat/coolings can excite GWs with concentric ring structure in the middle atmosphere.) Furthermore, the last row in Figure 19 indicates that in the region from $x'' = -1,000$ to $2,000$ km and $y'' = -1,000$ to $1,000$ km, the GW phases are aligned from southwest to northeast and have similar horizontal wavelengths below (panel j) and above (panel l) the knee of the fishbone structure in Figures 18a and 18c, which is located at $z_{\text{knee}} \sim 46$ km and after 10 July. This is another indication that these GWs are secondary GWs generated by a body force at ~ 46 km. Note that the partial concentric ring structures are only noticeable near the center of the structures; this is likely due to wind filtering (see below). Indeed, it is likely that because of wind filtering, only a few GWs with curved wavefronts not arising from deep convection have been observed in the MLT (Vargas et al., 2016).

To obtain quantitative estimates of the horizontal phase speeds and propagation directions of the secondary GWs, Figure 20 shows keograms of $u' \sqrt{\bar{\rho}/\bar{\rho}_{z=50}}$ for the GWs with $700 < \lambda_H < 3,000$ km. Figures 20a and 20b are ~ 4 km below the knee, while Figures 20c and 20d are ~ 4 km above the

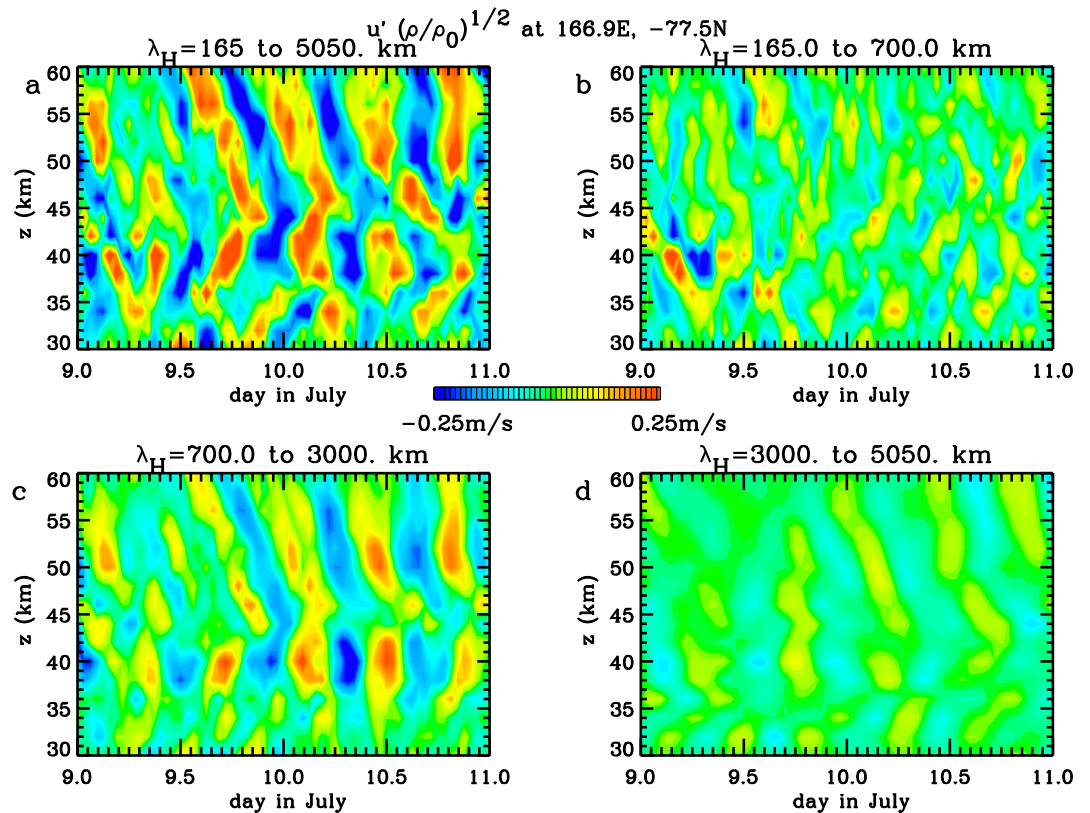


Figure 18. $u' \sqrt{\rho/\rho_0}$ at McMurdo. (a) Gravity waves (GWs) with $165 < \lambda_H < 5,050$ km. (b) GWs with $165 < \lambda_H < 700$ km. (c) GWs with $700 < \lambda_H < 3,000$ km. (d) GWs with $3,000 < \lambda_H < 5,050$ km.

We now determine c_H and λ_H for the southeastward GWs on 10.0–10.75 July. Below the knee, we use $c_x = 100$ m/s, $c_y = -70$ m/s, $\tau_r = 10$ hr, and equation (13) to obtain $c_H = 57$ m/s and $\lambda_H = c_H \tau_r \sim 2,050$ km. Additionally, the azimuth of propagation is

$$\Upsilon = \tan^{-1} \left(\frac{k}{l} \right) = \tan^{-1} \left(\frac{c_y}{c_x} \right), \quad (16)$$

which yields $\Upsilon = 145^\circ$ east of north or southeastward. Above the knee, we use $c_x = 90$ m/s, $c_y = -50$ m/s, and $\tau_r = 10$ hr to obtain $c_H = 44$ m/s, $\lambda_H \sim 1,600$ km and $\Upsilon = 151^\circ$. The striking similarity in λ_z , τ_r , λ_H , c_H , and Υ below and above the knee, and the fact that λ_H is much larger than that of the MWs, strongly indicates that the GWs in the fishbone structure in Figure 18 are secondary GWs created by a single body force (Vadas et al., 2018).

The reason that no westward-propagating GWs are seen in Figures 20a and 20c is because the structure of the background wind favors eastward-propagating GWs. The secondary GWs are excited near the peak of the polar night jet, where the eastward wind is large. In this frame of reference, the eastward and westward GWs are created with equal intrinsic phase speeds for each $|k|$, $|m|$, and ω_r (Vadas et al., 2003). However, the eastward secondary GWs have much larger ground-based phase speeds than the westward secondary GWs. Below and above the excitation altitude, the eastward background wind decreases significantly. Relative to the wind at the excitation altitude, this is akin to the secondary GWs propagating through an increasing “westward wind.” This causes the westward (eastward) propagating secondary GWs to have decreasing (increasing) $|\lambda_z|$ and leads to the westward secondary GWs breaking and/or reaching critical levels and dissipating closer to the body force than the eastward secondary GWs. For the upward-propagating secondary GWs, this leads to the westward secondary GWs dissipating at lower altitudes than the eastward secondary GWs, as was seen in Becker and Vadas (2018).

4.3.2. Secondary GWS Excited by a Body Force From MW Dissipation

We now estimate the location of a body force that could have excited the southeastward secondary GWs in the fishbone structure after about 9.5 July (see Figure 18). As is well known, GWs propagate horizontally

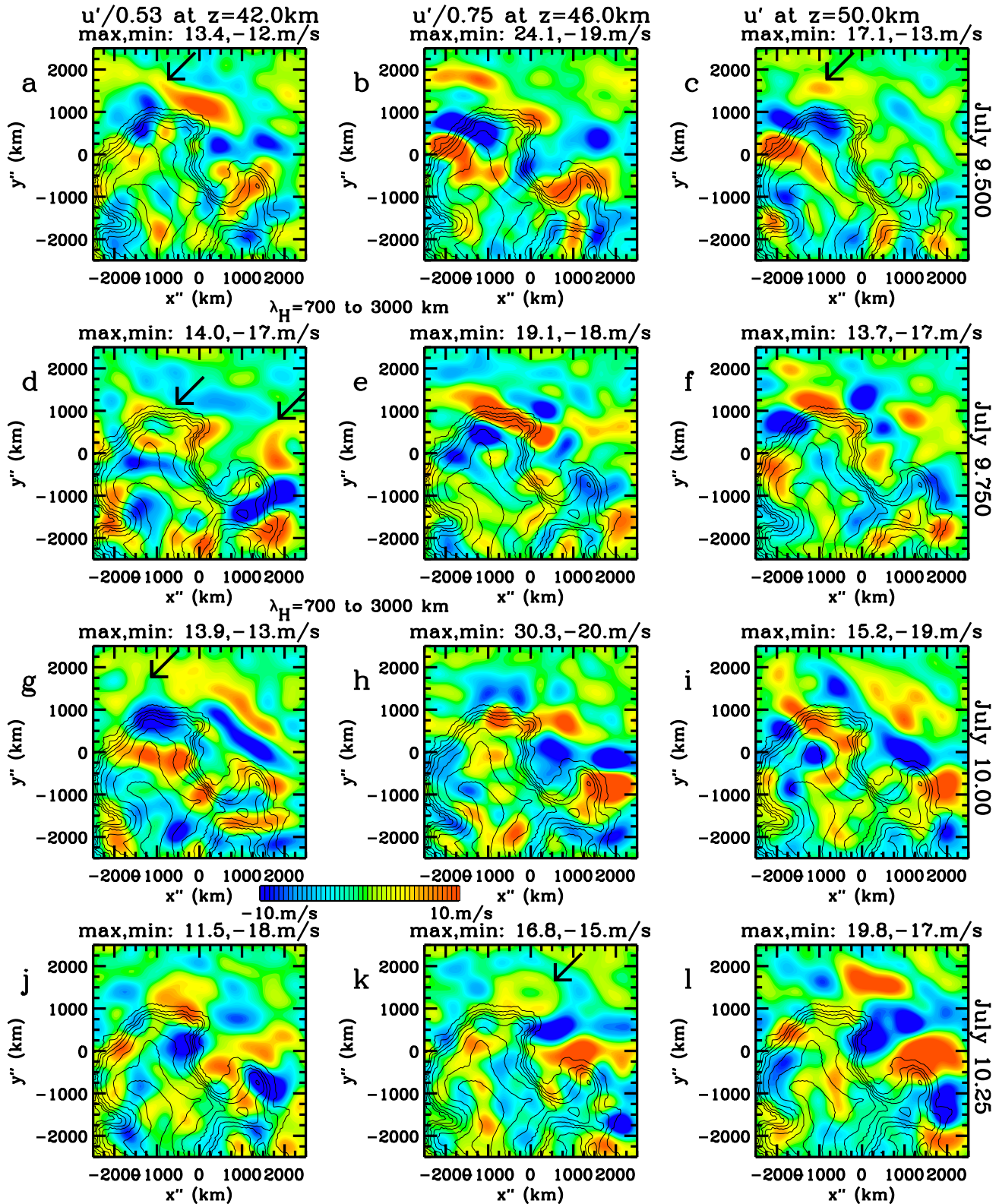


Figure 19. Gravity waves with $700 < \lambda_H < 3,000$ km. McMurdo is located at $x'' = y'' = 0$. Row 1: 9.5 July. The left panel shows $u'/(0.53)$ at $z = 42$ km, the middle panel shows $u'/(0.75)$ at $z = 46$ km, and the right panel shows u' at $z = 50$ km. Here $\sqrt{\bar{p}_{z=50}/\bar{p}_{z=42}} = 0.53$ and $\sqrt{\bar{p}_{z=50}/\bar{p}_{z=46}} = 0.75$. Rows 2–4: Same as in row 1 but on 9.75, 10.0, and 10.25 July, respectively. Arrows show locations and times for important gravity wave features (see text). Maximum and minimum values are shown at the top of each panel.

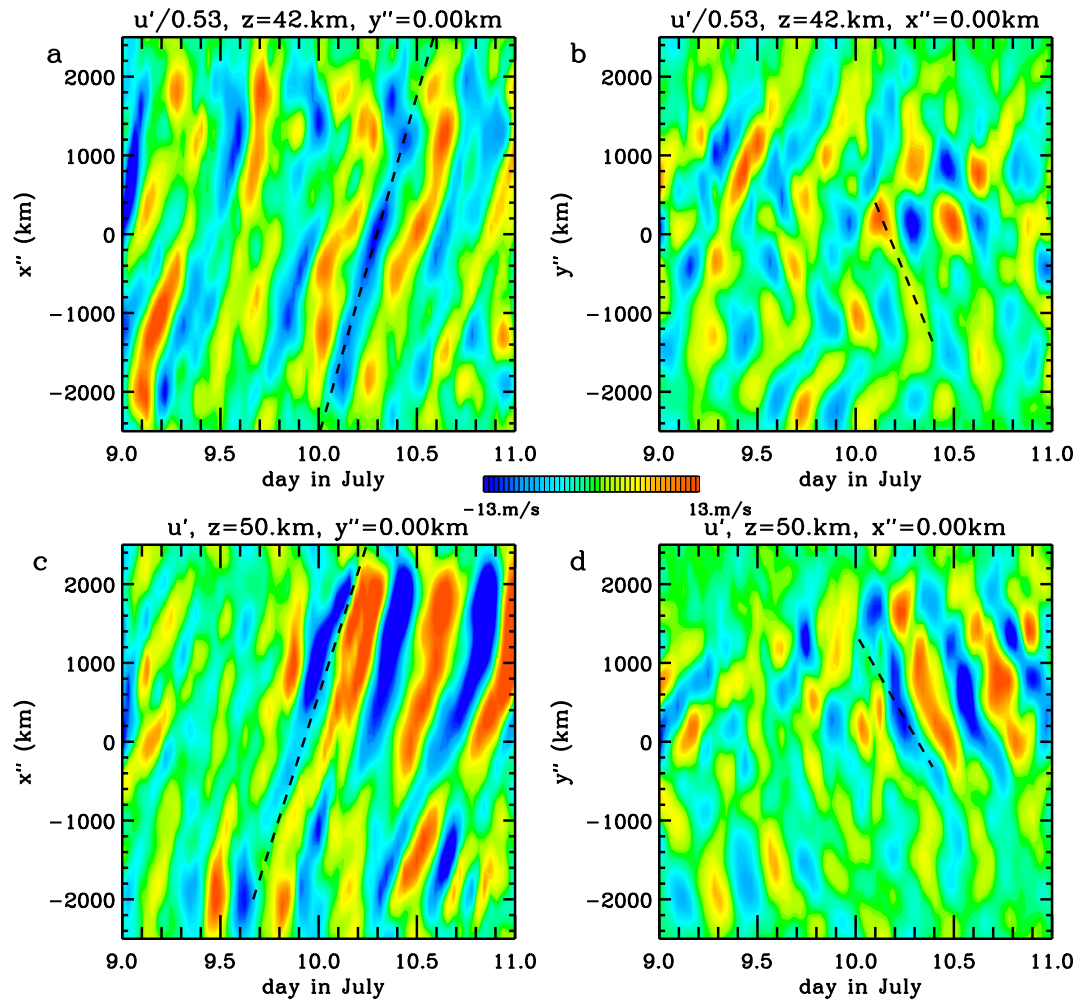


Figure 20. Keograms for gravity waves with $700 < \lambda_H < 3,000$ km. (a): $u'/(0.53)$ at $z = 42$ km and $y'' = 0$, where $\sqrt{\bar{\rho}_{z=50}/\bar{\rho}_{z=42}} = 0.53$. The dashed line shows $c_x = 100$ m/s. (b): $u'/(0.53)$ at $z = 42$ km and $x'' = 0$. The dashed line shows $c_y = -70$ m/s. (c) u' at $z = 50$ km and $y'' = 0$. The dashed line shows $c_x = 90$ m/s. (d) u' at $z = 50$ km and $x'' = 0$. The dashed line shows $c_y = -50$ m/s.

and vertically at the same time (Hines, 1960). If the background wind (U, V) is approximately constant along the raypath, then a GW propagates at an angle η from the horizontal of (Vadas et al., 2009):

$$\sin(\eta) \simeq \tau_B / \tau_{Ir}, \quad (17)$$

where $\tau_{Ir} = 2\pi / \omega_{Ir} = 2\pi / (\omega_r - kU - lV)$ is the intrinsic period and $\tau_B = 2\pi / N_B$ is the buoyancy period. Inserting the midfrequency GW dispersion relation (given by equation (2)) into equation (17), we obtain

$$\eta \simeq \sin^{-1}(|\lambda_z| / \lambda_H). \quad (18)$$

From Figure 18c, the secondary GWs above the knee at 9.75 July have $|\lambda_z| \sim 18$ km. Using $\lambda_H \sim 1,600$ km, we estimate $\eta \sim 0.6^\circ$. Because the vertical distance traveled from $z = 46$ km to $z = 50$ km is $\Delta z \sim 4$ km, we estimate that the secondary GWs at $z = 50$ km over McMurdo would have propagated the horizontal distance $\Delta L \sim \Delta z / \tan \eta \sim 400$ km away from the center of the body force and that the body force would have occurred $400 \text{ km} / c_H \sim 2.5$ hr (or 0.1 day) earlier. Here we have used $c_H = 44$ m/s.

Figure 21 shows w at $z = 16, 30,$ and 42 km on 9.5, 9.75, 10.0, and 10.25 July, and Figure 22 shows w at $z = 46, 60,$ and 76 km at the same times. On 9.5–9.75 July, relatively stationary MWs are seen at $z \sim 16$ – 60 km. (Note that it is because these MWs have relatively stationary phases in time that filtering GWs with $\tau_r \geq 11$ hr removed most of their signal on 9.5–10.25 July in Figures 5a, 5b, and 5c.) At later times, little MW activity is seen at $z > 40$ km. On 9.5 July in particular, MWs are strong 100–1,000 km northwest of McMurdo from

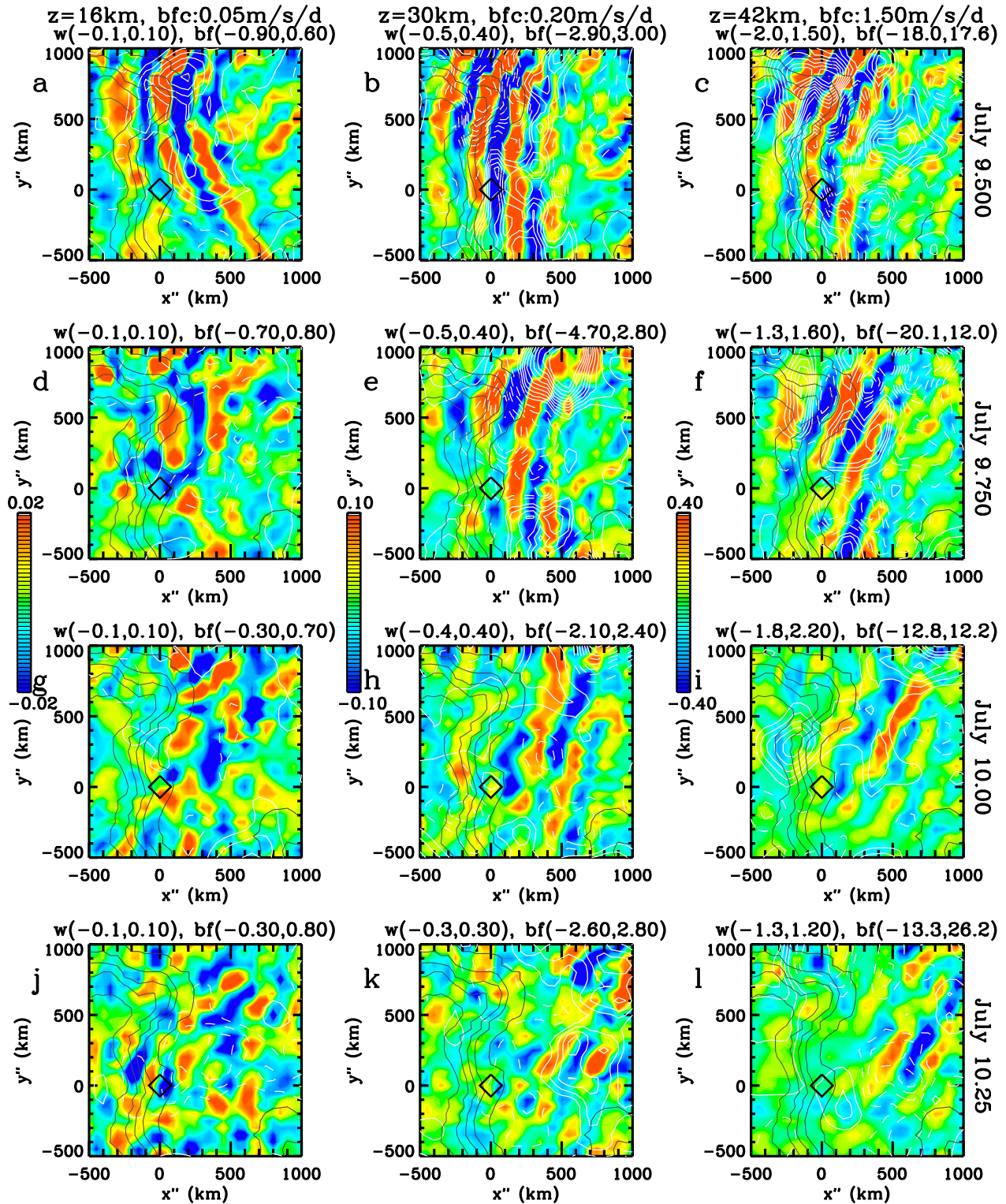


Figure 21. (a) w at $z = 16$ km on 9.5 July (color contours from -0.02 to 0.02 m/s). White solid (dashed) lines indicate positive (negative) zonal body force in $0.05\text{-m}\cdot\text{s}^{-1}\cdot\text{day}^{-1}$ intervals. The black diamond shows McMurdo. (b) Same as in (a) but at $z = 30$ km; w ranges from -0.1 to 0.1 m/s, and the body force intervals are $0.2\text{-m}\cdot\text{s}^{-1}\cdot\text{day}^{-1}$. (c) Same as in (a) but at $z = 42$ km; w ranges from -0.4 to 0.4 m/s, and the body force intervals are $1.5\text{-m}\cdot\text{s}^{-1}\cdot\text{day}^{-1}$. Row 2: Same as in row 1 but on 9.75 July. Row 3: Same as in row 1 but on 10.0 July. Row 4: Same as in row 1 but on 10.25 July. Maximum and minimum values of w (in $\text{m}\cdot\text{s}^{-1}$) and the body force (in $\text{m}\cdot\text{s}^{-1}\cdot\text{day}^{-1}$) are shown at the top of each panel.

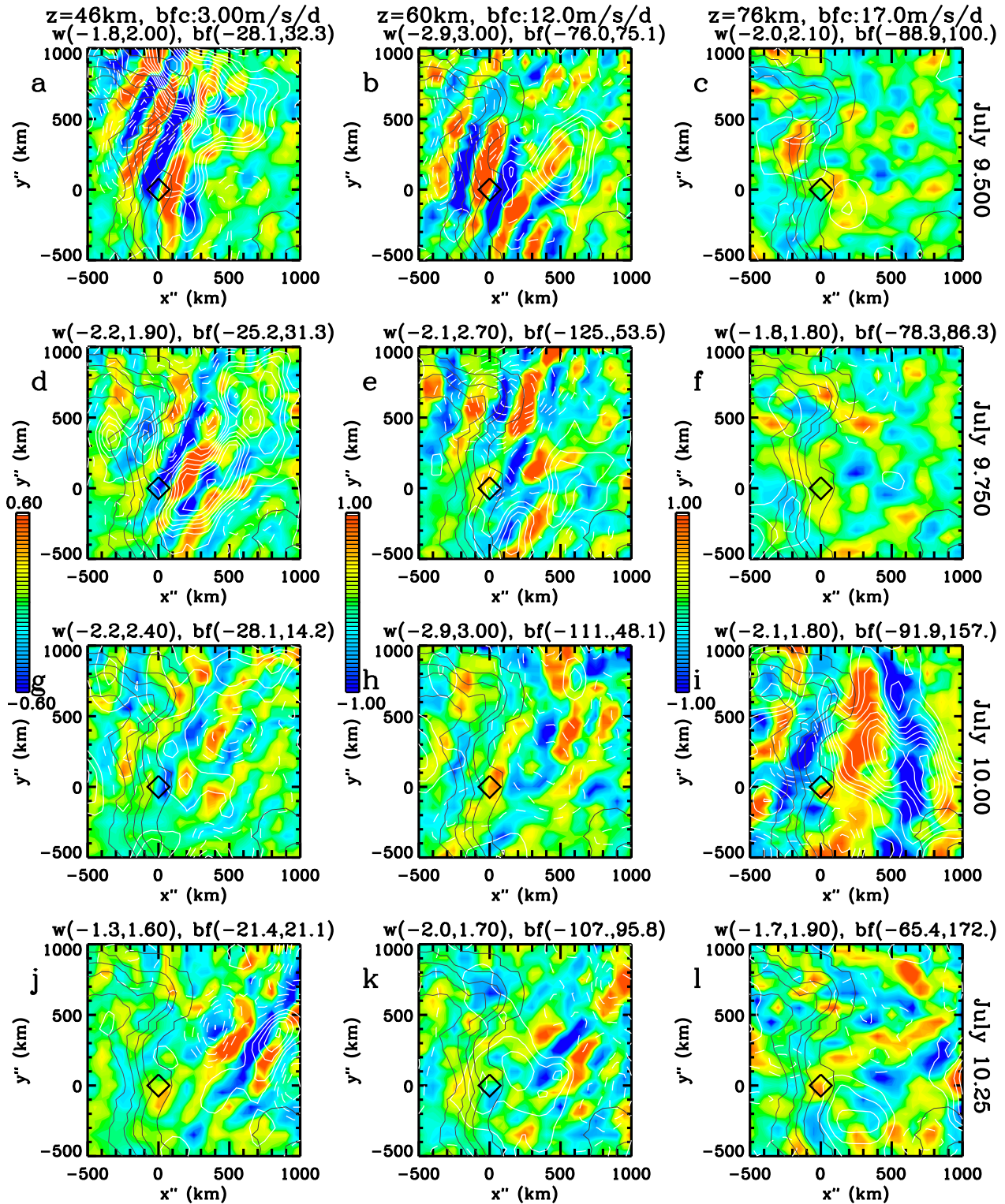


Figure 22. (a) w at $z = 46$ km on 9.5 July (color contours from -0.6 to 0.6 m/s). White solid (dashed) lines show positive (negative) values of the body force in $3.0 \cdot m \cdot s^{-1} \cdot day^{-1}$ intervals. The black diamond shows McMurdo. (b) Same as in (a) but at $z = 60$ km; w ranges from -1.0 to 1.0 m/s, and the body force intervals are $12 \cdot m \cdot s^{-1} \cdot day^{-1}$. (c) Same as in (a) but at $z = 76$ km; w ranges from -1.0 to 1.0 m/s, and the body force intervals are $17 \cdot m \cdot s^{-1} \cdot day^{-1}$. Row 2: Same as in row 1 but on 9.75 July. Row 3: Same as in row 1 but on 10.0 July. Row 4: Same as in row 1 but on 10.25 July. Maximum and minimum values of w (in m/s) and the body force (in $m \cdot s^{-1} \cdot day^{-1}$) are shown at the top of each panel.

$z = 16$ to $z = 42$ km. At $z = 46$ km, the MWs are weaker at $y'' > 500$ km. At $z = 60$ km, there are no MWs 400–1,000 km northwest of McMurdo (Figure 22b), although there are still MWs closer to McMurdo. At $z = 76$ km, no MWs are seen (Figure 22c). This implies that the MWs 400–1,000 km northwest of McMurdo dissipated at $42 < z < 60$ km on 9.5 July.

To determine the body force resulting from the dissipation of these MWs, we calculate the pseudo momentum flux convergence (see equation (1)). Since the MWs propagate mainly zonally, it is sufficient to compute the zonal component, F_x . We define the mean components (\bar{p} , U , V , W , \bar{T}) at each grid point by applying a $750 \text{ km} \times 750 \text{ km}$ horizontal average that is centered at each grid point. The scale of this horizontal average corresponds to $\sim 3\lambda_H$ for the MWs. The MW-related wind perturbations are then defined as $u' = u - U$, $v' = v - V$, $w' = w - W$, and $T' = T - \bar{T}$, and the zonal pseudo momentum flux, $(u'w' - f \frac{c_p}{g} T'v')$, is computed by applying a centered horizontal average of $450 \text{ km} \times 450 \text{ km}$ to $(u'w' - f \frac{c_p}{g} T'v')$ at each grid point. The vertical derivative is computed using a centered finite differencing in z . The resulting zonal body force is shown in Figures 21 and 22 with white contour lines (note the different contour intervals for the different panels). Overall, there is huge variety in amplitude and location of the body forces, which at $z = 60$ and 76 km also include the effects of dissipating secondary GWs (Becker & Vadas, 2018).

We now focus on 9.50 July at $z = 46$ km (Figure 22a). There is a significant westward body force of $\sim 28 \text{ m}\cdot\text{s}^{-1}\cdot\text{day}^{-1}$ located ~ 400 km northwest of McMurdo at $(x'', y'') = (-150, 400)$ km. This force is created by the dissipation of the (westward) MWs. There is also an eastward body force of $\sim 32 \text{ m}\cdot\text{s}^{-1}\cdot\text{day}^{-1}$ located ~ 700 km northeast of McMurdo. This change in sign of the body force can be explained by the transient change in c_x (see equation (12)) caused by the acceleration/deceleration of the mean wind due to synoptic-scale tropospheric Rossby waves as discussed earlier in this paper. Note, however, that the mean body force in the stratosphere over McMurdo for the present model simulation is westward, as expected (see Figures 5 and 8 in Becker & Vadas, 2018).

According to theory (Vadas et al., 2003, 2018), a westward body force excites eastward- and westward-propagating secondary GWs, which radiate away from the body force like dual “headlights”; other than purely northward or southward, secondary GWs are excited in all directions (see Figure 6b). Thus, the southeastward GWs in the fishbone structure in Figures 18–20 could have been created by the westward body force northwest of McMurdo on 9.5 July (Figure 22a). In conclusion, the altitude, location, and time of this body force agree well with our previous estimate that the secondary GW source occurred 0.1 days earlier at $z \sim 46$ km and $\Delta L \sim 400$ km northwest of McMurdo.

4.3.3. Comparison of Secondary GW Scales With Body Force Scales

We now investigate if the secondary GW horizontal and vertical wavelengths and periods as determined from the horizontal velocity perturbations agree with the spatial and temporal extents of this body force. The horizontal extent of the body force is $L_H \sim 800$ km from Figure 22a. This agrees well with the horizontal wavelength of the secondary GWs, $\lambda_H \sim 1,600$ – $2,050$ km, because even though the secondary GW spectrum is broad, it peaks at $\lambda_H \sim 2L_H$ in the horizontal velocity spectrum for a force duration of $\chi < 6$ hr (Vadas et al., 2018). The vertical extent of the body force is coarsely estimated from Figures 21 and 22 to be $L_z \sim 8$ km, since half of the force extends from $z \sim 42$ to 46 km. This agrees with the vertical wavelength of the secondary GWs, $\lambda_z \sim 18$ – 25 km, because although the secondary GW spectrum is broad, it peaks at $\lambda_z \sim 2.5L_z$ in the horizontal velocity spectrum for a force duration of $\chi < 6$ hr (Vadas et al., 2018).

We now determine the so-called *characteristic period* of the body force, τ_c , by assuming that the dominant GW excited by this force (if impulsive) would have wavelengths that are twice the widths and depth of the force: $|\lambda_x| \sim 2L_x$, $|\lambda_y| = 2L_y$, and $|\lambda_z| \simeq 2L_z$, where L_x and L_y are the full zonal and meridional extents of the force, respectively. Thus, τ_c is the period of this assumed dominant GW. We substitute $L_x = 4.5\sigma_x$, $L_y = 4.5\sigma_y$, and $L_z = 4.5\sigma_z$ into equation (3.3) of Vadas et al. (2003). The characteristic period of the body force is then

$$\tau_c = 2\pi \left[\frac{L_x^{-2} + L_y^{-2} + L_z^{-2}}{(L_x^{-2} + L_y^{-2}) N_B^2 + L_z^{-2} f^2} \right]^{1/2} = 2\pi \left[\frac{2L_H^{-2} + L_z^{-2}}{2L_H^{-2} N_B^2 + L_z^{-2} f^2} \right]^{1/2}, \quad (19)$$

where the second expression holds if $L_H = L_x = L_y$. As before, $f = 2\Omega \sin \theta$, θ is latitude and $\Omega = 2\pi/24$ hr is Earth’s rotation rate. Using $\theta = -80^\circ$, we obtain $f = -0.00014$ rad/s, which corresponds to an inertial period of $|2\pi/f| = 12.5$ hr. Assuming $N_B = 0.02$ rad/s and using $L_H = 800$ km and $L_z = 8$ km, we obtain $\tau_c = 5.5$ hr.

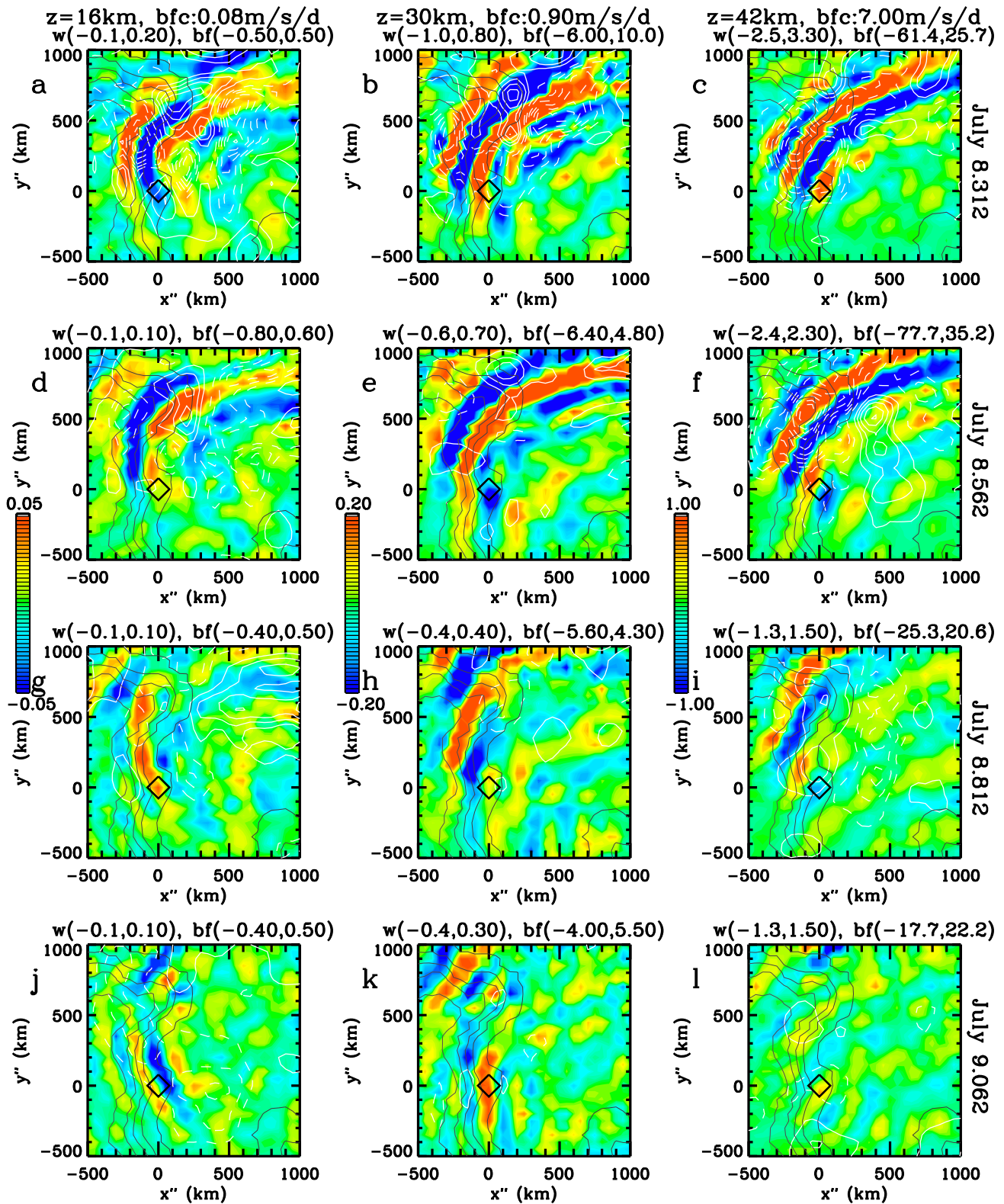


Figure 23. Same as in Figure 21 but for 8.312 July (row 1), 8.562 July (row 2), 8.812 July (row 3), and 9.062 July (row 4). Color contour ranges for w are -0.05 to 0.05 m/s, -0.2 to 0.2 m/s, and -1 to 1 m/s at $z = 16, 30,$ and 42 km, respectively. The body force intervals are $0.08, 0.9,$ and $7 \text{ m}\cdot\text{s}^{-1}\cdot\text{day}^{-1}$ at $z = 16, 30,$ and 42 km, respectively.

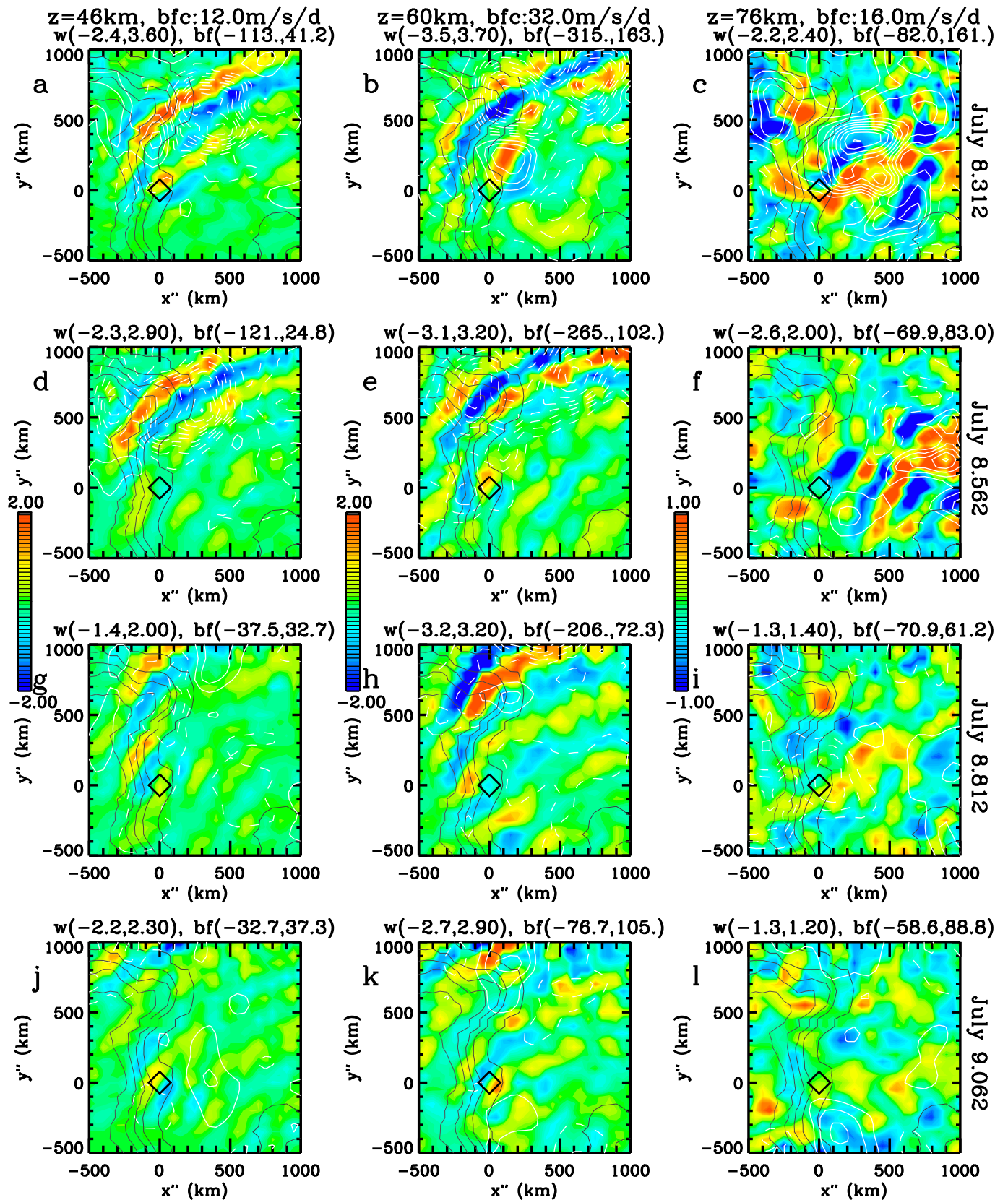


Figure 24. Same as in Figure 22 but for July 8.312 (row 1), 8.562 July (row 2), 8.812 July (row 3), and 9.062 July (row 4). Color contour ranges for w are -2 to 2 m/s, -2 to 2 m/s, and -1 to 1 m/s at $z = 46, 60,$ and 76 km, respectively. The body force intervals are $12, 32,$ and 16 $m \cdot s^{-1} \cdot day^{-1}$ at $z = 46, 60,$ and 76 km, respectively.

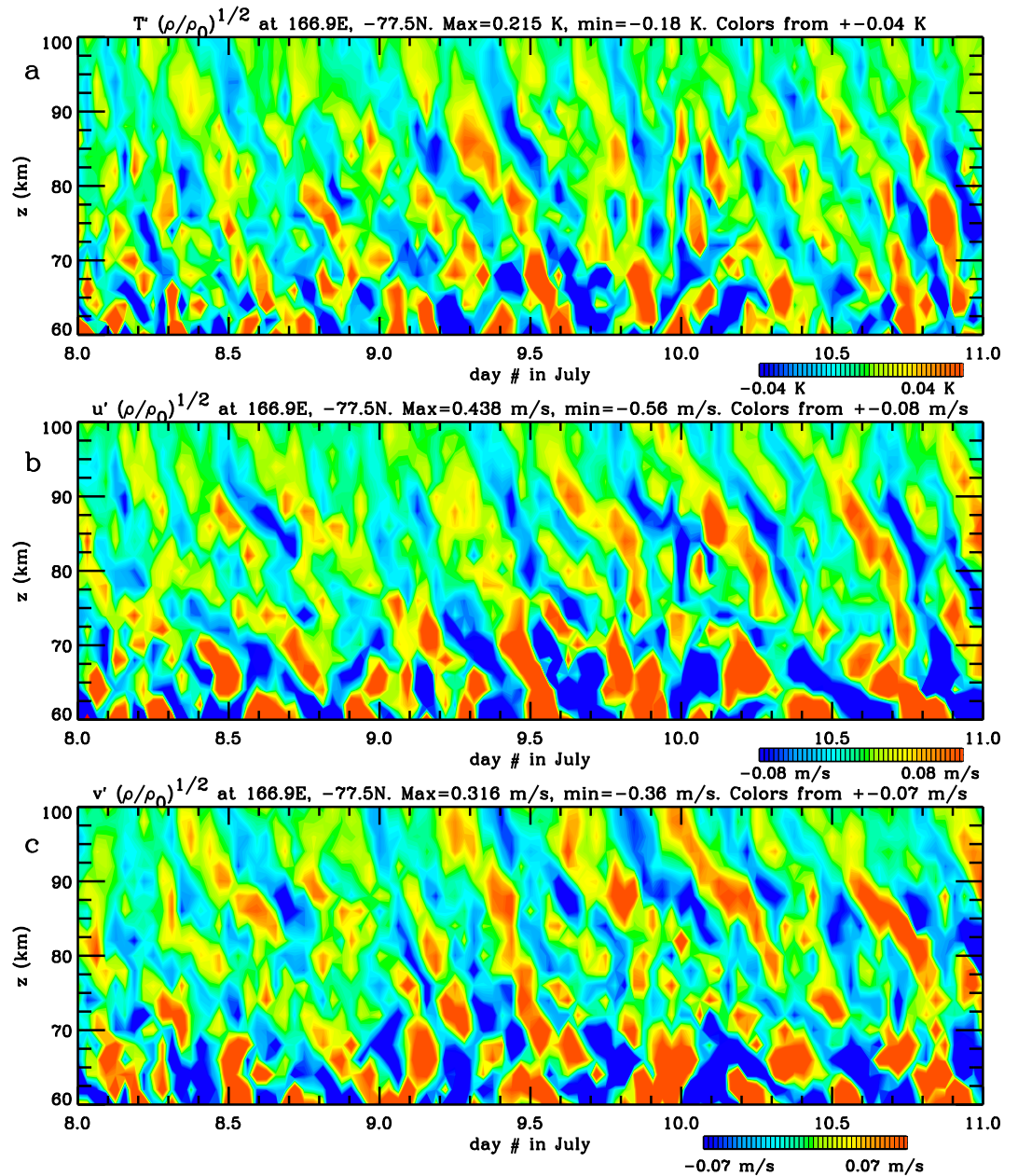


Figure 25. Same as Figure 3 but for 8–11 July at $z = 60\text{--}100$ km.

If $\chi < \tau_c$, the secondary GW spectrum peaks at $\tau_r \sim \tau_c$; whereas if $\chi > \tau_c$, the secondary GW spectrum peaks at $\tau_r \sim \chi$, since the higher-frequency GWs are cutoff (Vadas et al., 2003). We estimate χ very roughly to be $\chi < 12$ hr from Figures 22a and 22d (since the westward force is gone in Figure 22d).

We now estimate the intrinsic period, τ_r , of the southeastward-propagating secondary GWs. These GWs are created in the reference frame of the background wind at the excitation altitude with intrinsic horizontal phase speeds of $c_{iH} = \omega_r/k_H = \lambda_H/\tau_r = c_H - U_H$. At $z \sim 46$ km, $U \sim 30$ m/s and $V \sim 0$ on 9.5 July from Figure 1. Therefore, the background wind in the southeastward direction is $U_H \sim 15$ m/s. Since $c_H \sim 50$ m/s, $c_{iH} \sim 35$ m/s, which corresponds to $\tau_r = \lambda_H/c_{iH} \sim 14$ hr. Since $\tau_r \leq 2\pi/f$, we estimate $\tau_r \sim 12.5$ hr. This agrees with the rough estimate from the previous paragraph.

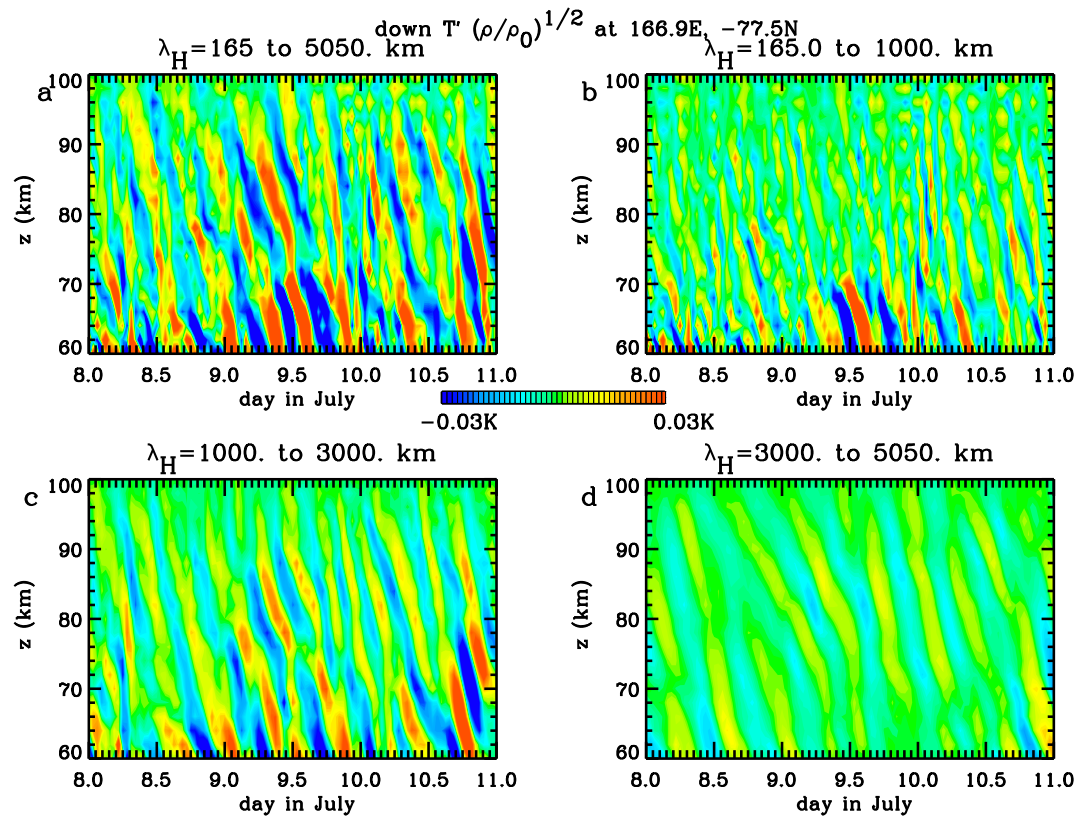


Figure 26. $T' \sqrt{\bar{\rho}/\bar{\rho}_0}$ at McMurdo for gravity waves (GWs) with downward phases in time. (a) GWs with $165 < \lambda_H < 5,050$ km. (b) GWs with $165 < \lambda_H < 1,000$ km. (c) GWs with $1,000 < \lambda_H < 3,000$ km. (d) GWs with $3,000 < \lambda_H < 5,050$ km.

In conclusion, we have shown that the southeastward-propagating secondary GWs in the fishbone structure on 9.5–10 July at $z \sim 30$ –60 km were likely generated by the body force ~ 400 km northwest of McMurdo at $z \sim 46$ km, 2.5 hr earlier. We also showed that this body force was created by MW dissipation.

4.3.4. Prevalence of Fishbone Structures and Body Forces in the Stratosphere

Fishbone structures occur from $z \sim 30$ –60 km at many times and altitudes in Figures 5 and 7. This suggests that secondary GWs and body forces are prevalent in the stratosphere. For example, for the MW event on 7.0–8.5 July, secondary GWs can be seen starting on 7.0 July at lower altitudes in Figure 7 and increasing by ~ 10 km in altitude by 8.0 July. Figure 17b shows w at $z = 30$ km and u_H at $z = 4$ km on 8.09 July. At this time, there are northeastward (downslope) winds west of McMurdo, which excite MWs that propagate to $z = 30$ km. Figure 23 shows w at $z = 16, 30,$ and 42 km on 8.312, 8.562, 8.812, and 9.062 July, and Figure 24 shows w at the same times at $z = 46, 60,$ and 76 km. As before, MWs are seen northwest to northeast of McMurdo for $z = 16$ to 60 km, although their amplitudes decrease rapidly above 42 km. These MWs are strong on 8.312 and 8.562 July and decrease rapidly after this time. The body forces on 8.312 and 8.562 July are mainly westward at $z = 16$ to 60 km. These body forces occur often around McMurdo at $z \sim 30$ –60 km, with amplitudes up to several hundred $\text{m}\cdot\text{s}^{-1}\cdot\text{day}^{-1}$. Although we do not investigate the resulting secondary GWs here because of lack of space, they likely have significant amplitudes (see Figure 7) and can cause significant variability and affect the mean circulation at higher altitudes (Becker & Vadas, 2018).

4.4. Secondary GWS in the Mesosphere at McMurdo

Figure 25 shows $T', u',$ and v' (as defined in section 3 according to filtering in frequency space) scaled by $\sqrt{\bar{\rho}/\bar{\rho}_0}$ at $z = 60$ –100 km on 8–11 July at McMurdo. We see that many of the phase lines that are downward in time at $z = 60$ km in Figures 5 and 18 (corresponding to upward-propagating secondary GWs) extend up to $z = 100$ km in Figure 25. For example, extensions are seen on 9.1–9.7 July in Figure 25a, 9.5–10.5 July in Figure 25b, and 9.3–11 July in Figure 25c.

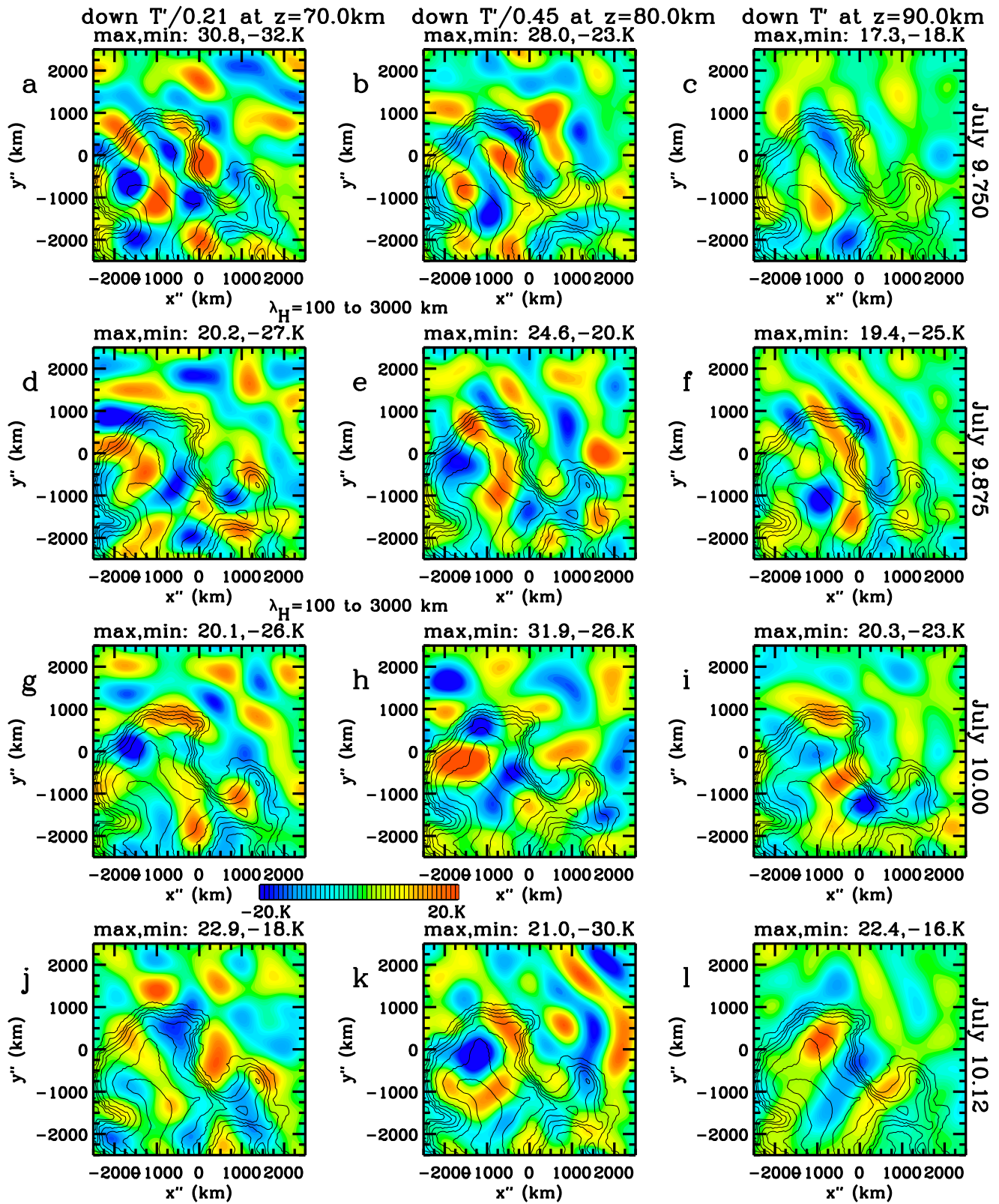


Figure 27. Gravity waves with downward phase lines in time having $1,000 < \lambda_H < 3,000$ km. Row 1: 9.75 July. The left panel shows $T'/(0.21)$ at $z = 70$ km, the middle panel shows $T'/(0.45)$ at $z = 80$ km, and the right panel shows T' at $z = 90$ km. Here $\sqrt{\bar{p}_{z=90}/\bar{p}_{z=70}} = 0.21$ and $\sqrt{\bar{p}_{z=90}/\bar{p}_{z=80}} = 0.45$. Rows 2–4: Same as in row 1 but on 9.875, 10.0, and 10.12 July, respectively. Maximum and minimum values of the plotted quantity are shown at the top of each panel.

If a phase line extends uniformly and continuously from $z = 60$ to 100 km as seen by a vertically pointing observer (such as in Figure 25), then this phase line does not “map out” a single monochromatic GW unless $|\lambda_z| > 40$ km; instead, it maps out the z - t profile of a spectrum of GWs excited by the same coherent source, such as occurs in Figure 6a. This is because a GW propagates obliquely to the zenith (see equation (18)); if an upward-propagating GW is seen by an observer at $z = 60$ km and has $|\lambda_z| \ll 40$ km, then this GW is out of the field of view of the observer (horizontally) at $z \sim 60$ km + $|\lambda_z|$. However, at that altitude, a higher-frequency, faster GW from the same source is then visible. Because the GWs are from the same coherent source, the GW phase lines are continuous with altitude (as in Figure 6a). (Note that in Figure 6a, $|\lambda_z|$ clearly increases with altitude; this is not a wind effect because the background wind is 0.)

Figure 25 also shows that the GWs at $z \sim 90$ km have $|\lambda_z| \sim 20$ – 40 km and $\tau_r \sim 2.5$ – 9 hr. These values are consistent with Chen et al. (2016). Note that the GW amplitudes decrease above $z > 90$ km because the GWs dissipate there from horizontal and vertical turbulent diffusion when the Richardson number is $R_i < 0.25$. This is caused mainly by the background tidal wind variations (Becker & Vadas, 2018).

Figure 26a shows $T' \sqrt{\bar{\rho}/\bar{\rho}_0}$ for all GWs with downward phases in time at $z = 60$ – 100 km. Figures 26b–26d shows those GWs from Figure 26a with $165 < \lambda_H < 1,000$ km, $1,000 < \lambda_H < 3,000$ km, and $3,000 < \lambda_H < 5,050$ km, respectively. We see that for $z > 70$ km, Figure 26a is composed almost entirely of GWs with $1,000 < \lambda_H < 5.050$ km for $z > 70$ km.

Figure 27 shows 2-D horizontal slices of those GWs with $1,000 < \lambda_H < 3,000$ km and with downward phases in time at $z = 70, 80,$ and 90 km on 9.75, 9.875, 10.0, and 10.12 July. Large-scale GWs with $\lambda_H \sim 1,000$ – $2,300$ km are apparent. Most are visible at all three altitudes, although some are “missing” at $z = 90$ km (presumably due to dissipation). Additionally, many of the phase lines are curved (e.g., Figure 27k), indicative of secondary GWs (see Figure 6). Importantly, because these are the scales of the secondary GWs determined in section 4.3.1 (which are much larger than λ_H for the MWs or IGWs generated in the troposphere), we conclude that most of the GWs in Figure 26a at $z > 70$ km are *secondary* GWs generated in the stratosphere.

In Figure 27, the GW phase lines constructively and destructively interfere with each other, thereby creating a “soup” of secondary GWs propagating in different directions above McMurdo. Because these secondary GWs are created by body forces scattered around McMurdo (see Figures 21–24), it is not surprising that GW activity in the upper mesosphere at McMurdo is more uniform (and less characterized by strong downslope MW events at McMurdo) than GW activity in the stratosphere (compare Figures 3 and 4). However, we do note that a weak MW propagated into the mesosphere and dissipated at $z \sim 87$ km in the DEEPWAVE campaign (Bossert et al., 2015), although strong MWs were found to break in the stratosphere (D. C. Fritts, private communication, 2017).

Thus, we conclude that most of the GWs in the mesosphere at McMurdo during July are large-scale secondary GWs created in the stratosphere not primary GWs from the troposphere or lowermost stratosphere (such as MWs or IGWs from unbalanced flow associated with large-amplitude Rossby waves). This is a paradigm shift from previous ideas that assume that mesospheric GWs are primary GWs from the troposphere.

5. Conclusions

In this paper, we analyzed the GWs at McMurdo Station in the Antarctic during July using the high-resolution, GW-resolving KMCM. This model resolves GWs with $\lambda_H \geq 165$ km. We found that there are two dominant GW “hot spots” in the Antarctic; the MWs created by eastward wind over the Antarctic Peninsula and the MWs created by downslope eastward (and often northward) wind from the Transantarctic Mountains to the west coast of the Ross Sea near McMurdo. This result agrees well with satellite and balloon measurements.

We removed the tides and planetary waves via Fourier filtering waves with periods > 11 hr. We found that (a) large-amplitude MW “events” from downslope winds occur at McMurdo every ~ 1.5 – 2.5 days whereby these MWs propagate up to $z \sim 40$ – 60 km and (b) the downslope winds are caused by Rossby waves. During these events, the MW phase lines were upward in time if the background eastward wind accelerated. We also found that the scaled GW amplitudes were smaller by a factor of ~ 10 for $z \sim 80$ – 100 km than for $z < 50$ km, thereby implying that severe wave dissipation occurred at $z \sim 50$ – 80 km. Additionally, we found many “fishbone” structures at $z \sim 30$ – 60 km, which suggested that secondary GWs were excited by horizontal body forces. We calculated the PSD and found that new upward- and downward-propagating GWs were added to the GW spectra in the stratosphere.

Because of the unequal grid spacing near the pole in geophysical coordinates, we developed a new method to transform from geophysical coordinates to equally spaced Cartesian coordinates on a 2-D plane tangent to Earth's surface at McMurdo. We then utilized keograms and horizontal Fourier filtering to determine c_H , λ_H , and the propagation directions of the GWs. During a particular event, we identified two types of primary GWs over McMurdo at $z = 20$ km: MWs and IGWs from Rossby waves over the circumpolar ocean. The MWs had $\lambda_H \approx 230$ km, $c_H \sim 9$ m/s, and $\tau_r \sim 7$ –8 hr, and the smaller-amplitude IGWs had $c_H \sim 35$ m/s, $\tau_r \sim 5$ –6 hr, and $\lambda_H \sim 500$ –800 km. These IGWs had small amplitudes at $z > 25$ km.

We then examined a fishbone structure at $z \sim 30$ –60 km on 9.5–10.5 July. We found that most of the structure was composed of GWs with λ_H much larger than that of the MWs: $\lambda_H \sim 700$ –3,000 km. We isolated those GWs with $\lambda_H \sim 700$ –3,000 km and determined c_H , λ_H , λ_z , τ_r , and the propagation direction for the GWs below and above the knee of the structure at $z_{\text{knee}} = 46$ km. We found that these GWs had similar $c_H = 40$ –60 m/s, $\lambda_H \sim 1,600$ –2,050 km, $|\lambda_z| \sim 18$ –25 km, and propagation directions (southeastward) below and above z_{knee} . Because of this, we identified the GWs in this structure as secondary GWs generated by a body force. We estimated this force to be ~ 400 km northwest of McMurdo, ~ 2.5 hr earlier.

In order to locate this force, we calculated the pseudo momentum flux convergence. We identified a large-amplitude westward body force caused by severe MW dissipation at $z = 46$ km located ~ 400 km northwest of McMurdo, ~ 2.5 hr before the beginning of the fishbone structure. We then showed that the wavelengths and periods of the secondary GWs agreed with the temporal and spatial extents of the body force, thus confirming that this force likely created the secondary GWs in this fishbone structure.

Finally, we showed that most of the GWs at $70 \leq z \leq 100$ km have $\lambda_H = 1,000$ to 3,000 km; thus, most of the GWs in the mesosphere were secondary GWs created in the stratosphere not primary GWs from the troposphere and lowermost stratosphere. This is a very important finding, as it strongly suggests that wintertime GWs in the MLT at southern polar latitudes cannot be simulated by a GCM with GW parameterization that only launches GWs from the troposphere; secondary GWs created in situ in the stratopause region must be included in GCMs in order to properly account for realistic GW activity in the MLT. Note that this result is supported by wintertime observations at McMurdo; Zhao et al. (2017) estimated that the GWs at $z = 30$ –50 km had $\lambda_H \sim 350$ –500 km, which is significantly smaller than the estimated $\lambda_H \sim 400$ –4,000 km in the MLT (Chen & Chu, 2017; Chen et al., 2013).

Hence, this paper and Becker and Vadas (2018) provide a stunning new picture of the middle atmosphere above McMurdo and at southern polar latitudes in general; (a) the GWs in the winter stratosphere are a complicated and highly time and altitude-dependent mixture of primary GWs (MWs and IGWs from Rossby waves) and secondary GWs (from primary GW dissipation), and (b) most of the GWs in the winter MLT are a complicated mixture of secondary GWs from many different local body forces. This coupled dynamical picture can now be simulated with high-resolution, GW-resolving GCMs. It represents a paradigm shift from the results of non-GW-resolving GCMs whereby GWs in the middle atmosphere only include primary GWs (launched in the troposphere) not secondary GWs. Importantly, secondary GW generation yields a significant new source of GWs in the middle atmosphere, MLT and thermosphere. Because these GWs have small amplitudes initially (which allows them to propagate many density scale heights before breaking) and have larger λ_H , $|\lambda_z|$, and c_H than the primary GWs, some of these secondary GWs have the potential to propagate well into the thermosphere before dissipating, thereby potentially significantly influencing the variability and dynamics of the wintertime thermosphere at southern polar latitudes. Secondary GWs (along with byproducts of their dissipation in the thermosphere, e.g., "tertiary" GWs) may account for the large GW hotspot measured by the Challenging Minisatellite Payload satellite ($z \sim 300$ –400 km) in June over the southern Andes (Park et al., 2014). Whether secondary GWs play an important role during other seasons and at other locations is not yet known but will be investigated in future works.

Appendix A: Pseudo Momentum Flux of Inertia-Gravity Waves

The wave-mean flow interaction of GWs having medium and high frequencies is described by the convergence of the momentum flux (i.e., by the divergence of the GW-related Reynolds stress tensor). In the single-column approximation, only the vertical flux of horizontal momentum is considered. The momentum flux density is constant with height in the conservative case for medium-frequency and high-frequency GWs in steady state (Lindzen, 1981). However, when the intrinsic period of a GW is comparable with the inertial frequency, as is the case for (low-frequency) inertia-GWs (IGWs), the wave is accompanied by a Stokes drift and by apparent wave-mean flow interaction, even in the limit of conservative waves in steady state.

Both apparent effects (wave-mean flow interaction and Stokes drift) are balanced by an overturning circulation (e.g., Bretherton, 1969; Dunkerton, 1978; Lindzen, 1971). If the horizontal GW propagation is the x direction on a local f plane, then this circulation lies in the y - z plane. This behavior is analogous to the Ferrel cell that accompanies a baroclinic Rossby wave. Also, in analogy to baroclinic Rossby waves, the wave-mean flow interaction is different from the divergence of the Reynolds stress tensor. In this appendix we derive the wave-mean flow interaction of IGWs in the single-column approximation. We show below that equation (A25) is equivalent to Equation (41) in Fritts and Alexander (2003) for a monochromatic IGW. A WKB analysis for IGWs, however, is not performed here for the sake of brevity.

Our starting point is the isentropic primitive equations on the f plane in the anelastic approximation and in flux form (Becker, 2017, his Appendix):

$$\partial_t \mathbf{v} = -\nabla (\mathbf{v} \cdot \mathbf{v}) - \rho_r^{-1} \partial_z (\rho_r \mathbf{v} w) + \mathbf{v} \times f \mathbf{e}_z - \rho_r^{-1} \nabla \tilde{p}, \quad (\text{A1})$$

$$\partial_z (\rho_r^{-1} \tilde{p}) = -g \rho_r^{-1} \tilde{p}, \quad (\text{A2})$$

$$0 = \nabla \cdot \mathbf{v} + \rho_r^{-1} \partial_z (\rho_r w), \quad (\text{A3})$$

$$c_p \partial_t \tilde{T} = -\nabla \cdot (\tilde{T} \mathbf{v}) - \rho_r^{-1} \partial_z (\rho_r T w) - w g (1 + \tilde{T}/T_r). \quad (\text{A4})$$

Here $\mathbf{v} = (u, v)$ denotes the horizontal velocity field, f is the Coriolis parameter, and w and \mathbf{e}_z respectively denote the vertical velocity and unit vector in the vertical direction. As usual, the scalar product is denoted by a dot and the tensor product by an open circle. Furthermore, t is time, g is the gravitational acceleration, and c_p is the heat capacity per unit mass for constant pressure. In equations (A1)–(A4), we have expanded the thermodynamic variables, pressure, density, and temperature as

$$\begin{aligned} p &= p_r(z) + \tilde{p}(\mathbf{r}, t), \\ \rho &= \rho_r(z) + \tilde{\rho}(\mathbf{r}, t), \\ T &= T_r(z) + \tilde{T}(\mathbf{r}, t), \end{aligned}$$

respectively. Here $\mathbf{r} = (x, y, z)$, the subscript r denotes a hydrostatic reference state that depends on height z only, and the deviations from the reference state are denoted by \tilde{p} , $\tilde{\rho}$, and \tilde{T} . Note that we use the primitive equations because IGWs fulfill the hydrostatic approximation.

We now expand the flow into a slowly varying zonal mean flow (denoted by U , P_u , ρ_u , and T_u) plus deviations from that mean flow, which are due to (a) the aforementioned mean circulation in the y - z plane (denoted by v_m and w_m) and (b) quasi-linear GWs that propagate in the x - z plane (denoted by primes):

$$\begin{aligned} \mathbf{v} &= U(y, z, t) \mathbf{e}_x + v_m(y, z, t) \mathbf{e}_y + w_m(y, z, t) \mathbf{e}_z + \mathbf{v}'(\mathbf{r}, t), \\ \tilde{p} &= p_u(y, z, t) + p'(\mathbf{r}, t), \\ \tilde{\rho} &= \rho_u(y, z, t) + \rho'(\mathbf{r}, t), \\ \tilde{T} &= T_u(y, z, t) + T'(\mathbf{r}, t). \end{aligned} \quad (\text{A5})$$

Here $p_u(y, z, t)$ is the slowly varying pressure perturbation that balances the mean flow; when there are no GWs, this relation is $fU = -\rho_r(z)^{-1} \partial_y \tilde{p}_u$. This pressure deviation is associated with the slowly varying density and temperature deviations, ρ_u and T_u , respectively, according to (A2) and the anelastic relation

$$\tilde{T}/T_r = -\tilde{\rho}/\rho_r. \quad (\text{A6})$$

Since v_m and w_m are slowly varying and are of order the wave perturbations, we can neglect their derivatives in the momentum and thermodynamic equations. However, we must take into account the Coriolis force and the adiabatic heating due to v_m and w_m . We assume that the reference state is isothermal. In order to obtain the mean-flow equations in the single-column approximation, we assume that the wave field is periodic in the x direction. All mean flow variables and the mean circulation have slowly varying dependencies on y, z , and t .

Given the above approximations, the resulting equations that describe the total flow can be written as

$$\begin{aligned} \partial_t U \mathbf{e}_x + \partial_t \mathbf{v}' = & -U \partial_x \mathbf{v}' - v' \partial_y U \mathbf{e}_x - w' \partial_z U \mathbf{e}_x - \nabla \cdot (\mathbf{v}' \circ \mathbf{v}') \\ & - \rho_r^{-1} \partial_z (\rho_r \mathbf{v}' w') + (U \mathbf{e}_x + \mathbf{v}' + v_m \mathbf{e}_y) \times f \mathbf{e}_z - \rho_r^{-1} (\nabla p_u + \nabla p'), \end{aligned} \quad (\text{A7})$$

$$\partial_z (\rho_r^{-1} (p_u + p')) = -g \rho_r^{-1} (\rho_u + \rho'), \quad (\text{A8})$$

$$0 = \nabla \cdot \mathbf{v}' + \partial_y v_m + \rho_r^{-1} \partial_z (\rho_r (w' + w_m)), \quad (\text{A9})$$

$$\begin{aligned} \partial_t T_u + \partial_t T' = & -U \partial_x T' - v' \partial_y T_u - w' \partial_z T_u - \nabla \cdot (T' \mathbf{v}') \\ & - \rho_r^{-1} \partial_z (\rho_r T' w') - c_p^{-1} g (w' + w_m) (1 - \rho_r^{-1} (\rho_u + \rho')). \end{aligned} \quad (\text{A10})$$

The resulting linear wave equations are

$$(\partial_t + U \partial_x) u' + v' \partial_y U + w' \partial_z U = f v' - \rho_r^{-1} \partial_x p', \quad (\text{A11})$$

$$(\partial_t + U \partial_x) v' = -f u', \quad (\text{A12})$$

$$\partial_z (\rho_r^{-1} p') = -g \rho_r^{-1} \rho', \quad (\text{A13})$$

$$0 = \nabla \cdot \mathbf{v}' + \rho_r^{-1} \partial_z (\rho_r w'), \quad (\text{A14})$$

$$(\partial_t + U \partial_x) T' + v' \partial_y T_u + w' \partial_z T_u = -c_p^{-1} g w'. \quad (\text{A15})$$

These equations lead to the well-known dispersion and polarization relations for medium-frequency and low-frequency (inertia) GWs if we neglect the advection of U and T_u by v' and w' in equations (A11) and (A15). Indeed, these terms are negligible in the WKB approximation for the waves, but they must be retained when considering the energy budgets of the waves.

The mean-flow equations are obtained by subtracting equations (A11)–(A15) from equations (A7)–(A10) and averaging over the GW scales in x and t (indicated by \bar{X} for any variable X):

$$\partial_t U = -\rho_r^{-1} \partial_z (\rho_r \overline{u' w'}) + f v_m \quad (\text{A16})$$

$$0 = -f U - \rho_r^{-1} \partial_y p_u \quad (\text{A17})$$

$$\partial_z (\rho_r^{-1} p_u) = -g \rho_r^{-1} \rho_u = g T_r^{-1} T_u \quad (\text{A18})$$

$$0 = \partial_y v_m + \rho_r^{-1} \partial_z (\rho_r w_m) \quad (\text{A19})$$

$$\partial_t T_u = -\partial_y (\overline{T' v'}) - c_p^{-1} g w_m. \quad (\text{A20})$$

Here $-\partial_x (\overline{u' u'})$ and $-\partial_x (\overline{T' u'})$ are omitted in equations (A16) and (A20), respectively, because of the single-column approximation. Furthermore, we used $\overline{u' v'} = 0$, which follows from equation (A12), and we used $\overline{T' w'} = 0$, which holds when we neglect $v' \partial_y T_u + w' \partial_z T_u$ in (A15) according to the WKB approximation. Furthermore, we considered only the leading term of the adiabatic heating.

For any conservative linear GW field in steady state and without critical levels, the wave-mean flow interaction is 0. However, the heat flux term in equation (A20) is generally not 0. According to Bretherton (1969) and Lindzen (1971), the momentum flux density, $\rho_r \overline{u' w'}$, is also not constant with height for IGWs subject to refraction by a slowly varying mean flow. Instead the vertical component of the so-called pseudo-momentum flux density is constant with height for conservative IGWs in steady state. In the following, we exploit this insight to recapitulate the general form of the momentum deposition and the pseudo-momentum flux density from IGWs.

Since the left-hand side of equation (A20) must be 0 for conservative IGWs in steady state, we can eliminate the vertical component of the circulation in the y - z plane,

$$w_m = -g^{-1} c_p \partial_y (\overline{T' v'}), \quad (\text{A21})$$

where $-\rho_r w_m$ is the vertical Stokes drift of the waves. Then, the continuity equation (A19) is fulfilled for

$$v_m = \rho_r^{-1} \partial_z (\rho_r g^{-1} c_p \overline{T' v'}), \quad (\text{A22})$$

and $-\rho_r v_m$ is the Stokes drift in y direction. Using equation (A22), the mean-flow momentum equation (A16) becomes

$$\partial_t U = -\rho_r^{-1} \partial_z \left(\rho_r \overline{u' w'} - \rho_r f c_p g^{-1} \overline{T' v'} \right). \quad (\text{A23})$$

Note the analogy of equation (A23) to the transformed Eulerian mean zonal-mean zonal momentum equation on the sphere (Andrews et al., 1987; Becker, 2017).

For a monochromatic wave with intrinsic frequency ω_i , we obtain $-i\omega_i T' = -g c_p^{-1} w'$ from equation (A15) and $-i\omega_i v' = -f u'$ from equation (A12). In this case, equation (A23) reduces to

$$\partial_t U = -\rho_r^{-1} \partial_z \left(\rho_r \overline{u' w'} (1 - f^2 \omega_i^{-2}) \right). \quad (\text{A24})$$

Indeed, the right-hand side of equation (A24) is 0 for an IGW that is linear and conservative.

Since all azimuthal (horizontal) directions are equivalent on the f plane, we can write down the general form of the pseudo-momentum flux density of IGWs as

$$\mathbf{F} = \rho_r \overline{\mathbf{v}' w'} + \rho_r f c_p g^{-1} \mathbf{e}_z \times \overline{T' \mathbf{v}'}. \quad (\text{A25})$$

Here we used again the fact that the horizontal velocity component perpendicular to the horizontal propagation direction is out of phase with w' and is in phase with T' . In the limit of a monochromatic GW, we obtain

$$\mathbf{F} = \rho_r \overline{\mathbf{v}' w'} (1 - f^2 \omega_i^{-2}). \quad (\text{A26})$$

The drag per unit mass (horizontal acceleration of the mean flow) due to IGWs that are not conservative or are not in steady state is generally given by $-\rho_r \partial_z \mathbf{F}$, with \mathbf{F} given by equation (A25) in the general case and by equation (A26) for a monochromatic wave.

Appendix B: Transformation from Geophysical to 2-D Cartesian Coordinates

In order to determine the parameters of small-amplitude GWs, it is necessary to employ horizontal filtering techniques. However, geophysical coordinates are unequally spaced (especially near the pole), therefore preventing simple Fourier filtering techniques.

In order to bypass this constraint, we develop a new method to transform our model data from geophysical coordinates to a 2-D (equally spaced) Cartesian plane centered at the longitude ϕ_1 and latitude θ_1 of interest. (For example, the plane could be centered at McMurdo: $\phi_1 = 166.69^\circ$ and $\theta_1 = -77.84^\circ$.) This 2-D plane is perpendicular to a line extending from Earth's center to this location and is therefore tangent to Earth's surface at ϕ_1 and θ_1 . On this plane, we ascribe (x'', y'') coordinates, with positive x'' in the eastward direction and positive y'' in the northward direction (towards the equator) at $x'' = y'' = 0$.

Consider a typical Cartesian coordinate system fixed to Earth, with longitude ϕ and latitude θ . In this system, the x axis lies from the center of the Earth through Greenwich (at the equator), the y axis is 90° from x (through the equator), and the z axis is upward from the center of the Earth through the North Pole. Consider two points on a sphere having radius $r = R_{\text{Earth}} + z$, where z is fixed. The first point has the coordinate (ϕ_1, θ_1) , and the second point has the coordinate (ϕ_2, θ_2) . In Cartesian space, the vector for each point is given by

$$\mathbf{r} = r \cos \theta \cos \phi \hat{\mathbf{i}}_C + r \cos \theta \sin \phi \hat{\mathbf{j}}_C + r \sin \theta \hat{\mathbf{k}}_C, \quad (\text{B1})$$

where $\hat{\mathbf{i}}_C, \hat{\mathbf{j}}_C,$ and $\hat{\mathbf{k}}_C$ are the Cartesian unit vectors in the $x, y,$ and z directions, respectively. Note that these unit vectors are fixed to Earth and do not depend on the latitude and longitude (as they do in geophysical spherical coordinates—see below). Below, we refer to geophysical spherical coordinates as “geophysical” coordinates. Figure B1a shows this Cartesian coordinate system, along with the two vectors \mathbf{r}_1 and \mathbf{r}_2 . The radius of the sphere is $r = R_{\text{Earth}} + z$. The distance between \mathbf{r}_1 and \mathbf{r}_2 along the sphere is l , and the angle between them is ψ . Because

$$\mathbf{r}_1 \cdot \mathbf{r}_2 = |\mathbf{r}_1| |\mathbf{r}_2| \cos \psi, \quad (\text{B2})$$

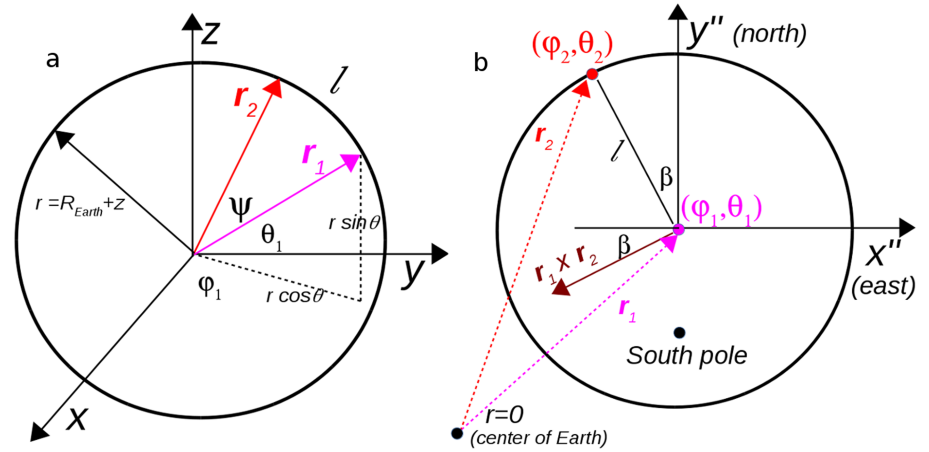


Figure B1. (a) Geometry of the vectors \mathbf{r}_1 (purple arrow) and \mathbf{r}_2 (red arrow) in Cartesian coordinates. The surface of the sphere has a radius of $r = R_{\text{Earth}} + z$. Both vectors have radii r . The center of Earth is located at the intersection of the x , y , and z axes. The longitude (ϕ) and latitude (θ) of \mathbf{r}_1 are displayed, along with the z component ($r \sin \theta$) and the projection in the $x - y$ plane ($r \cos \theta$). The distance between \mathbf{r}_1 and \mathbf{r}_2 along the sphere is l , and the angle between them is ψ . (b) Geometry of \mathbf{r}_1 and \mathbf{r}_2 in the (x'', y'') coordinates on a 2-D plane tangent to Earth at (ϕ_1, θ_1) . Positive x'' and y'' denotes east and north in geophysical coordinates, respectively, only at (ϕ_1, θ_1) . The center of the Earth is shown in the lower left corner, and \mathbf{r}_1 and \mathbf{r}_2 are shown as the purple and red dotted arrows, respectively. The azimuth angle between the line connecting \mathbf{r}_1 and \mathbf{r}_2 with north is β . $\mathbf{r}_1 \times \mathbf{r}_2$ is the brown arrow. The south pole is the black dot.

and $|\mathbf{r}_1| = |\mathbf{r}_2| = r$, the distance between \mathbf{r}_1 and \mathbf{r}_2 along the surface of this sphere is

$$l = r\psi = r \cos^{-1} \left(\frac{\mathbf{r}_1 \cdot \mathbf{r}_2}{r^2} \right) \quad (\text{B3})$$

$$= r \cos^{-1} (\cos \theta_1 \cos \theta_2 \cos(\phi_2 - \phi_1) + \sin \theta_1 \sin \theta_2).$$

Figure B1b shows the geophysical coordinate system at \mathbf{r}_1 , which depends on its longitude (ϕ_1) and latitude (θ_1). Here east is positive x'' , and north is positive y'' . The azimuth angle (i.e., clockwise from north) that the line connecting \mathbf{r}_1 and \mathbf{r}_2 makes with true north is β . Note that $\mathbf{r}_1 \times \mathbf{r}_2$ lies in the 2-D plane tangent to Earth at \mathbf{r}_1 .

To determine the azimuth β , we note that

$$(-\mathbf{r}_1 \times \mathbf{r}_2) \cdot (\hat{\mathbf{i}}_{\text{geo}}) = |\mathbf{r}_1 \times \mathbf{r}_2| |\hat{\mathbf{i}}_{\text{geo}}| \cos \beta, \quad (\text{B4})$$

where $\hat{\mathbf{i}}_{\text{geo}}$ is the east unit vector in geophysical (geo) coordinates. Since $|\hat{\mathbf{i}}_{\text{geo}}| = 1$,

$$\beta = \cos^{-1} \left(-\frac{(\mathbf{r}_1 \times \mathbf{r}_2) \cdot \hat{\mathbf{i}}_{\text{geo}}}{|\mathbf{r}_1 \times \mathbf{r}_2|} \right). \quad (\text{B5})$$

Using equation (B1), the components of $\mathbf{r}_1 \times \mathbf{r}_2$ in Cartesian coordinates are

$$\begin{aligned} \mathbf{r}_1 \times \mathbf{r}_2 = r^2 \{ & [\cos \theta_1 \sin \phi_1 \sin \theta_2 - \cos \theta_2 \sin \phi_2 \sin \theta_1] \hat{\mathbf{i}}_C \\ & - [\cos \theta_1 \cos \phi_1 \sin \theta_2 - \cos \theta_2 \cos \phi_2 \sin \theta_1] \hat{\mathbf{j}}_C \\ & + [\cos \theta_1 \cos \phi_1 \cos \theta_2 \sin \phi_2 - \cos \theta_1 \sin \phi_1 \cos \theta_2 \cos \phi_2] \hat{\mathbf{k}}_C \}. \end{aligned} \quad (\text{B6})$$

In order to evaluate equation (B5), we calculate $\mathbf{r}_1 \times \mathbf{r}_2$ in Cartesian coordinates, then transform this vector to geophysical coordinates at \mathbf{r}_1 . To perform this transformation from Cartesian to geophysical coordinates at (ϕ_1, θ_1) , we first rotate by $\xi = \phi_1 + 90^\circ$ counterclockwise in the x - y plane and then by $\zeta = 90^\circ - \theta_1$ counterclockwise in the y' - z' plane.

We now formulate this transformation. Consider a vector with Cartesian coordinates $(x, y, z) = x\hat{\mathbf{i}}_C + y\hat{\mathbf{j}}_C + z\hat{\mathbf{k}}_C$. We first rotate the coordinate system by $\xi = \phi_1 + 90^\circ$ counterclockwise in the x - y plane. The coordinates for this vector in this new coordinate system is (x', y', z') :

$$\begin{aligned} x' &= x \cos \xi + y \sin \xi, \\ y' &= -x \sin \xi + y \cos \xi, \\ z' &= z. \end{aligned} \quad (\text{B7})$$

Next we rotate the coordinate system by $\zeta = 90^\circ - \theta_1$ counterclockwise in the y' - z' plane. The coordinates for this vector in this geophysical coordinate system is (x'', y'', z'') :

$$\begin{aligned}x'' &= x', \\y'' &= y' \cos \zeta + z' \sin \zeta, \\z'' &= -y' \sin \zeta + z' \cos \zeta.\end{aligned}\tag{B8}$$

Equations (B7) and (B8) apply to the transformation of any vector from Cartesian to geophysical coordinates at (ϕ_1, θ_1) . We now apply these transformations to the vector $(\mathbf{r}_1 \times \mathbf{r}_2)$ to determine the angle from north between the line bisecting \mathbf{r}_1 and \mathbf{r}_2 . Using equation (B6), we find that

$$\begin{aligned}(\mathbf{r}_1 \times \mathbf{r}_2) \cdot \hat{\mathbf{i}}_{\text{geo}} &= x'' = x' \cos \xi + y' \sin \xi \\&= r^2 \{ (\cos \theta_1 \sin \phi_1 \sin \theta_2 - \cos \theta_2 \sin \phi_2 \sin \theta_1) \cos \xi + \\&\quad (-\cos \theta_1 \cos \phi_1 \sin \theta_2 + \cos \theta_2 \cos \phi_2 \sin \theta_1) \sin \xi \},\end{aligned}\tag{B9}$$

where x and y here are the $\hat{\mathbf{i}}_C$ and $\hat{\mathbf{j}}_C$ components of $\mathbf{r}_1 \times \mathbf{r}_2$ in equation (B6). Then we use equation (B5) to determine β .

It is then straightforward to determine the (x'', y'') coordinates of \mathbf{r}_2 in the 2-D Cartesian plane. We define positive x'' eastward and positive y'' northward at $x'' = y'' = 0$ (as in Figure B1b). The coordinate of \mathbf{r}_2 in this plane is

$$\begin{aligned}x'' &= l \sin \beta, \\y'' &= l \cos \beta.\end{aligned}\tag{B10}$$

To transform the vector $\mathbf{v} = (v_1, v_2)$, such as the horizontal velocity, in geophysical coordinates at (ϕ_2, θ_2) to the vector $\mathbf{v}'' = (v_1'', v_2'')$ in the 2-D x'' - y'' plane tangent to Earth at (ϕ_1, θ_1) , we rotate \mathbf{v} clockwise by the angle $\phi_2 - \phi_1$:

$$\begin{aligned}v_1'' &= v_1 \cos(\phi_2 - \phi_1) + v_2 \sin(\phi_2 - \phi_1), \\v_2'' &= -v_1 \sin(\phi_2 - \phi_1) + v_2 \cos(\phi_2 - \phi_1).\end{aligned}\tag{B11}$$

This is the procedure we use to convert the zonal and meridional velocities at (ϕ_2, θ_2) to the “new” velocity vector \mathbf{v}'' in the 2-D x'' - y'' plane.

Acknowledgments

We would like to thank three anonymous reviewers for helpful comments. S. L. V. was supported by NSF grants PLR-1246405 and AGS-1552315. E. B. was supported by the Collaborative Research Centre TRR 181 (subproject T1) funded by the German Research Foundation. E. B. would like to thank NCAR/HAO and IAP for the sabbatical opportunity at NCAR/HAO. The model data shown in this paper is available via NWRA's website at https://www.cora.nwra.com/vadas/VadasBecker_JGR_2018_files/.

References

- Alexander, M. J., Gille, J., Cavanaugh, C., Coffey, M., Craig, C., Eden, T., et al. (2008). Global estimates of gravity wave momentum flux from High Resolution Dynamics Limb Sounder observations. *Journal of Geophysical Research*, *113*, D15S18. <https://doi.org/10.1029/2010JD008807>
- Alexander, S. P., Klekociuk, A. R., & Murphy, D. J. (2011). Rayleigh lidar observations of gravity wave activity in the winter upper stratosphere and lower mesosphere above Davis, Antarctica (69°S, 78°E). *Journal of Geophysical Research*, *116*, D13109. <https://doi.org/10.1029/2010JD015164>
- Alexander, M. J., & Teitelbaum, H. (2007). Observation and analysis of a large amplitude mountain wave event over the Antarctic peninsula. *Journal of Geophysical Research*, *112*, D21103. <https://doi.org/10.1029/2006JD008368>
- Alexander, M. J., & Teitelbaum, H. (2011). Three-dimensional properties of Andes mountain waves observed by satellite: A case study. *Journal of Geophysical Research*, *116*, D23110. <https://doi.org/10.1029/2011JD016151>
- Andrews, D. G., Holton, J. R., & Leovy, C. B. (1987). *Middle atmosphere dynamics*. Florida: Academic Press.
- Bacmeister, J. T., & Schoeberl, M. R. (1989). Breakdown of vertically propagating two-dimensional gravity waves forced by orography. *Journal of the Atmospheric Sciences*, *46*, 2109–2134.
- Becker, E. (2009). Sensitivity of the upper mesosphere to the Lorenz energy cycle of the troposphere. *Journal of the Atmospheric Sciences*, *66*, 647–666. <https://doi.org/10.1175/2008JAS2735.1>
- Becker, E. (2012). Dynamical control of the middle atmosphere. *Space Science Reviews*, *168*, 283–314. <https://doi.org/10.1007/s11214-011-9841-5>
- Becker, E. (2017). Mean-flow effects of thermal tides in the mesosphere and lower thermosphere. *Journal of the Atmospheric Sciences*, *74*, 2043–2063. <https://doi.org/10.1175/JAS-D-16-0194.1>
- Becker, E., Knöpfel, R., & Lübken, F.-J. (2015). Dynamically induced hemispheric differences in the seasonal cycle of the summer polar mesopause. *Journal of Atmospheric and Solar - Terrestrial Physics*, *129*, 128–141. <https://doi.org/10.1016/j.jastp.2015.04.014>
- Becker, E., & Vadas, S. L. (2018). Secondary gravity waves in the winter mesosphere: Results from a high-resolution global circulation model. *Journal of Geophysical Research: Atmospheres*, *123*, 2605–2627. <https://doi.org/10.1002/2017JD027460>
- Bossert, K., Fritts, D. C., Pautet, P.-D., Williams, B. P., Taylor, M. J., Kaifler, B., et al. (2015). Momentum flux estimates accompanying multiscale gravity waves over Mount Cook, New Zealand, on 13 July 2014 during the DEEPWAVE campaign. *Journal of Geophysical Research: Atmospheres*, *120*, 9323–9337. <https://doi.org/10.1002/2015JD023197>
- Bossert, K., Kruse, C. G., Heale, C. J., Fritts, D. C., Williams, B. P., Snively, J. B., et al. (2017). Secondary gravity wave generation over New Zealand during the DEEPWAVE campaign. *Journal of Geophysical Research: Atmospheres*, *122*, 7834–7850. <https://doi.org/10.1002/2016JD026079>

- Bretherton, F. P. (1969). Momentum transport by gravity waves. *Quarterly Journal of the Royal Meteorological Society*, *95*, 213–243. <https://doi.org/10.1002/qj.49709540402>
- Chen, C., & Chu, X. (2017). Two-dimensional Morlet wavelet transform and its application to wave recognition methodology of automatically extracting two-dimensional wave packets from lidar observations in Antarctica. *Journal of Atmospheric and Solar-Terrestrial Physics*, *162*, 28–47. <https://doi.org/10.1016/j.jastp.2016.10.016>
- Chen, C., Chu, X., McDonald, A. J., Vadas, S. L., Yu, Z., Fong, W., & Lu, X. (2013). Inertia-gravity waves in Antarctica: A case study using simultaneous lidar and radar measurements at McMurdo/Scott Base (77.8°S, 166.7°E). *Journal of Geophysical Research: Atmospheres*, *118*, 2794–2808. <https://doi.org/10.1002/jgrd.50318>
- Chen, C., Chu, X., Zhao, J., Roberts, B. R., Yu, Z., Fong, W., et al. (2016). Lidar observations of persistent gravity waves with periods of 3–10 h in the Antarctic middle and upper atmosphere at McMurdo (77.83°S, 166.67°E). *Journal of Geophysical Research: Space Physics*, *121*, 1483–1502. <https://doi.org/10.1002/2015JA022127>
- Chu, X., Yu, Z., Gardner, C. S., Chen, C., & Fong, W. (2011). Lidar observations of neutral Fe layers and fast gravity waves in the thermosphere (110–155 km) at McMurdo (77.8°S, 166.7°E), Antarctica. *Geophysical Research Letters*, *38*, L23807. <https://doi.org/10.1029/2011GL050016>
- Chun, H.-Y., & Kim, Y.-H. (2008). Secondary waves generated by breaking of convective gravity waves in the mesosphere and their influence in the wave momentum flux. *Journal of Geophysical Research*, *113*, D23107. <https://doi.org/10.1029/2008JD009792>
- de la Torre, A., & Alexander, P. (2005). Gravity waves above Andes detected from GPS radio occultation temperature profiles: Mountain forcing? *Geophysical Research Letters*, *32*, L17815. <https://doi.org/10.1029/2005GL022959>
- Dunkerton, T. J. (1978). On the mean meridional mass motions of the stratosphere and mesosphere. *Journal of the Atmospheric Sciences*, *35*, 2325–2333.
- Eckermann, S., & Marks, C. (1996). An idealized ray model of gravity wave-tidal interactions. *Journal of Geophysical Research*, *101*(D16), 21,195–21,212. <https://doi.org/10.1029/96JD01660>
- Eckermann, S., & Preusse, P. (1999). Global measurements of stratospheric mountain waves from space. *Science*, *286*(5444), 1534–1537. <https://doi.org/10.1126/science.286.5444.1534>
- Ern, M., Preusse, P., Alexander, M. J., & Warner, C. D. (2004). Absolute values of gravity wave momentum flux derived from satellite data. *Journal of Geophysical Research*, *109*, D20103. <https://doi.org/10.1029/2004JD004752>
- Ern, M., Preusse, P., Gille, J. C., Hepplewhite, C. L., Mlynczak, M. G., Russell III, J. M., & Riese, M. (2011). Implications for atmospheric dynamics derived from global observations of gravity wave momentum flux in stratosphere and mesosphere. *Journal of Geophysical Research*, *116*, D19107. <https://doi.org/10.1029/2011JD015821>
- Franke, P. M., & Robinson, W. A. (1999). Nonlinear behavior in the propagation of atmospheric gravity waves. *Journal of the Atmospheric Sciences*, *56*, 3010–3027.
- Fritts, D. C., & Alexander, M. J. (2003). Gravity wave dynamics and effects in the middle atmosphere. *Reviews of Geophysics*, *41*(1), 1003. <https://doi.org/10.1029/2001RG000106>
- Fritts, D. C., Smith, R. B., Taylor, M. J., Doyle, J. D., Eckermann, S. D., Dörnbrack, A., et al. (2016). The deep propagating gravity wave experiment (DEEPWAVE): An airborne and ground-based exploration of gravity wave propagation and effects from their sources throughout the lower and middle atmosphere. *Bulletin of the American Meteorological Society*, *97*, 425–453. <https://doi.org/10.1175/BAMS-D-14-00269.1>
- Fritts, D. C., Vadas, S. L., Wan, K., & Werne, J. A. (2006). Mean and variable forcing of the middle atmosphere by gravity waves. *Journal of Atmospheric and Solar - Terrestrial Physics*, *68*, 247–265.
- Gong, J., Wu, D. L., & Eckermann, S. D. (2012). Gravity wave variances and propagation derived from AIRS radiances. *Atmospheric Chemical Physics*, *12*, 1701–1720. <https://doi.org/10.5194/acp-12-1701-2012>
- Heale, C. J., Bossert, K., Snively, J. B., Fritts, D. C., Pautet, P.-D., & Taylor, M. J. (2017). Numerical modeling of a multiscale gravity wave event and its airglow signatures over Mount Cook, New Zealand, during the DEEPWAVE campaign. *Journal of Geophysical Research: Atmospheres*, *122*, 846–860. <https://doi.org/10.1002/2016JD025700>
- Hendricks, E. A., Doyle, J. D., Eckermann, S. D., Jiang, Q., & Reinecke, P. A. (2014). What is the source of the stratospheric gravity wave belt in austral winter. *Journal of the Atmospheric Sciences*, *71*, 1583–1592. <https://doi.org/10.1175/JAS-D-13-0332.1>
- Hines, C. O. (1960). Internal atmospheric gravity waves at ionospheric heights. *Canadian Journal de Physique*, *38*, 1441–1481.
- Hoffmann, P., & Alexander, M. J. (2009). Retrieval of stratospheric temperatures from atmospheric infrared sounder radiance measurements for gravity wave studies. *Journal of Geophysical Research*, *114*, D07105. <https://doi.org/10.1029/2008JD011241>
- Hoffmann, P., Becker, E., Singer, W., & Placke, M. (2010). Seasonal variation of mesospheric waves at northern middle and high latitudes. *Journal of Atmospheric and Solar - Terrestrial Physics*, *72*, 1068–1079. <https://doi.org/10.1016/j.jastp.2010.07.002>
- Hoffmann, L., Xue, X., & Alexander, M. J. (2013). A global view of stratospheric gravity wave hotspots located with atmospheric infrared sounder observations. *Journal of Geophysical Research: Atmospheres*, *118*, 416–434. <https://doi.org/10.1029/2012jd018658>
- Holton, J. R. (1992). *An introduction to dynamic meteorology* (507 pp.). San Diego, CA: Academic Press.
- Jiang, J. H., Wu, D. L., & Eckermann, S. D. (2002). Upper atmosphere research satellite (UARS) MLS observation of mountain waves over the Andes. *Journal of Geophysical Research*, *107*(D20), 8273. <https://doi.org/10.1029/2002JD002091>
- Kaifler, B., Lübken, F.-J., Höffner, J., Morris, R. J., & Viehl, T. P. (2015). Lidar observations of gravity wave activity in the middle atmosphere over Davis (69°S, 78°E), Antarctica. *Journal of Geophysical Research: Atmospheres*, *120*, 4506–4521. <https://doi.org/10.1002/2014JD022879>
- Lighthill, J. (1978). *Waves in fluids* (504 pp.). Cambridge: Cambridge University Press.
- Lindzen, R. S. (1971). Equatorial waves in shear. Part I. *Journal of the Atmospheric Sciences*, *28*, 609–622.
- Lindzen, R. S. (1981). Turbulence and stress owing to gravity wave and tidal breakdown. *Journal of Geophysical Research*, *86*(C10), 9707–9714.
- Liu, H.-L., McInerney, J., Santos, S., Lauritzen, P. H., Taylor, M. A., & Pedatella, N. M. (2014). Gravity waves simulated by high-resolution Whole Atmosphere Community Climate Model. *Geophysical Research Letter*, *41*, 9106–9112. <https://doi.org/10.1002/2014GL02468>
- Lu, X., Chu, X., Chen, C., Nguyen, V., & Smith, A. K. (2017). First observations of short-period eastward propagating planetary waves from the stratosphere to the lower thermosphere (110 km) in winter Antarctica. *Geophysical Research Letters*, *44*, 10,744–10,753. <https://doi.org/10.1002/2017GL075641>
- Lu, X., Chu, X., Fong, W., Chen, C., Yu, Z., Roberts, B. R., & McDonald, A. J. (2015). Vertical evolution of potential energy density and vertical wave number spectrum of Antarctic gravity waves from 35 to 105 km at McMurdo (77.8°S, 166.7°E). *Journal of Geophysical Research: Atmospheres*, *120*, 2719–2737. <https://doi.org/10.1002/2014JD022751>
- Lu, X., Chu, X., Fuller-Rowell, T., Chang, L., Fong, W., & Yu, Z. (2013). Eastward propagating planetary waves with periods of 15 days in the winter Antarctic stratosphere as revealed by MERRA and Lidar. *Journal of Geophysical Research: Atmospheres*, *118*, 9565–9578. <https://doi.org/10.1002/jgrd.50717>

- McFarlane, N. A. (1987). The effect of orographically excited gravity wave drag on the general circulation of the lower stratosphere and troposphere. *Journal of the Atmospheric Sciences*, *44*, 1775–1800.
- Murphy, D. J., Alexander, S. P., Klekociuk, A. R., Love, P. T., & Vincent, R. A. (2014). Radiosonde observations of gravity waves in the lower stratosphere over Davis, Antarctica. *Journal of Geophysical Research: Atmospheres*, *119*, 11,973–11,996. <https://doi.org/10.1002/2014JD022448>
- Nicolls, M. J., Varney, R. H., Vadas, S. L., Stamus, P. A., Heinselman, C. J., Cosgrove, R. B., & Kelley, M. C. (2010). Influence of an inertia-gravity wave on mesospheric dynamics: A case study with the Poker Flat Incoherent Scatter Radar. *Journal of Geophysical Research*, *115*, D00N02. <https://doi.org/10.1029/2010JD014042>
- O'Sullivan, D., & Dunkerton, T. J. (1995). Generation of inertia-gravity waves in a simulated life-cycle of baroclinic instability. *Journal of the Atmospheric Sciences*, *52*, 3695–3716.
- Park, J., Lühr, H., Lee, C., Kim, Y. H., Jee, G., & Kim, J.-H. (2014). A climatology of medium-scale gravity wave activity in the midlatitude/low-latitude daytime upper thermosphere as observed by CHAMP. *Journal of Geophysical Research: Space Physics*, *119*, 2187–2196. <https://doi.org/10.1002/2013JA019705>
- Plougonven, R., Hertzog, A., & Teitelbaum, H. (2008). Observations and simulations of a large-amplitude mountain wave breaking over the Antarctic Peninsula. *Journal of Geophysical Research*, *113*, D16113. <https://doi.org/10.1029/2007JD009739>
- Plougonven, R., & Zhang, F. (2014). Internal gravity waves from atmospheric jets and fronts. *Reviews of Geophysics*, *52*, 33–76. <https://doi.org/10.1002/2012RG000419>
- Preusse, P., Dörnbrack, A., Eckermann, S. D., Riese, M., Schaeler, B., Bacmeister, J. T., et al. (2002). Space-based measurements of stratospheric mountain waves by CRISTA. 1. Sensitivity analysis method, and a case study. *Journal of Geophysical Research*, *107*(32), 8178. <https://doi.org/10.1029/2001JD000699>
- Preusse, P., Ern, M., Eckermann, S. D., Warner, C. D., Picard, R. H., Knieling, P., et al. (2006). Tropopause to mesopause gravity waves in August: Measurement and modeling. *Journal of Atmospheric and Solar-Terrestrial Physics*, *68*, 1730–1751.
- Sato, K., Tateno, S., Watanabe, S., & Kawatani, Y. (2012). Gravity wave characteristics in the southern hemisphere revealed by a high-resolution middle-atmosphere general circulation model. *Journal of the Atmospheric Sciences*, *69*, 1378–1396. <https://doi.org/10.1175/JAS-D-11-0101.1>
- Sato, K., Watanabe, S., Kawatani, Y., Tomikawa, Y., Miyazaki, K., & Takahashi, M. (2009). On the origins of mesospheric gravity waves. *Geophysical Research Letters*, *36*, L19801. <https://doi.org/10.1029/2009GL039908>
- Sato, K., & Yoshiki, M. (2008). Gravity wave generation around the polar vortex in the stratosphere revealed by 3-hourly radiosonde observations at Syowa station. *Journal of the Atmospheric Sciences*, *65*, 3719–3735.
- Satomura, T., & Sato, K. (1999). Secondary generation of gravity waves associated with the breaking of mountain waves. *Journal of the Atmospheric Sciences*, *56*, 3847–3858.
- Senf, F., & Achatz, U. (2011). On the impact of middle-atmosphere thermal tides on the propagation and dissipation of gravity waves. *Journal of Geophysical Research*, *116*, D24110. <https://doi.org/10.1029/2011JD015794>
- Shibuya, R., Sato, K., Tsutsumi, M., Sato, T., Tomikawa, Y., Nishimura, K., & Kohma, M. (2017). Quasi-12 h inertia-gravity waves in the lower mesosphere observed by the PANSY radar at Syowa station (39.6°E, 69.0°S). *Atmospheric Chemical Physics*, *17*, 6455–6476.
- Tsuda, T., Nishida, M., Rocken, C., & Ware, R. H. (2000). A global morphology of gravity wave activity in the stratosphere revealed by the GPS occultation data (GPS/MET). *Journal of Geophysical Research*, *105*, 7257–7273.
- Vadas, S. L. (2013). Compressible *f*-plane solutions to body forces, heatings, and coolings, and application to the primary and secondary gravity waves generated by a deep convective plume. *Journal of Geophysical Research: Space Physics*, *118*, 2377–2397. <https://doi.org/10.1002/jgra.50163>
- Vadas, S. L., & Fritts, D. C. (2001). Gravity wave radiation and mean responses to local body forces in the atmosphere. *Journal of the Atmospheric Sciences*, *58*, 2249–2279.
- Vadas, S. L., & Fritts, D. C. (2002). The importance of spatial variability in the generation of secondary gravity waves from local body forces. *Geophysical Research Letters*, *29*(20), 1984. <https://doi.org/10.1029/2002GL015574>
- Vadas, S. L., & Fritts, D. C. (2013). Corrigendum. *Journal of the Atmospheric Sciences*, *70*, 2680. <https://doi.org/10.1175/JAS-D-13-057.1>
- Vadas, S. L., Fritts, D. C., & Alexander, M. J. (2003). Mechanism for the generation of secondary waves in wave breaking regions. *Journal of the Atmospheric Sciences*, *60*, 194–214.
- Vadas, S. L., & Liu, H.-L. (2009). The generation of large-scale gravity waves and neutral winds in the thermosphere from the dissipation of convectively-generated gravity waves. *Journal of Geophysical Research*, *114*, A10310. <https://doi.org/10.1029/2009JA014108>
- Vadas, S. L., & Liu, H.-L. (2013). Numerical modeling of the large-scale neutral and plasma responses to the body forces created by the dissipation of gravity waves from 6 h of deep convection in Brazil. *Journal of Geophysical Research: Space Physics*, *118*, 2593–2617. <https://doi.org/10.1002/jgra.50249>
- Vadas, S. L., Yue, J., She, C.-Y., Stamus, P. A., & Liu, A. (2009). A model study of the effects of winds on concentric rings of gravity waves from a convective plume near Fort Collins on 11 May 2004. *Journal of Geophysical Research*, *114*, D06103. <https://doi.org/10.1029/2008JD010753>
- Vadas, S. L., Zhao, J., Chu, X., & Becker, E. (2018). The excitation of secondary gravity waves from local body forces: Theory and observation. *Journal of Geophysical Research: Atmospheres*, *123*. <https://doi.org/10.1029/2017JD027970>
- Vargas, F., Swenson, G., Liu, A., & Pautet, D. (2016). Evidence of the excitation of a ring-like gravity wave in the mesosphere over the Andes Lidar observatory. *Journal of Geophysical Research: Atmospheres*, *121*, 8896–8912. <https://doi.org/10.1002/2016JD024799>
- Vincent, R. A., Hertzog, A., Boccara, G., & Vial, F. (2007). Quasi-Lagrangian superpressure balloon measurements of gravity-wave momentum fluxes in the polar stratosphere of both hemispheres. *Geophysical Research Letters*, *34*, L19804. <https://doi.org/10.1029/2007GL031072>
- Walterscheid, R. L., Gelinis, L. J., Mechoso, C. R., & Schubert, G. (2016). Spectral distribution of gravity wave momentum fluxes over the Antarctic Peninsula from Concordiasi superpressure balloon data. *Journal of Geophysical Research: Atmospheres*, *121*, 7509–7527. <https://doi.org/10.1002/2015JD024253>
- Watanabe, S., Kawatani, Y., Tomikawa, Y., Miyazaki, K., Takahashi, M., & Sato, K. (2008). General aspects of a T213L256 middle atmosphere general circulation model. *Journal of Geophysical Research*, *113*, D12110. <https://doi.org/10.1029/2008JD010026>
- Watanabe, S., Sato, K., & Takahashi, M. (2006). A general circulation model study of orographic gravity waves over Antarctica excited by katabatic winds. *Journal of Geophysical Research*, *111*, D18104. <https://doi.org/10.1029/2005JD006851>
- Wu, D. L., & Jiang, J. H. (2002). MLS observations of atmospheric gravity waves over Antarctica. *Journal of Geophysical Research*, *107*(D24), 4773. <https://doi.org/10.1029/2002JD002390>
- Wu, D. L., Preusse, P., Eckermann, S. D., Jiang, J. H., Juarez, M. delaT., Coy, L., & Wang, D. Y. (2006). Remote sounding of atmospheric gravity waves with satellite limb and nadir techniques. *Advances in Space Research*, *37*, 2269–2277. <https://doi.org/10.1016/j.asr.2005.07.031>

- Yamashita, C., Chu, X., Liu, H.-L., Espy, P. J., Nott, G. J., & Huang, W. (2009). Stratospheric gravity wave characteristics and seasonal variations observed by lidar at the South Pole and Rothera, Antarctica. *Journal of Geophysical Research*, *114*, D12101. <https://doi.org/10.1029/2008JD011472>
- Yoshiki, M., Kizu, N., & Sato, K. (2004). Energy enhancements of gravity waves in the Antarctic lower stratosphere associated with variations in the polar vortex and tropospheric disturbances. *Journal of Geophysical Research*, *109*, D23104. <https://doi.org/10.1029/2004JD004870>
- Yoshiki, M., & Sato, K. (2000). A statistical study of gravity waves in the polar regions based on operational radiosonde data. *Journal of Geophysical Research*, *105*, 17,995–18,011.
- Zhang, F. (2004). Generation of mesoscale gravity waves in upper-tropospheric jet-front systems. *Journal of the Atmospheric Sciences*, *61*, 440–457.
- Zhao, J., Chu, X., Chen, C., Lu, X., Fong, W., Yu, Z., et al. (2017). Lidar observations of stratospheric gravity waves from 2011 to 2015 at McMurdo (77.84°S, 166.69°E), Antarctica: Part I. Vertical wavelengths, periods, and frequency and vertical wavenumber spectra. *Journal of Geophysical Research: Atmospheres*, *122*, 5041–5062. <https://doi.org/10.1002/2016JD026368>
- Zhou, X., Holton, J. R., & Mullendore, G. L. (2002). Forcing of secondary waves by breaking of gravity waves in the mesosphere. *Journal of Geophysical Research*, *107*(D7), 4058. <https://doi.org/10.1029/2001JD001204>
- Zhu, X., & Holton, J. R. (1987). Mean fields induced by local gravity-wave forcing in the middle atmosphere. *Journal of the Atmospheric Sciences*, *44*, 620–630.